TU/e EINDHOVEN UNIVERSITY OF TECHNOLOGY

Electro-optical beam steering in an InP optical waveguide

Citation for published version (APA):
Cardarelli, S. (2019). *Electro-optical beam steering in an InP optical waveguide*. [Phd Thesis 1 (Research TU/e / Graduation TU/e), Electrical Engineering]. Technische Universiteit Eindhoven.

Document status and date:
Published: 03/06/2019

Document Version:
Publisher's PDF, also known as Version of Record (includes final page, issue and volume numbers)

Please check the document version of this publication:

• A submitted manuscript is the version of the article upon submission and before peer-review. There can be important differences between the submitted version and the official published version of record. People interested in the research are advised to contact the author for the final version of the publication, or visit the DOI to the publisher's website.
• The final author version and the galley proof are versions of the publication after peer review.
• The final published version features the final layout of the paper including the volume, issue and page numbers.

Link to publication

General rights
Copyright and moral rights for the publications made accessible in the public portal are retained by the authors and/or other copyright owners and it is a condition of accessing publications that users recognise and abide by the legal requirements associated with these rights.

• Users may download and print one copy of any publication from the public portal for the purpose of private study or research.
• You may not further distribute the material or use it for any profit-making activity or commercial gain
• You may freely distribute the URL identifying the publication in the public portal.

If the publication is distributed under the terms of Article 25fa of the Dutch Copyright Act, indicated by the "Taverne" license above, please follow below link for the End User Agreement:

www.tue.nl/taverne

Take down policy
If you believe that this document breaches copyright please contact us at:

openaccess@tue.nl

providing details and we will investigate your claim.

Download date: 05. Oct. 2023

Electro-Optical Beam Steering in an InP Optical Waveguide

PROEFSCHRIFT

ter verkrijging van de graad van doctor aan de Technische Universiteit Eindhoven, op gezag van de rector magnificus prof.dr.ir. F. Baaijens, voor een commissie aangewezen door het College voor Promoties, in het openbaar te verdedigen op maandag 3 juni 2019 om 16:00 uur

door

Simone Cardarelli

Geboren te Teramo, Italy

Dit proefschrift is goedgekeurd door de promotoren en de samenstelling van de promotiecommissie is als volgt:

voorzitter:	prof. dr. ir. J. H. Blom
1e promotor:	prof. dr. K. A. Williams
Co-promotor:	dr. Nicola Calabretta
leden:	prof. dr. A. Fiore
	prof. dr. S. Yu (University of Bristol)
	dr. ir. M. Tichem (Delft University of Technology)
	prof. dr. D. Lenstra
	prof. ir. A. M. J. Koonen

Copyright © 2019 by Simone Cardarelli. All rights reserved. A catalogue record is available from the Eindhoven University of Technology Library
ISBN: 978-90-386-4786-9

… dedicato alla mia amorevole famiglia. Grazie di tutto!

Summary

Optical beam steering is important for metrology, sensing and communication. Researchers have demonstrated beam steering through movable optics and microelectromechanical systems. While the combination of mechanical actuators with the optical source often results in bulky designs and requires extra packaging costs, direct integration on the photonic chip substrate remains a challenge. Electro-optical effects provide refractive index modulation directly in the guiding medium, representing an integrated solution to tune the optical beam direction without employing movable parts.

In this work we investigate an integrated beam steering solution which addresses aspects such as sub-micrometer accuracy, large tuning range, beam quality, low complexity of the electrical circuitry and low electrical power consumption. We study a method to achieve beam steering across the facet of a multimode optical waveguide, through an advanced interference mechanism. Activation of the proposed interference mechanism is proposed by reconfiguration of the refractive index profile of the waveguide. This is studied by using both current injection and voltage controlled effects. The possibility of activating the proposed interference mechanism by reverse bias voltage control is interesting to enable power efficient beam steering. The design space is investigated for both analog and digital operation to address switching and continuous sensing functionalities. The capability of moving an optical beam across the chip facet is important for micro-optical alignment but may also open research routes for free space beam steering functions. The possibility of engineering the output facet of the beam steering device in order exploit the beam steering across the facet for far field reconfiguration is also explored.

The literature review of the main beam steering techniques is reported in **chapter 1**. Different methods are presented together with performance and advantages/disadvantages.

In **chapter 2**, a review of the physical mechanisms which can be exploited in InP technology to achieve refractive index modulation is reported. A model for refractive index perturbation is built in order to perform accurate simulations of the proposed beam steering device. An absorption model is also defined to understand how refractive index perturbation affects optical losses.

The proposed beam steering mechanism is introduced in **chapter 3**. The steering concept is explained through a simple analytical model, which links a refractive index modulation to the modal perturbation and beam steering.

A low power consumption implementation of the device is addressed in **chapter 4** through accurate electrical-optical simulations, in which refractive index modulation is activated through reverse bias voltage. A proof of concept device is studied. A beam steering of ± 1 μm across the chip facet is achieved with a maximum applied voltage of 6 V. The employed technology shows that the voltage driven device efficiency is compromised by the leakage current path present between the control electrodes. The possibility of achieving low power consumption optical switching is numerically demonstrated.

Current injection is experimentally studied in **chapter 5** to achieve large refractive index modulation and explore the tuning range limits of the studied device. An extended steering range of ± 4 μm is shown by employing an electrical power up to 420 mW. The impact that the refractive index perturbation has on the beam quality is studied through a fiber-to-chip coupling experiment.

The effect that the proposed beam steering mechanism has in the far field region is studied in **chapter 6.** The far field of the device is experimentally characterized for both voltage and current control. A concept to enhance far field beam steering is proposed and experimentally demonstrated by integrating a curved facet at the output termination of the device. An enhancement of the full far field beam steering range up to 5° and 60° has been measured for the voltage and current driven beam steering device respectively. This improvement comes at cost of a higher lateral beam divergence on the order of 35°.

The possibility of fabricating curved facets at wafer level is explored in **chapter 7**. A strategy to fabricate etched facets through dry plasma etching is presented. High quality straight facets with a roughness of 7 nm are shown, and obstruction free radiation is achieved after singulation thanks to the proposed precision cleaving strategy.

CONTENTS

SUMMARY **6**

1 INTRODUCTION **13**

1.1 OPTICAL ALIGNMENT IN PHOTONICS 13

1.1.1 Passive alignment techniques *14*

1.1.2 Active alignment techniques *17*

1.2 OPTICAL ALIGNMENT THROUGH REFRACTIVE INDEX MODULATION: BEAM STEERING TECHNIQUES 20

1.2.1 Liquid crystals *21*

1.2.2 Photonic integrated optical phase arrays *22*

1.2.3 Tuned MMI *23*

1.3 CONCLUSIONS AND PROPOSED RESEARCH 24

1.3.1 Thesis outline *26*

2 REFRACTIVE INDEX MODULATION **28**

2.1 INTRODUCTION 28

2.2 ELECTRO-OPTIC EFFECTS IN INP/INGAASP MATERIALS 28

2.2.1 Pockels effect *29*

2.2.2 Kerr effect *31*

2.3 FREE-CARRIER EFFECTS IN INP/INGAASP MATERIALS 32

2.3.1 Band filling effect *32*

2.3.2 Plasma effect *34*

2.4 ABSORPTION COEFFICIENT MODULATION 35

2.4.1 Free-carrier absorption *36*

2.4.2 Franz-Keldysh effect *37*

2.5 CONCLUSIONS 38

3 TWO-MODE ELECTRO-OPTIC BEAM STEERING **41**

3.1 BEAM STEERING CONCEPT 41

3.2 ANALYTICAL MODEL 42

3.2.1 2D approximation *42*

3.2.2 Perturbation model *43*

3.2.3 Analytical beam steering formula *47*

3.3 CONCLUSIONS 54

4 VOLTAGE DRIVEN ELECTRO-OPTICAL BEAM STEERING 57

4.1 INTRODUCTION 57
4.2 REVERSE BIAS VOLTAGE DRIVEN STEERING DEVICE 57
4.2.1 Two dimensional reverse bias voltage simulation 58
4.2.2 Perturbed optical beam propagation 61
4.2.3 Impact of the input modal purity 64
4.3 GENERIC FOUNDRY ENABLED VOLTAGE DRIVEN STEERING 65
4.3.1 Sub-micron beam steering 67
4.3.2 Enhanced beam steering through a controlled input condition . 69
4.4 DESIGN OF AN ENERGY EFFICIENT 1X2 VOLTAGE DRIVEN SWITCH 72
4.4.1 Schematic of the voltage driven optical switch 73
4.4.2 Optical switch performance 74
4.4.3 Tolerance analysis 75
4.5 CONCLUSIONS 77

5 CURRENT DRIVEN ELECTRO-OPTICAL BEAM STEERING 79

5.1 INTRODUCTION 79
5.2 CURRENT INJECTION BEAM STEERING DEVICE 79
5.2.1 Enhanced optical beam steering 83
5.2.2 Chip-to-fiber misalignment compensation 85
5.3 CONCLUSIONS 87

6 FAR FIELD BEAM STEERING 90

6.1 INTRODUCTION 90
6.2 ENHANCED FAR FIELD BEAM STEERING THROUGH A CURVED OUTPUT FACET ... 90
6.2.1 Curved facet functionality 90
6.2.2 Far field beam steering: simulations 91
6.3 EXPERIMENTAL FAR FIELD BEAM STEERING 93
6.3.1 The voltage driven far field reconfiguration 94
6.3.2 The current driven far field reconfiguration 97
6.4 ANGLE OF ARRIVAL DETECTION 99
6.5 CONCLUSIONS 101

7 MANUFACTURING METHOD FOR ETCHED FACETS 103

7.1 INTRODUCTION 103
7.2 ETCHED FACETS FABRICATION 104
7.2.1 Facet and scribe mark etching 105

7.2.2 Singulation *108*
7.3 OPTICAL BEAM QUALITY 112
7.3.1 Near and far field characterization *112*
7.3.2 Singulation requirements *113*
7.4 CONCLUSIONS 114
8 CONCLUSIONS 116
9 APPENDIX - PIEZOELECTRIC BASED FIBER ALIGNER IN TWO DIMENSIONS 119
9.1 INTRODUCTION 119
9.2 TWO DIMENSIONAL PIEZOELECTRIC ACTUATOR 119
9.2.1 Design and principle of operation *119*
9.2.2 Piezo assembly characterization *120*
9.2.3 Photonic integrated circuit *122*
9.3 FIBER-CHIP COUPLING 124
9.3.1 Piezoelectric misalignment compensation *125*
9.3.2 Automatic compensation *126*
9.4 CONCLUSIONS 128
10 APPENDIX-THE FABRICATION PROCESS FLOW 130
10.1 INTRODUCTION 130
10.2 PROCESS FLOW 130
10.2.1 Active/passive integration *131*
10.2.2 Waveguides definition *132*
10.2.3 Passivation *132*
10.2.4 Metallization *132*
10.2.5 Etched facets *132*
10.2.6 Wet etched scribe marks *134*
10.2.7 Singulation *135*
BIBLIOGRAPHY 137
LIST OF PUBLICATIONS 148
ACKNOWLEDGMENTS 150
CURRICULUM VITAE 157

1 Introduction

Beam steering through photonics is a valid method to enable either continuous or digital alignment functionalities with features such as sub-micrometre accuracy, wide angle range, low power consumption, all collected in a compact integrated solution.

Beam steering is applicable to a number of fields ranging from LIDAR [1], sensing [2], metrology [3], and imaging [4] to communication [5]. Beyond classical optical beam steering methods based on optomechanical devices [6], several novel integrated optical beam steering techniques are reported in the literature. These include techniques based on micro-electromechanical systems (MEMS) [7], liquid crystals [8] and photonic integrated circuits (PICs) [9]. Methods based on PICs are interesting to enable compact integration of the steering function directly with the optical source [10]. Photonic integrated beam steering has been employed to demonstrate functions such as optical switching [11] and LIDAR [1]. This dissertation will explore integrated optical beam steering based on photonic integration to enable new concepts for micro-alignment of optical components without the use of movable parts, a function not yet addressed by PICs.

In this chapter, the importance of micro-optical alignment is introduced, together with the main alignment techniques reported in the literature. Alignment techniques based on beam steering are highlighted and discussed to motivate our research direction. The ambitions and challenges of this thesis are reported at the end of this chapter.

1.1 Optical alignment in photonics

The reliable employment of photonic modules is possible if the fabricated PICs are provided with a robust and accurate packaging service [12]. One of the most critical steps in photonic packaging is the alignment [12] of optical components. Fiber-to-chip alignment, positioning of micro-lenses and alignment of fiber arrays have direct impact on the performance of the final photonic module and require sub-micrometer accuracy [13]. Part of the alignment procedure still needs manual operation, making the total packaging a slow and expensive process, which may represent up to 80 % of the total photonic module price [14] for large volume production. Developing low-cost and efficient alignment techniques is particularly important for InP technology that still cannot rely on the same packaging technology level of silicon semiconductor industry [15]. Researchers have proposed several *passive* and *active* alignment techniques in order to improve speed, accuracy and yield in photonic packaging.

1.1.1 Passive alignment techniques

Passive alignment techniques aim either to ease the positioning of optical fibers with respect to the photonic I/O waveguide ports, or to improve the chip-fiber coupling tolerance to misalignments. *Passive alignment* techniques may rely on mode conversion [16], engineered geometrical constraints [17], or thermal effects [18] and do not require monitoring of the optical power coupling efficiency. *Passive alignment* enables fast and low-cost assembly but hardly can achieve the sub-micron alignment accuracy necessary for optimal optical coupling from single mode lasers to optical fibers [19].

V-grooves

V-grooves are *passive alignment* features often employed to achieve accurate optical fiber positioning [20]. High precision V-grooves can be fabricated through photolithographic process with a pitch accuracy in the order of tens of nanometers, and a sub-micron accuracy on the final opening width [21]. Wet chemical etching is usually employed for semiconductor V-grooves formation because of the process cleanness and precision. The geometry of wet etched V-grooves is defined by the etched semiconductor crystal planes. V-grooves are attractive to accurately place optical fibers in a linear array scheme to achieve multiport coupling to photonic chips. A common fiber-chip coupling scheme is show in Figure 1-1.

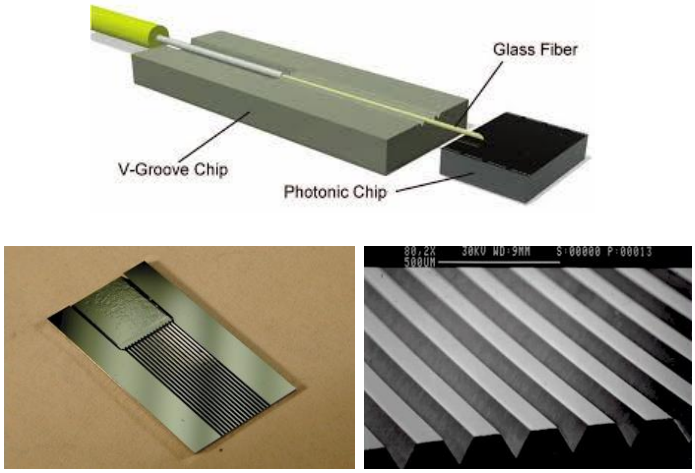

Figure 1-1. a) fiber-chip coupling schematic through V-grooves based passive alignment [22]. b) optical and SEM photograph of a V-groove based carrier [23].

V-grooves for fiber positioning can be either fabricated on a different substrate with respect to the photonic die, or directly integrated on the photonic chip [24] if the design is properly oriented with respect to the crystal orientation. The advantage of integrating V-grooves on the photonic chip is that a fiber array can be mounted directly on-chip, for a compact package solution. However, V-grooves integrated on the photonic chip require large functional footprint and the final alignment is compromised by the optical fiber core eccentricity [13]. The V-grooves depth, defined with an accuracy on the order of ± 1 μm, may represent an issue [21] in terms of vertical alignment. A fiber-chip coupling experiment has been performed through V-grooves and a coupling loss of 5 dB has been demonstrated [25], with a fiber positioning accuracy of 1 μm.

Solder bumps

Solder bumps have been extensively employed for flip-chip packaging in the electronics industry [26]. Solder bumps, when sandwiched between two contact pads and after thermal activation, have the capability of reflowing and aligning the two pads when cooling down, as shown in Figure 1-2. Solder bumps are typically fabricated by electro-plating [27] or through ball-wire bonding tools [28].

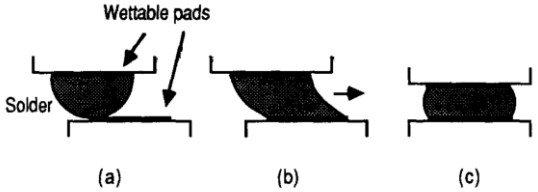

Figure 1-2. Principle of alignment for the solder bumps technique [29].

Alignment through solder bumps has been exploited by researches to provide lateral optical alignment techniques. Lateral alignment through solder bumps between fiber array units and the photonic die has been demonstrated [29]. Solder bumps are applied on top of the fiber array carrier while the opposite contact pad is realized on the photonic die surface. The fiber array is flipped on top of the die to achieve solder bump-to-pad contact and lateral passive alignment. Vertical alignment control might be compromised by a poor solder-bump dimension reproducibility, furthermore, control of the ball height change after thermal activation is needed. Self-alignment accuracy on the order of ± 0.5 μm has been reported [29].

Integrated mode converters

Mode conversion is sometimes considered as passive alignment technique, sometimes as a support to other passive alignment methods. Mode conversion aims to improve the misalignment tolerance of the optical system. Single mode optical fields in photonic waveguides have mode sizes on the order of 1 μm and assembly with subsequent optics is critical to optimize the coupling efficiency. Mode converters enable a magnification of the on chip optical mode in order to achieve both a tolerant coupling to sub-micron misalignment and mode matching to optical fibers. Mode converters are usually based on adiabatically tapered optical waveguides and can exhibit either one or two dimensional mode expansion. An example of a two dimensional mode converter schematic for InP technology is shown in Figure 1-3 [30].

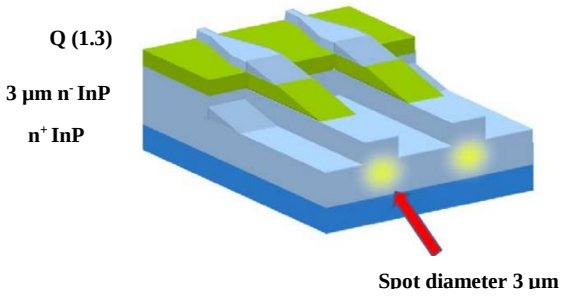

Figure 1-3. 3D schematic of spot size converters based on InP technology [30].

On chip mode conversion is attractive for the possibility of processing fiber-mode matched I/O ports at wafer level, however adiabatic tapering requires significant footprint of the photonic die and a more complex fabrication process is required. Mode conversion might be compared to passive alignment techniques by quoting the -1 dB misalignment tolerance, which is the spatial fiber-to-chip misalignment range for which the misalignment loss is smaller than 1 dB. Spot size converters with -1 dB misalignment tolerance of ± 1.7 μm have been demonstrated [31].

Micro-optics

Expansion of the optical beam radiated from a photonic chip can also be achieved by inserting optics between the chip and the optical fiber. Micro-lenses can be designed to project the radiated beam from the chip into the optical fiber and achieve field magnification for fiber-mode matching. Using a lens as a beam magnifier, instead of on chip spot size converters, may have multiple advantages such as saving functional area on the optical die and enabling power coupling

optimization of the fiber along the focal axis. Figure 1-4 shows a common schematic of a chip-lens-fiber assembly [12].

Figure 1-4. Schematic of chip-to-fiber mode conversion through a micro-optical lens [12].

Micro-optics is attractive to implement field size conversion functionalities off-chip, however, it requires extra fabrication, space and assembly effort, compromising the final packaged die costs. Arrays of micro-lenses have been demonstrated in order to parallelize the lens assembly process but the accurate positioning and fixation of individual lenses in the array remains a challenge. A misalignment tolerances between ± 0.8 μm and ± 1.5 μm has been reported for a misalignment loss of 3 dB in [32].

A summary of the characteristics of the presented passive alignment methods is shown for comparison in Table 1-1, in terms of accuracy in fiber alignment, fiber-chip coupling misalignment tolerance and fiber to chip coupling loss.

Method	**Alignment accuracy [μm]**	**Misalignment tolerance [μm]**	**Coupling loss [dB]**
V-grooves [25]	± 1		5 dB
Solder bumps [29]	± 0.5		1 dB
Mode converters [31]		± 1.7 (at -1 dB)	0.5 dB
Micro-optics [32]		± 0.8 – 1.5 (at -3 dB)	2 dB

Table 1-1. Summary of passive alignment methods performance.

1.1.2 Active alignment techniques

Active alignment is a technique which requires monitoring of the power transmitted between two optical modules to achieve accurate alignment. Fiber-to-chip *active alignment* implies monitoring of the optical power coupling while the fiber-to-chip alignment and fixation is performed and is an effective technique especially for photonic chips with active materials. Sub-micron accuracy can be achieved at cost of a more expensive and slower alignment process [33]. *Active alignment* provides better yield in terms of coupling efficiency per port with respect

to passive techniques. *Active alignment* techniques often exploit MEMS as on/off chip thermal [12], electrostatic [34] or piezoelectric actuators [35].

Thermal actuators

Thermal actuators for active alignment are based on the combination of materials with different coefficients of thermal expansion (CTE). When materials with different CTE are set in contact and the temperature is tuned, the strain between the two materials changes and deformation is observed. A thermoelectrically actuated flexible waveguide used as interface between an InP PIC and an optical fiber array has been demonstrated [36]. Vertical actuation of up to 18.5 µm with an electrical power consumption of 130 mW has been demonstrated. The concept of the flexible waveguides array, used as an interposer between the photonic die and optical fiber array, is schematically shown in Figure 1-5.

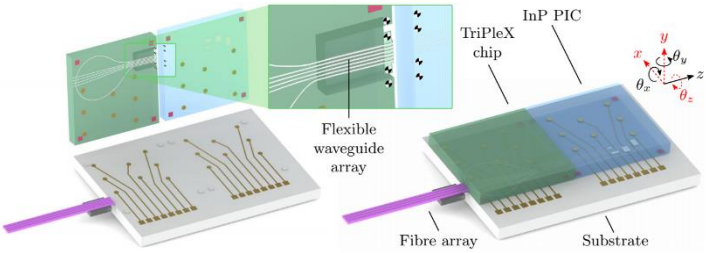

Figure 1-5. Schematic of alignment concept based on thermally actuated flexible waveguides [36].

Thermal actuation is attractive for large deflection capability. Furthermore, the possibility of achieving thermal actuation in silicon and silicon dioxide technology is an advantage in terms of standardized processing [37]. However, it requires an additional interface to be fabricated and aligned for the optical transition from chip-to-fiber.

Electrostatic actuation

Micro fabricated electrostatic actuators are employed in a wide variety of MEMS for applications ranging from relays and switches to valves and displays. The mechanical deflection mechanism for electrostatic actuators is based on the electrostatic force which occurs between two electrodes when excited with a sufficiently high voltage. Electrostatically actuated gratings have been fabricated to demonstrate a voltage driven and low power alignment method to align the on chip beam with the fiber core position [34]. A displacement of 6 µm has been achieved

with a driving voltage of 6 V. A photo of the electrostatic grating and alignment mechanism is shown in Figure 1-6.

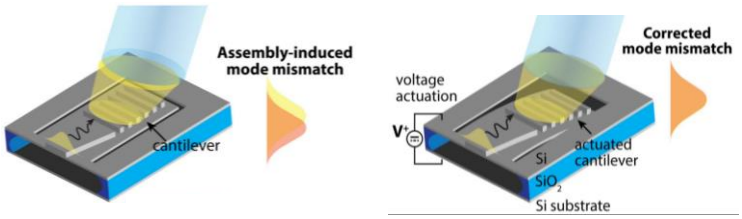

Figure 1-6. Photograph of the alignment mechanism based on the electrostatic grating [34].

Electrostatic actuators present many advantages, with respect to other MEMS technologies, as low power consumption, fast response time [38]. Electrostatic devices can be realized by using a wide set of materials (e.g. silicon, silicon dioxide, aluminium, nickel, diamond), which is attractive for the integration with different fabrication methods. However, the tuning range for electrostatic actuators is limited by the pull-in effect [39].

Piezoelectric actuators

The piezoelectric effect is the mechanical deformation that certain solid materials (crystals, ceramics) exhibit when excited with an electrical potential. Piezoelectric actuators enable low power consumption operation and typically require lower driving voltage with respect to electrostatic actuators [40]. Simulations of a cantilever beam with dimensions 100×10×2 μm^3 have shown a piezoelectric deformation of 1 µm for an applied voltage of 50 V, the actuation is 12.5 times larger with respect to the electrostatic deflection [41]. Several piezoelectric actuators can be fabricated from PZT ceramics: tube, laminate, stacked and bimorph [42]. An example of a piezoelectric assembly employing a bimorph PZT based stuck and used for fiber-to-chip alignment is shown in Figure 1-7 [43].

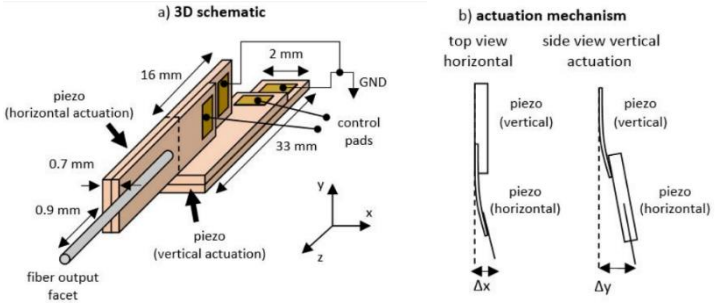

Figure 1-7. a) Schematic of the piezoelectric based alignment assembly and b) the actuation mechanism.

The piezoelectric assembly in [43] has shown the possibility of achieving an optimal fiber chip coupling in a misalignment window of 100 μm^2, with a maximum applied voltage and current of 25 V and 26 nA, respectively. The work in [43] has been conducted by the author and reported in Appendix 9. PZT piezoelectric actuators are very often employed for MEMS application and can be processed though lithographical techniques, at cost of a time consuming process [44]. Micromachining of PZT material is challenging due to the brittle nature of the ceramics [45].

The features of the presented active aligned methods are summarized in Table 1-2, in terms of total tuning range and power consumption.

Method	**Tuning range [µm]**	**Power consumption**	**Coupling loss [dB]**
Thermal [36]	18.5	130 mW	Not measured
Electrostatic [34]	6	Not significant	2 dB
Piezoelectric [46]	10 × 10	Not significant	2.1 dB

Table 1-2. Summary of the active alignment methods performance.

1.2 Optical alignment through refractive index modulation: beam steering techniques

The first part of the introduction has focused on examples of *passive* and *active* alignment methods to manipulate micro-optics. *Active alignment* techniques through MEMS are mainly employed where sub-micron accuracy and high yield is required. However, the alignment speed of methods based on movable parts might be an issue where relatively short activation times are necessary [47] and alternative solutions are required.

This thesis proposes to explore the possibility of achieving optical alignment by steering the on chip optical beam through refractive index modulation of the guiding medium, without employing movable parts. In a fiber-chip alignment scenario, the proposed solution aims to enable concepts for automated and low power on chip optical alignment, where the on chip optical beam is electro-optically moved across the chip facet to track the optical fiber core position and relax alignment tolerances. The proposed research route is interesting for new *active alignment* solutions for photonic packaging, and may also enable new concepts for LIDAR [9], switches [48], in home communication [49] and sensing [2]. A summary of well-known beam steering techniques based on liquid crystals (LCs), optical phased arrays (OPAs) and tuned MMIs is here reported to motivate the direction of our work.

1.2.1 Liquid crystals

A liquid crystal is a non-classic state of the matter for which both features of liquids and solids coexist. For example, liquid crystals can flow like a liquid while the molecules can be oriented like in a crystal or a dielectric material. Liquid crystals molecules are usually electrically asymmetric (dipoles) and can be oriented by applying an electric field. The orientation of the liquid crystals molecules causes a material refractive index change which can be employed for light phase modulation and beam steering. An example of beam steering mechanism actuated through liquid crystals polarization is shown in Figure 1-8. The region filled with liquid crystal presents a prism shape and is contacted with a material with different refractive index. When the molecules polarization of the liquid crystal occurs, the change in refractive index modifies the angle relationship between the incident and transmitted rays and beam steering is observed. Deflection through LCs can be achieved using voltage-controlled phase modulation for both reflective [50] or transmissive [8] operations.

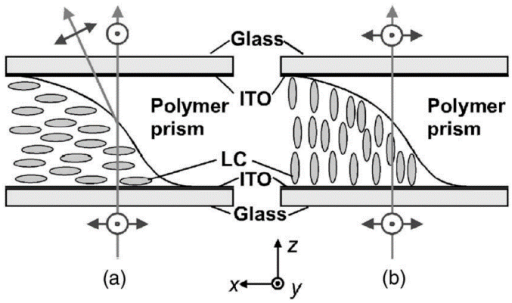

Figure 1-8. Beam steering mechanism through the polarization of liquid crystals molecules [51].

LC devices can achieve up to 20° beam deflection with a large number of precisely controlled beams (10^4 -10^5). LC devices are interesting due to low power consumption and low activation voltage, however the speed is limited to <10 kHz [52]. LCs can be controlled in a single electrode or multiple electrodes configuration. A metal plate is attached to the LC cell for a single electrode configuration and the refractive index change is uniform in the liquid crystal. Patterning of multiple electrodes on top of the LC cell enables non-uniform spatial control of the refractive index change in the liquid crystal cell. By tuning the voltage applied to each electrode, paths with different phase change can be enabled in the LC cell to achieve an optical phased array operation [53]. An optical phased array liquid crystal module has exhibited a total steering range of 80° [54]. Integration of LC in Si and InP technology has been demonstrated [55], [56], however, the risk of trapped gas in the liquid crystals may degrade the device performance [57].

1.2.2 Photonic integrated optical phase arrays

OPAs based on integrated waveguide phased array allow independent control in the array of uncoupled channel waveguides to achieve the wanted steering characteristics. The working principle of such an OPA is based on the interference of individual radiating optical waves with their neighbouring waves forming the desired wavefront in a particular direction. The direction of the wavefront can be tuned by changing the field phase in each waveguide. Phase modulation can be achieved either by thermal or electro-optic effects and the scanning range can be linear or two dimensional according to the geometrical configuration of the emitters. Emitters can be designed in a linear configuration and combined with surface emitting gratings to achieve two dimensional steering through wavelength control. Figure 1-9 shows the schematic of an optical phased array combined with surface emitting grating [10].

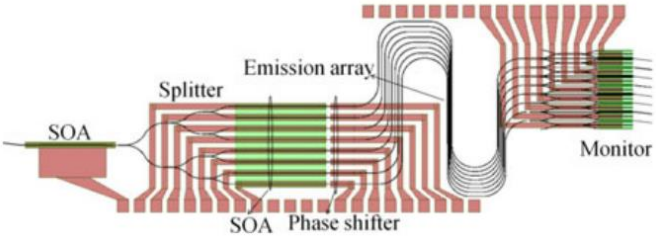

Figure 1-9. Schematic of an optical phase array realized in InP technology [10].

OPAs with wide beam steering up to 51° with a full width half maximum of 3.3° have been demonstrated [9] and low electrical power consumption can be achieved by applying reverse bias voltage to p-i-n junction based waveguides. The beam quality is limited by the number of emitters and if a highly densely integrated solution has been shown in silicon technology, the integration with lasers remains an issue. In order to address a solution with reduced circuitry/control complexity and smaller footprint, beam steering devices based on tuned MMIs are introduced in next sub-chapter. Tuned MMIs are important since only on emitter is employed to achieve beam steering, by electrically controlling few electrodes applied on top of a multimode waveguide.

1.2.3 Tuned MMI

Multi-mode interference based beam steering devices operated by direct control of the refractive index profile in a multimode waveguide to achieve continuous and digital beam steering. Continuous beam steering occurs if the refractive index at the boundaries of the multimode interference device is controlled by current injection [58]. A schematic of the tuned MMI device for continuous beam steering is shown in Figure 1-10. The optical beam injected into the input waveguide spreads laterally once in the slab waveguide underneath the contacts. The beam can be confined and shifted by tuning the current injected through the contacts. The first prototypes relied on current injection and exhibited an operational current of up to 250 mA. The index-profile tuning MMI concept has also been implemented with multiple quantum wells and selective area doping in order to improve the electro refractive modulation efficiency and the current confinement. Near field beam steering of up to 17 μm has been demonstrated for this approach with a current of 17 mA [59].

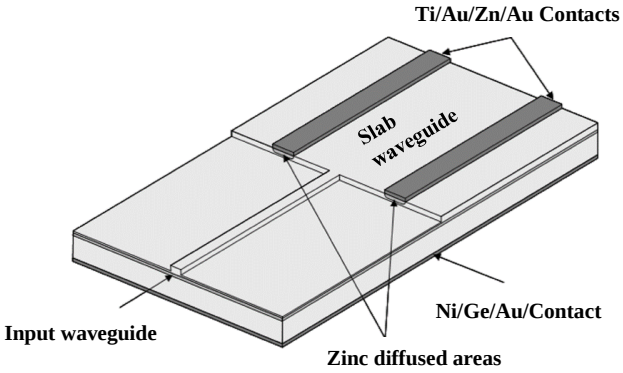

Figure 1-10. Schematic of a tuned MMI beam steering device [59].

The tuned MMI in [59] enables large beam steering with respect to the beam size but electrical power has to be constantly provided for the beam confinement, even though beam steering is not required. Applying electrodes to a laterally confined MMI coupler represents a solution to achieve beam steering through modal interference suppression, in an energy efficient manner. Suppressed mode interference can achieve a digital form of beam steering by injecting currents of up to 30 mA through an electrode placed only on one side of the MMI coupler [60].

The steering characteristics of the discussed techniques are summarized in Table 1-3.

Method	**Beam steering [μm]**	**Free space steering [degrees]**
Liquid crystals [54]		80
OPAs [9]		51
Tuned MMIs [59]	17	Not measured

Table 1-3. Summary of the reported beam steering techniques.

1.3 Conclusions and proposed research

The reported review of the main micro-optical alignment techniques has shown advantages and disadvantages of different methods. *Passive alignment* enables fast operation, however, the lack of control on the alignment degrades the final accuracy. *Active alignment* based on MEMS is employed when sub-micrometer accuracy is necessary. An actuation displacement of the order of tens of micrometers can be achieved through off chip solutions, but extra space and assembly steps are

required in the final package. On-chip alignment solutions based on MEMS have been shown in Si material, however, the integration with laser is still challenging. InP has promising properties for MEMS integration [61], but the demonstrated actuation is still limited to a few hundreds of nanometers [62]. Alignment techniques based on a refractive index modulation represent a solution to achieve a higher level of integration. Furthermore, this method can enable higher speed operation with respect to mechanical methods.

Optical alignment through liquid crystals is possible, but challenges remain in terms of integration and manufacturing reliability. Integrated OPAs enable wide angle beam steering for optical alignment, however, it requires a large number of electrodes and controls in order to achieve high beam quality. A low electrical complexity is provided by tuned MMI couplers, for which beam steering has been shown with a limited number of electrodes. Tuned MMIs are operated through current injection which may be an issue in terms of electrical power efficiency.

In this work we investigate an integrated beam steering solution which addresses aspects such as sub-micrometer accuracy, large tuning range, beam quality, low complexity of the electrical circuitry and low electrical power consumption. We study a method to achieve beam steering across the facet of a multimode optical waveguide, through an advanced interference mechanism. Activation of the proposed interference mechanism is proposed by reconfiguration of the refractive index profile of the waveguide. This is studied by using both current injection and voltage controlled effects. The possibility of activating the proposed interference mechanism by reverse bias voltage control is interesting to enable power efficient beam steering. The design space is investigated for both analog and digital operation to address switching and continuous sensing functionalities. The capability of moving an optical beam across the chip facet is important for micro-optical alignment but may also open research routes for free space beam steering functions. The possibility of engineering the output facet of the beam steering device in order exploit the beam steering across the facet for far field reconfiguration is also explored.

1.3.1 Thesis outline

In **chapter 2**, a review of the physical mechanisms which can be exploited in InP technology to achieve refractive index modulation is reported. A model for refractive index perturbation is built in order to perform accurate simulations of the proposed beam steering device. An absorption model is also defined to understand how refractive index perturbation affects optical losses.

The basic beam steering device exploiting the proposed interference mechanism is introduced in **chapter 3**. The steering concept is explained through a simple analytical model, which links a refractive index modulation to the modal perturbation and beam steering.

The low power consumption implementation of the device is addressed in **chapter 4** through accurate electrical-optical simulations, in which refractive index modulation is activated through reverse bias voltage. A proof of concept device has been realized and the experimental results are shown. The possibility of achieving low power consumption optical switching is numerically studied.

Current injection is experimentally studied in **chapter 5** to achieve large refractive index modulation and explore the tuning range limits of the studied device. The possibility of tuning the refractive index over a large range through current based effects is an opportunity to study the beam quality for a wide set of steering values. The impact that the refractive index perturbation has on the beam quality is studied through a fiber-to-chip coupling experiment.

The effect that the proposed beam steering mechanism has in the far field region is studied in **chapter 6**. The far field of the device is experimentally characterized for either voltage and current control. A concept to enhance far field beam steering is proposed and experimentally demonstrated by integrating a curved facet at the output termination of the device.

The possibility of fabricating curved facets at wafer level is explored in **chapter 7**. A strategy to fabricate etched facets through dry plasma etching is presented. The quality of the realized facets is morphologically and optically characterized. The requirements on the process accuracy are also studied.

2 Refractive index modulation

2.1 Introduction

Electro-refraction is the property of a material to exhibit a refractive index change by means of an electrical control. It is important to know what physical mechanisms can induce a refractive index change in a material in order to understand how to electronically control an optical waveguide to achieve beam steering. In this chapter, a review of the relevant effects suitable to enable electro-refraction InP/InGaAsP materials is reported, in order to build a model to predict electronically controlled refractive index perturbation.

A refractive index change in InP/InGaAsP semiconductors can be achieved by either applying an electric field or by tuning the free-carrier density. The refractive index modulation due to an applied electric field and a carrier density change is called electro-optic and free-carrier effect, respectively. The electro-optic mechanisms studied in this thesis are the Pockels and the Kerr effects, the considered free-carrier effects are the Band-filling and the plasma effects. A change in the refractive index causes a variation of the absorption properties of the material. After reporting the electro-refraction effects, the change in absorption will be also discussed and modelled by considering two absorption mechanisms: the Franz-Keldysh effect and the free-carrier absorption.

2.2 Electro-optic effects in InP/InGaAsP materials

A plane wave travelling through a medium can in general exhibit different phase velocities along different propagation directions. Such a phenomenon is modelled by defining an anisotropic refractive index for the guiding medium. The *index ellipsoid* is a useful mathematical tool to describe the refractive index experienced by a travelling optical field [63] in an anisotropic medium. The *index ellipsoid* is a geometrical surface representing the refractive index observed by an electric field oscillating along the same direction of a vector pointing to a (x, y, z) point of the surface. In case the guiding medium is a crystal, the x, y and z coordinates are related to the Miller indices (*h, k, l*) [64] describing the plane orientations in a crystal. The general expression for the *index ellipsoid* is

$$\eta_{11}x^2 + \eta_{22}y^2 + \eta_{33}z^2 + 2yz\eta_{23} + 2zx\eta_{31} + 2xy\eta_{12} = 1 \qquad (1)$$

Where the tensor η_{ij} is called impermeability tensor, is symmetrical, and depends on the guiding material. The *index ellipsoid* can be reconfigured by tuning the coefficients of the impermeability tensor, in order to achieve refractive index

modulation. The change of the impermeability tensor by means of an externally applied electric field is called electro-optic effect.

2.2.1 Pockels effect

The electro-optic effect is modelled as a polynomial function of the absolute value of the applied static electric field. The electro-optic effect related to the linear contribution of the polynomial is called Pockels effect, and is modelled by the following formula

$$\Delta\eta_{ij} = \sum_{k} \tilde{r}_{ijk}\ E_k \tag{2}$$

where $\tilde{r}_{ijk}$ are the *linear electro optic* (LEO) *coefficients*, *k* is an index identifying the electric field spatial components and can assume the values {x, y, z}, E_k is the amplitude of the *k*-th component of the electric field. The relationship between $\Delta\eta_{ij}$ and E_k is usually reported by using a simplified version of the $\tilde{r}_{ijk}$ matrix. The matrix $\tilde{r}_{ijk}$ can be rewritten as a two dimensional matrix due to the symmetry of the impermeability tensor, and equation (2) can be expressed such as

$$\begin{bmatrix} \Delta\eta_{11} \\ \Delta\eta_{22} \\ \Delta\eta_{33} \\ \Delta\eta_{12} \\ \Delta\eta_{23} \\ \Delta\eta_{31} \end{bmatrix} = \begin{bmatrix} r_{11} & r_{12} & r_{13} \\ r_{21} & r_{22} & r_{23} \\ r_{31} & r_{32} & r_{33} \\ r_{41} & r_{42} & r_{43} \\ r_{51} & r_{52} & r_{53} \\ r_{61} & r_{62} & r_{63} \end{bmatrix} \begin{bmatrix} E_x \\ E_y \\ E_z \end{bmatrix} \tag{3}$$

where the matrix r_{ij} is called *electro-optic tensor*. The ordinary index ellipsoid in InP/InGaAsP materials is a sphere, and the Pockels effect occurs according to the following electro-optic tensor.

$$\begin{bmatrix} 0 & 0 & 0 \\ 0 & 0 & 0 \\ 0 & 0 & 0 \\ r_{41} & 0 & 0 \\ 0 & r_{41} & 0 \\ 0 & 0 & r_{41} \end{bmatrix} \tag{4}$$

The refractive index modulation related to the InP/InGaAsP electro-optic tensor is schematically shown in Figure 2-1, when a static electric field is applied across an InP wafer, perpendicularly to the wafer surface.

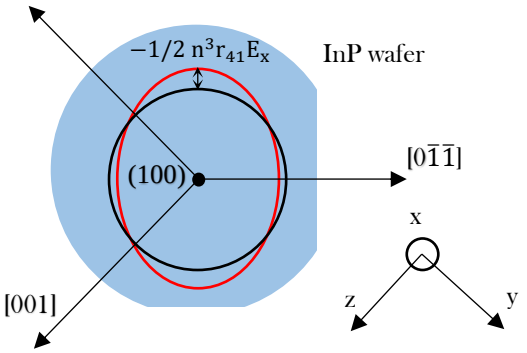

Figure 2-1. Schematic representation of the index ellipsoid perturbation in an InP wafer.

The number in between the brackets are the Miller indices, a crystal plane is identified by round brackets whereas a direction is defined with square brackets. The light blue disk with two flat sides represents the top view of an InP wafer complying (European-Japanese standard [65]) with the top surface parallel to the (100) crystal plane. The black circle is the intersection between the wafer plane and the unperturbed *index ellipsoid*, whereas the red ellipse represents a section of the perturbed *index ellipsoid*. The achieved refractive index change is

$$\begin{aligned} \Delta n &= -\frac{1}{2} n^3 r_{41} E_x \quad for \quad [01\bar{1}] \\ \Delta n &= \frac{1}{2} n^3 r_{41} E_x \quad for \quad [0\bar{1}\bar{1}] \\ \Delta n &= 0 \quad for \quad [100] \end{aligned} \tag{5}$$

where n is the unperturbed refractive index. The maximum change of the refractive index is observed along the directions [01$\bar{1}$] and [0$\bar{1}\bar{1}$], for which a TE polarized field can be excited. The TM polarized optical field is commonly defined along the [100] direction and is not affected by the Pockels effect. Researches have measured an r_{41} LEO coefficient of the order of $-1.4\frac{\mathrm{pm}}{\mathrm{V}}$ for InP [66], at the optical wavelength of 1.3 μm. The wavelength dependence of the LEO coefficients for InP and InGaAsP can be derived by an analytical model reported by Adachi [67]. The

calculated r_{41} coefficient is shown in Figure 2-2 for InP and for InGaAsP with a bandgap wavelength of 1.25 µm, experimental data is also shown for comparison.

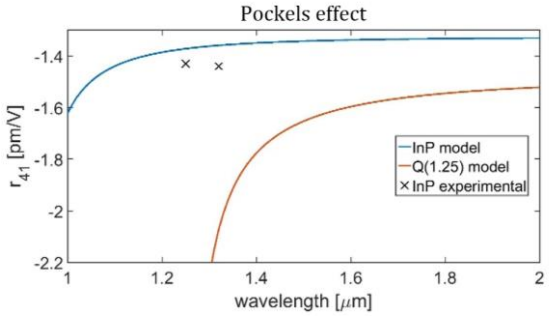

Figure 2-2. LEO coefficient measured in [66] and model [67].

2.2.2 Kerr effect

If the external applied field is strong enough, or the linear electro-optic tensor is zero, a quadratic change of the refractive index might be observed. This phenomenon is called Kerr effect. The Kerr effect is modelled by adding a quadratic term to the polynomial expression of the impermeability coefficient perturbation. The quadratic term representing the Kerr effect is

$$\Delta\eta_{ij}'' = \sum_k \sum_l R_{ijkl}\ E_k E_l \qquad (6)$$

Where the apices in $\Delta\eta_{ij}''$ indicate the second order term of the impermeability perturbation polynomial and R_{ijkl} is the quadratic electro-optic (QEO) coefficient. The matrix R_{ijkl} can be compressed into a two dimensional matrix due to symmetry considerations. The refractive index modulation due to the Kerr effect in InP/InGaAsP (see Figure 2-1) for an external static electric field perpendicular to the wafer surface is

$$\Delta n_{Kerr} = \frac{1}{2} n^3 R_{12,11} {E_x}^2 \qquad (7)$$

where R_{12} and R_{11} are the quadratic electro-optic coefficients relative to the TE and TM polarized optical fields, respectively.

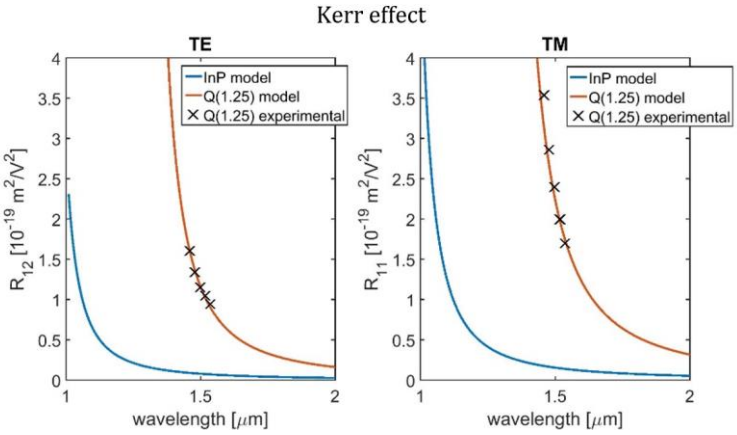

Figure 2-3. QEO coefficients following the model in [68] compared to experimental data from [69].

The QEO coefficients used to model the Kerr effect in InP and Q(1.25) InGaAsP are shown in Figure 2-3 as a function of wavelength. The QEO are represented by the solid lines and follow from the analytical model found in [68]. A multiplication factor of 1.1 and 2.1, for the TE and TM mode, has been added to the analytical model in [68] to provide calibration with experimental data that has been reported in [69].

2.3 Free-carrier effects in InP/InGaAsP materials

Electro-refraction in a semiconductor can also be modulated by tuning the local free carrier concentration. A change in the carrier concentration affects the absorption properties of a material. Such a phenomenon is attributed to the connection between the density of occupied electron/hole states and the probability of an electron to be excited to a different energy state. A change in the absorption coefficient of a material is linked to a refractive index modulation through the Kramers-Kronig formulas [63].

2.3.1 Band filling effect

Electrons in the valence band of an intrinsic semiconductor require an energy equal to the energy band gap in order to be excited to the conduction band. If carriers are injected into the conduction band, higher energy is needed for an electron to jump into a free state in the conduction band and a change of the effective energy gap is observed (see Figure 2-4), together with an absorption coefficient variation.

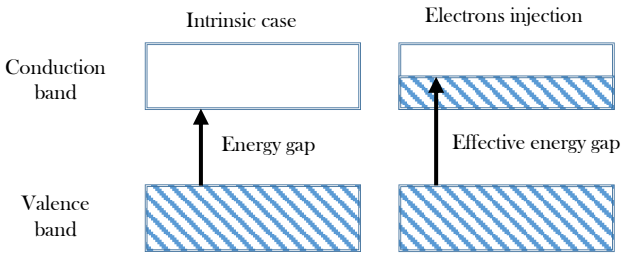

Figure 2-4. Schematic of the band filling mechanism.

This process is an *interband process* since related to energy states belonging to different energy bands, and the correspondent refractive index modulation by the Kramers-Kronig formulas is called *band-filling effect*.

Bennett has reported a numerical model for the band-filling effect by calculating the absorption change occurring in a material for different free carrier concentrations, and by integrating the absorption according to the Kramers-Kronig formula [70]. Vinchant has shown, by means of Bennett results that the refractive index change due to the Band Filling effect is a linear function of the *N* (electrons) carrier concentration change [71]. The Vinchant formula used in this thesis to model the band-filling effect is

$$\Delta n_{Band\ Filling} = -A\Delta N \qquad (8)$$

Where A is a proportionality constant and ΔN is the electron density change expressed in cm^3. The constant A is $0.5 \times 10^{-20}\,\mathrm{cm}^3$ in InP at an optical wavelength on the order of 1.5 µm. The band-filling effect is much stronger in InGaAsP, for which A is $1.5 \times 10^{-20}\,\mathrm{cm}^3$ for a quaternary composition ($\mathrm{In_{1-x}Ga_xAs_yP_{1-y}}$) defined by $y = 0.5$. The wavelength dependence of the calculated *A* coefficient is shown in Figure 2-5 for InP and InGaAsP.

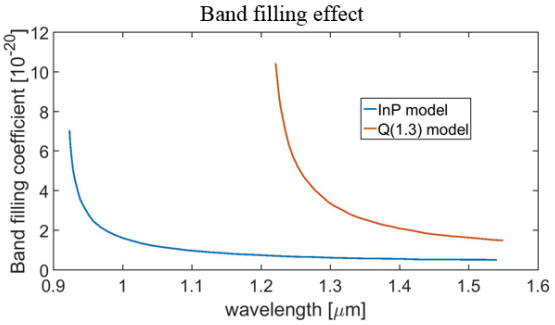

Figure 2-5. Wavelength dependence of the calculated *A* coefficient defining the band-filling effect.

2.3.2 Plasma effect

The plasma effect is the refractive index change due to a carrier density modulation. However, this is an *intraband phenomenon*, since involves energy states related to the same energy band. A change in the carrier density, either in the conduction or the valence band, affects the probability for an electron/hole to be excited from a state to another state of the same band, causing a free-carrier absorption coefficient variation. As for the band filling effect, the free-carrier absorption coefficient change can be converted into a refractive index change by using the Kramers-Kronig relations. The *intraband* process involved in the plasma effect is schematically represented in Figure 2-6.

Figure 2-6. Intraband processes involved in the plasma effect.

The Plasma effect is modelled by means of the classical dispersion theory and is defined by the equation [67]:

$$\Delta n_{Plasma} = -\frac{e^2\lambda^2}{8\pi^2 n\varepsilon_0 c^2}\left(\frac{\Delta N}{m_e} + \Delta P\frac{m_{hh}^{1/2} + m_{lh}^{1/2}}{m_{hh}^{3/2} + m_{lh}^{3/2}}\right) \qquad (9)$$

where e is the electron charge, λ is the vacuum wavelength, ε_0 is the vacuum permittivity, c is the speed of light in vacuum, N is the electrons concentration, P is the holes concentration, m_e is the effective electron mass, m_{hh} and m_{lh} are the

effective heavy hole and light hole masses. The effective masses m_{hh} and m_{lh} are calculated through the model reported in [72].

For both the band-filling and the free-carrier effects, a negative change of the refractive index occurs when injecting carriers in a semiconductor. Furthermore, both the carrier effects are isotropic. Experimental data for the current injected refractive index change is commonly reported as the sum of the band-filling and plasma effect, since the experimental separation of the two effects is challenging. The total refractive index modulation due to a change of the carrier density has been reported in [70] for a wavelength between 1 μm and 1.24 μm. This experimental data and the sum of the simulated band-filling and the plasma effects, from equations (8) and (9) respectively, are shown in Figure 2-7. The simulation results shown in Figure 2-7 are obtained at the wavelength of 1.1 μm. Agreement between experiments and the model is shown for an n-type concentration of $n = 10^{18}/\mathrm{cm}^3$. The model exhibits an overestimation of the refractive index change with respect to the experiments for higher carrier concentrations.

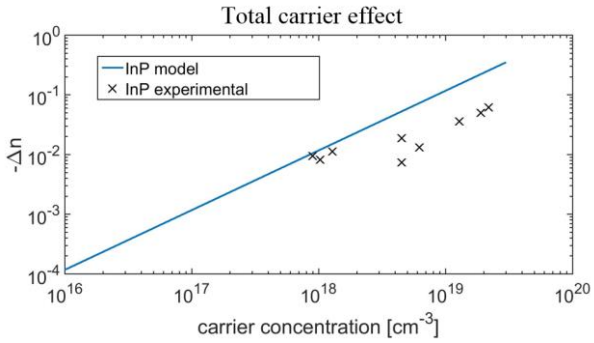

Figure 2-7. Refractive index modulation due to carrier injection effects. Experimental data from [70] for a wavelength included between 1 μm and 1.24 μm, and sum of the band-filling and plasma effect models at a wavelength if 1.1 μm.

2.4 Absorption coefficient modulation

Optical losses are modelled to understand the impact that the refractive index modulation has on the absorption coefficient of the perturbed material. Optical losses are modelled as the combination of the free-carrier absorption and electro-absorption effects.

2.4.1 Free-carrier absorption

Free-carrier absorption is the absorption mechanism related to the free-carrier electro-refraction. Free-carrier absorption in the p-type InP and n-type InP is considered. Free carrier absorption in InGaAsP is neglected as InGaAsP is only used with a low doping concentration in this work. The dominant absorption mechanism below bandgap for p-type InP is intervalence band transitions. The absorption in p-type InP is assumed to follow

$$\alpha_P = 4.252 \cdot 10^{-20}\, exp(-3.657\, E)\, P \quad [m^{-1}] \qquad (10)$$

where E is the photon energy in electron volts and P is the hole density expressed in m^{-3}. Equation (10) has been found empirically and is considered a good approximation for compositions of InGaAsP [73], and so it is used as an approximation for the free-carrier absorption in InP. The modelled absorption coefficient is shown in Figure 2-8 as a function of the wavelength, together with the experimental data reported in [74]. The plot is made for a p-carrier concentration of $p = 10^{18}/\mathrm{cm}^3$. The simulated data appear to overestimate the experimental losses across the considered wavelength range, however, good agreement is observed at the wavelength of 1.5 µm used in this thesis.

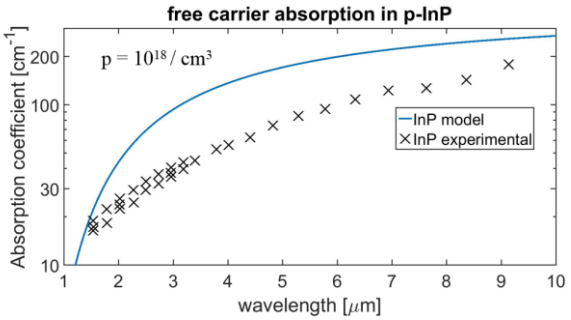

Figure 2-8. Free-carrier absorption coefficient for p-doped InP. Experimental data from [74] and model given in [73].

The free carrier absorption coefficient in the n-type InP is modelled as [75]:

$$\alpha_n = \alpha_{OP}(N)\left(\frac{\lambda}{\lambda_0}\right)^{3.5} + \alpha_{AC}(N)\left(\frac{\lambda}{\lambda_0}\right)^{2.5} + \alpha_{IMP}(N)\left(\frac{\lambda}{\lambda_0}\right)^{1.5} \quad [m^{-1}] \qquad (10)$$

where α_{OP}, α_{AC}, and α_{IMP} represent the electron-optical phonons, electro-acoustical phonons and electron-ionized impurity interactions at the reference

optical wavelength λ_0 of 10 μm, N represents the free-electrons density expressed in m^{-3}. The parameters α_{OP}, α_{AC}, and α_{IMP} are calculated through fitting of the measurements reported by Walukiewicz [75], by means of a polynomial function of order 8.

2.4.2 Franz-Keldysh effect

Electro-absorption is the change in absorption coefficient due to an applied electric field. An electric field has the effect of bending the conduction and valence bands of a semiconductor, causing a perturbation of the carrier wave functions. The perturbed wave functions for the electrons and holes exhibit a decaying behaviour in the band gap, resulting in an improvement of the overlap between the two wave functions. The result is a lower effective energy bandgap and an absorption modulation. The described electro-absorption mechanism is schematically shown in Figure 2-9.

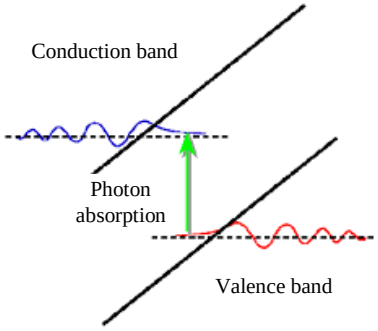

Figure 2-9. Schematic of the electro-absorption mechanism.

The explained electro-absorption mechanism is called Franz-Keldysh effect and the numerical model has been reported by [76]. The absorption coefficient due to the Franz-Keldysh effect is modelled by the following equations

$$\alpha_{EA}(\omega, E) = C\frac{\mu}{\omega}\frac{F}{E_g - \hbar\omega}\, e^{-\frac{4}{3}\eta^{\frac{3}{2}}}$$

$$\eta = \frac{E_g - \hbar\omega}{\hbar\varphi} \qquad (10)$$

$$\varphi = \left(\frac{(q\,F)^2}{\mu\,\hbar}\right)^{\frac{1}{3}}$$

where α_{EA} is the electro-absorption coefficient, E_g is the energy gap of the considered material [77], F is the static applied electric field amplitude, ω is the optical angular frequency, is the reduced Planck constant and q is the absolute electron charge. The constants C and μ are 0.2×10^{24} and $0.0016 \times m_0$ for InP, 2.5×10^{24} and $0.015 \times m_0$ for InGaAsP. m_0 is the electron mass. The constants C and μ are chosen to fit the measured absorption coefficient reported in [69]. The modelled absorption coefficient change for InP and InGaAsP is shown in Figure 2-10, together with the experimental data from [69]. Experimental results in [69] are defined for an optical wavelength of 1.53 µm. Figure 2-10 shows good agreement between the model and the experimental data up to an applied electric field of 200 kV/cm.

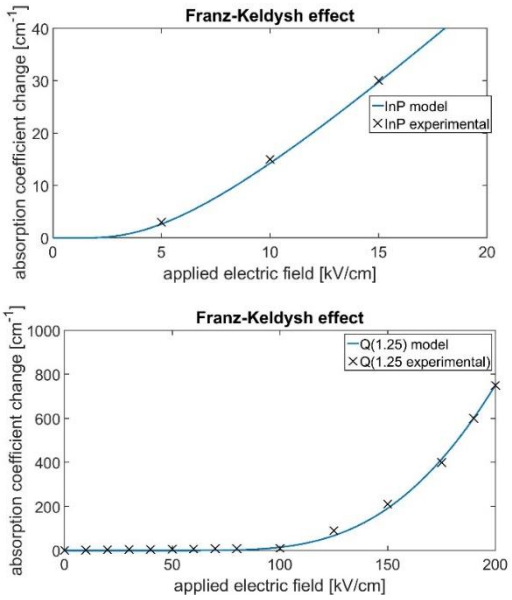

Figure 2-10. The modelled absorption coefficient changes for InP and InGaAsP. Experimental data from [69] and model given in [76].

2.5 Conclusions

A literature review of the effects enabling refractive index modulation in InP and InGaAsP materials has been performed in terms of analytical models and experimental data. Field induced refractive index change is modelled by considering the Pockels and Kerr effects. The electro-optical coefficients used to model the Pockels and the Kerr effects show agreement with the experimental data from literature at a wavelength of 1.3 µm and 1.5 µm, respectively. Refractive index

change from carrier density modulation is modelled by considering band-filling and plasma effects. The sum of the two models shows agreement with experimental results for an n-type carrier concentration of $n = 10^{18}/\mathrm{cm}^3$. The electro-absorption and free-carrier absorption have been modelled to understand how electro-refraction impacts the absorption coefficient in optical devices. The modelled electro-absorption agrees with experimental data from literature for InP and InGaAsP up to an applied electric field of 200 kV/cm. Agreement between experimental data from the literature and the analytical model for the free-carrier absorption has been shown at a wavelength of 1.5 μm and for a relatively high p-type doping concentration of $p = 10^{18}/\mathrm{cm}^3$. The presented analytical expressions for the refractive index and the absorption coefficient change will be used in chapter 4 to model an electronically actuated beam steering device.

3 Two-mode electro-optic beam steering[1]

The proposed beam steering mechanism is presented in this chapter. After introducing the schematic and the principle of operation, an analytical model of the device behaviour is developed to validate the concept, to identify the relevant design parameters, and to understand what steering range can be achieved.

3.1 Beam steering concept

The proposed beam steering concept is explained by defining the device structure in terms of geometry and materials first, and by introducing the effect of the refractive index perturbation later. A schematic 3D view of the proposed beam steering device is shown in Figure 3-1.

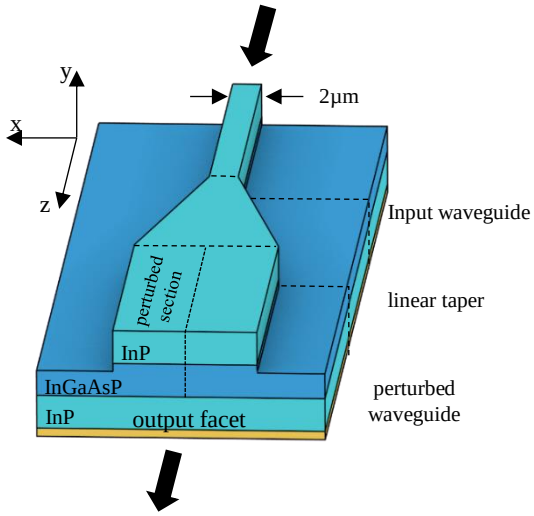

Figure 3-1. Schematic 3D view of the beam steering device.

The layer stack is composed by an InP top and bottom cladding, and an InGaAsP guiding layer. The input field is the zero-order mode of the *input waveguide*. The 2 µm wide *input waveguide* serves as connection with standard photonic components operating with a single mode. The input field expands through the adiabatic *linear taper* to match the mode size of the *perturbed waveguide*.

[1] The analytical model reported in this chapter has been developed by Simone Cardarelli, together with the support of Daan Lenstra.

The beam steering mechanism is based on achieving an asymmetric refractive index change across the *perturbed waveguide* cross section. This is performed by modulating the refractive index in half the waveguide, across the *perturbed section*. The optical field is expected to travel straight and unperturbed if the refractive index is not modulated, and 100 % the input power is coupled to the zero-order mode of the *perturbed waveguide*. However, a fraction of the input power couples to the first-higher order mode if refractive index modulation occurs. The modal evolution and interference of the perturbed zero- and first-higher order modes is the core mechanism to achieve lateral steering of the field intensity along the *perturbed waveguide*. The presented mechanism is here named two-mode beam steering.

3.2 Analytical model

The proposed steering mechanism is validated through an analytical model. The developed model is based on the calculation of the perturbed beam evolution in the *perturbed waveguide* (see Figure 3-1) when the input waveguide is excited with a fundamental mode. The analytical model is limited to the analysis of the *perturbed waveguide*, injected with an input field which is mode size expanded by the adiabatic taper. The perturbed modes are calculated by solving the Helmholtz equation for the *perturbed waveguide* cross section when the refractive index is tuned in a portion of the waveguide. The Helmholtz equation is solved through perturbation theory, by expressing the perturbed modes as a linear combination of a finite number of unperturbed modes. The relationship between the fundamental unperturbed mode and the perturbed modes represents the butt-coupling condition at the input of the *perturbed waveguide* and will be exploited to calculate the perturbed modal excitation and propagation. The beam steering is quantified by calculating the maximum intensity peak displacement of the propagated perturbed field.

3.2.1 2D approximation

The proposed beam steering device is studied through the approximated 2D model shown in Figure 3-2. The effective index in the W wide guiding layer equals 3.17, whereas the effective index in the left and right cladding is assumed to be sufficiently low to consider the optical modes strongly confined, as in a rectangular metal waveguide. The refractive index change is modelled as a Δn local perturbation of the effective index in half the waveguide and is defined as a rectangular function.

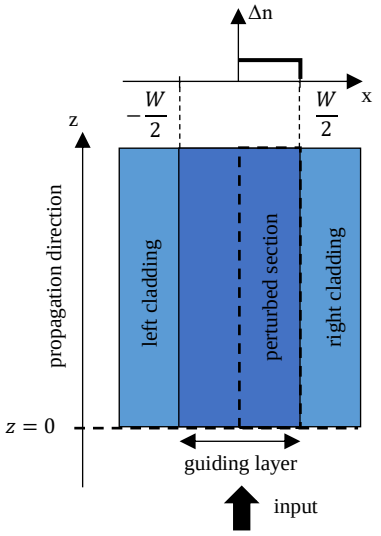

Figure 3-2. 2D approximation of the *perturbed waveguide*.

3.2.2 Perturbation model

The unperturbed Helmholtz equation ($\Delta n = 0$) describing the lateral modes in a slab waveguide is

$$\begin{aligned} \mathrm{H}\,\Psi_j &= \mathrm{E_j}\,\Psi_j \\ \mathrm{E_j} &= {k_0}^2 n^2 - \beta_j^2 \end{aligned} \tag{1}$$

Where $\mathrm{H} = -\frac{d^2(\cdot)}{dx^2}$, $\mathrm{E_j}$ is the unperturbed eigenvalue, k_0 is the vacuum wave vector, n is the effective index profile and β_j is the unperturbed propagation constant for the j-th mode. Ψ_j is the j-th unperturbed lateral mode and is expressed as

$$\begin{aligned} \Psi_j &= \sqrt{\frac{2}{W}}\cos\left(\frac{j\,\pi}{W}x\right) \quad j = 1, 3, 5, 7 \ldots \\ \Psi_j &= \sqrt{\frac{2}{W}}\sin\left(\frac{j\pi}{W}x\right) \quad j = 2, 4, 6, 8 \ldots \end{aligned} \tag{2}$$

$${\beta_{0/1}}^2 = {k_0}^2 n^2 - \mathrm{E}_{0/1}$$

The normalization factor $\sqrt{\frac{2}{W}}$ is introduced to achieve normalization of the modes to unity energy. A refractive index change $\Delta n(x)$ causes a perturbation in the Helmholtz equation. The perturbed Helmholtz equation is calculated by substituting $n + \Delta n(x)$ in the refractive index of the eigenvalue expression in (1), and by selecting the first- order term in the Taylor expansion with respect to $\Delta n(x)$ in the point $\Delta n = 0$. The perturbed Helmholtz equation is

$$(H + P)\,\tilde{\Psi} = \tilde{E}\,\tilde{\Psi} \qquad (3)$$

Where $\tilde{\Psi}$ is the perturbed mode, $\tilde{E}$ is the eigenvalue related to the perturbed mode and P(x) is given by

$$P(x) = \begin{cases} \frac{8\pi^2 n}{\lambda^2}\Delta n = \Delta H & 0 < x < \frac{W}{2} \\ 0 & -\frac{W}{2} < x < 0 \end{cases} \qquad (4)$$

The calculation of the perturbed modes is performed according to the perturbation theory guidelines [78]. The perturbed modes are expressed as linear combinations of the unperturbed modes, with coefficients that become the new unknowns. Initially, two unperturbed modes are considered in order to keep a low level of analytical complexity. The perturbed mode is expressed as

$$\tilde{\Psi} = \sum_{j=0}^{1} s_j \Psi_j \qquad (5)$$

The coefficients s_j can be derived by substituting $\tilde{\Psi}$ in the perturbed Helmholtz equation (3)

$$\sum_{j=0}^{1} s_j \left(E_j - \tilde{E} + P\right) \Psi_j = 0 \qquad (6)$$

Since the modes of an optical waveguide are orthonormal by definition, inner product with the unperturbed modes can be applied to equation (6) to derive the following linear system

$$\begin{aligned}\left[\left(\mathrm{E}_0-\widetilde{\mathrm{E}}\right)+\mathrm{P}_{00}\right]\mathrm{s}_0+\ \mathrm{P}_{10}s_1=0\\ \mathrm{P}_{01}s_0+\ \left[\left(\mathrm{E}_1-\widetilde{\mathrm{E}}\right)+\mathrm{P}_{11}\right]s_1=0\end{aligned} \tag{7}$$

The matrix elements $\mathrm{P_{jk}}$ are given by the following internal product between the unperturbed modes

$$\mathrm{P_{jk}}=\Delta\mathrm{H}\int_0^{\frac{\mathrm{W}}{2}}\Psi_\mathrm{j}\Psi_\mathrm{k}\,\mathrm{dx} \tag{8}$$

Using the mode expressions given in (2), $\mathrm{P_{jk}}$ is expressed as $\mathrm{P_{00}}=\mathrm{P_{11}}=\frac{1}{2}\Delta\mathrm{H}$, $\mathrm{P_{01}}=\mathrm{P_{10}}=-\frac{4\Delta\mathrm{H}}{3\pi}$. The linear system in (7) is re-defined in order to simplify the formalism:

$$\begin{pmatrix}\mathrm{a}-\widetilde{\mathrm{E}} & \mathrm{b}\\ \mathrm{b} & \mathrm{c}-\widetilde{\mathrm{E}}\end{pmatrix}\begin{pmatrix}\mathrm{s}_0\\ \mathrm{s}_1\end{pmatrix}=0 \tag{9}$$

Where $\mathrm{a}=\frac{1}{2}\Delta\mathrm{H}+\ \mathrm{E}_0$, $\mathrm{c}=\frac{1}{2}\Delta\mathrm{H}+\ \mathrm{E}_1$ and $\mathrm{b}=-\frac{4\Delta\mathrm{H}}{3\pi}$. The linear system in (9) is homogenous and admits solution if the determinant of the coefficient matrix is zero. The determinant of the coefficient matrix is a second order equation with $\widetilde{\mathrm{E}}$ unknown:

$$\widetilde{\mathrm{E}}^2-(\mathrm{a}+\mathrm{c})\widetilde{\mathrm{E}}+\mathrm{ac}-\mathrm{b}^2=0 \tag{10}$$

The two solutions for the perturbed eigenvalue are

$$\begin{aligned}\widetilde{\mathrm{E}}_{0/1}&=\frac{\mathrm{a}+\mathrm{c}\ \pm\sqrt{(\mathrm{a}+\mathrm{c})^2-4(\mathrm{ac}-\mathrm{b}^2)}}{2}\\ &=\frac{\mathrm{E}_0+\mathrm{E}_1+\Delta\mathrm{H}\pm\sqrt{(\mathrm{E}_0-\mathrm{E}_1)^2+4\left(\frac{4\Delta\mathrm{H}}{3\pi}\right)^2}}{2}\end{aligned} \tag{11}$$

$\widetilde{\mathrm{E}}_0$ is the perturbed eigenvalue by taking the minus sign, whereas $\widetilde{\mathrm{E}}_1$ is identified by the plus sign. Note that in absence of perturbation, that is $\Delta\mathrm{n}=\ \Delta\mathrm{H}=0$, the perturbed eigenvalues coincide with the unperturbed cases. The perturbed

modes can be calculated by substituting $\widetilde{\mathrm{E}}_{0/1}$ in (9). Since $\widetilde{\mathrm{E}}_0 = \mathrm{E}_0$ and $\widetilde{\mathrm{E}}_1 = \mathrm{E}_1$ for $\Delta\mathrm{H} = 0$, the perturbed modes related to $\widetilde{\mathrm{E}}_0$ and $\widetilde{\mathrm{E}}_1$ are here defined as perturbed zero-order mode and perturbed first-order mode, respectively. Two couples of coefficients $\{\mathrm{s}_{00}, \mathrm{s}_{01}\}$ for $\widetilde{\Psi}_0$ and $\{\mathrm{s}_{10}, \mathrm{s}_{11}\}$ for $\widetilde{\Psi}_1$ can be derived for each perturbed eigenvalue. The i index of s_{ij} is related to the i-th perturbed mode whereas the j index is related to the j-th unperturbed mode. For $\widetilde{\mathrm{E}} = \widetilde{\mathrm{E}}_0$, the relation between s_{00} and s_{01} is found (use (9)):

$$s_{01} = \frac{\mathrm{b}}{\widetilde{\mathrm{E}}_0 - c} s_{00} = \frac{\frac{8\Delta\mathrm{H}}{3\pi}}{\mathrm{E}_1 - \mathrm{E}_0 + \sqrt{(\mathrm{E}_0 - \mathrm{E}_1)^2 + 4\left(\frac{4\Delta\mathrm{H}}{3\pi}\right)^2}} s_{00} \tag{12}$$

Similarly, for $\widetilde{\mathrm{E}} = \widetilde{\mathrm{E}}_1$, the relation between s_{10} and s_{11} is found:

$$s_{10} = \frac{\mathrm{b}}{\widetilde{\mathrm{E}}_1 - a} s_{11} = \frac{\frac{8\Delta\mathrm{H}}{3\pi}}{\mathrm{E}_0 - \mathrm{E}_1 - \sqrt{(\mathrm{E}_0 - \mathrm{E}_1)^2 + 4\left(\frac{4\Delta\mathrm{H}}{3\pi}\right)^2}} s_{11} \tag{13}$$

The final relation between the two perturbed modes and the unperturbed modes can be expressed as:

$$\widetilde{\Psi}_0 = s_{00}\Psi_0 + s_{01}\Psi_1 \qquad \widetilde{\Psi}_1 = s_{10}\Psi_0 + s_{11}\Psi_1 \tag{14}$$

In order to normalize the perturbed modes to unity as well, we multiply the coefficients in (12) and (13) with a fixed real number such that

$$|s_{00}|^2 + |s_{01}|^2 = 1 \qquad |s_{10}|^2 + |s_{11}|^2 = 1 \tag{15}$$

Notice that after normalization, the matrix s_{ij} becomes real and unitary, that is ${s_{ij}}^{-1} = \left({s_{ij}}^{*}\right)^{T}$. Since s_{ij} is real and unitary, the determinant of s_{ij} equals 1. Furthermore, the relation $s_{00} = s_{11}$ and $s_{01} = -s_{10}$ exist among the matrix coefficients. The unperturbed modes can be expressed in the perturbed modes by inverting the relation in equation (14):

$$\begin{aligned} \Psi_0 &= \tilde{s}_{00}\tilde{\Psi}_0 + \tilde{s}_{01}\tilde{\Psi}_1 \\ \Psi_1 &= \tilde{s}_{10}\tilde{\Psi}_0 + \tilde{s}_{11}\tilde{\Psi}_1 \end{aligned} \qquad (16)$$

where the matrix $\tilde{s}_{ij}$ is the inverse of s_{ij}. The first equation of (16) represents the butt-coupling condition at the interface between the taper output section and the *perturbed waveguide* and will be used to calculate the perturbed modes excitation in next section. Because of the unitary matrix properties, the relation between s_{mn} and the inverted matrix $\tilde{s}_{mn}$ is:

$$\tilde{s}_{mn} = \begin{pmatrix} s_{00} & s_{01} \\ s_{10} & s_{11} \end{pmatrix}^{-1} = \begin{pmatrix} s_{11} & -s_{01} \\ -s_{10} & s_{00} \end{pmatrix} \qquad (17)$$

The propagation constant of the two modes is calculated by substituting the perturbed eigenvalues in (1), and is expressed as

$$\tilde{\beta}_{0/1}{}^{2} = k_0{}^{2}n^{2} - \tilde{E}_{0/1} \qquad (18)$$

3.2.3 Analytical beam steering formula

The calculated perturbed modes and the related perturbed propagation constants are here exploited to compute the full beam propagation in the perturbed waveguide and the final beam steering formula. The fundamental mode Ψ_0 is injected into the perturbed waveguide, and a waveguide width of 14.5 μm is here assumed to provide comparison with the experimental results reported in next chapters. It is assumed that no reflections occur at the taper/perturbed waveguide interface and that all the input optical power is coupled to the perturbed modes. Neglecting reflections at the taper/*perturbed waveguide* interface is motivated by the fact that a small refractive index perturbation generates small reflections between the unperturbed and perturbed waveguides. The formula for the reflection coefficient between two mediums with different refractive index is $R \cong \left(\frac{n_2 - n_1}{n_2 + n_1}\right)^2$, which is negligible when a small perturbation is present between the two refractive indices.

The input field Ψ_0 enters the perturbed waveguide at z = 0 (see Figure 3-2) and couples to the zero- and first- order perturbed modes according to the first equation of (16). The excited perturbed modes propagate with the propagation constants calculated in (18), and the total field at a generic propagation distance z from the input of the *perturbed waveguide* is

$$\begin{aligned}\widetilde{\Psi}_{\text{total}}(z) &= \tilde{s}_{00}\widetilde{\Psi}_0 e^{-i\beta_0 z} + \tilde{s}_{01}\widetilde{\Psi}_1 e^{-i\beta_1 z} \\ &= s_{11}\widetilde{\Psi}_0 e^{-i\beta_0 z} - s_{01}\widetilde{\Psi}_1 e^{-i\beta_1 z}\end{aligned} \tag{20}$$

Notice that when z is 0, the equation (20) is exactly the first equation of (16). The impact of the refractive index modulation on the perturbed field propagation is studied by looking at the intensity distribution of the field $\widetilde{\Psi}_{\text{total}}(z)$, shown in Figure 3-3 for a refractive index change of 0.001. Figure 3-3 has been created by calculating the field intensity $\left|\widetilde{\Psi}_{\text{total}}(z)\right|^2$ and by normalization with respect to the maximum value of the field intensity at $z = 0$. The shown intensity distribution is expressed in dB and limited between -6 dB and 1.5 dB.

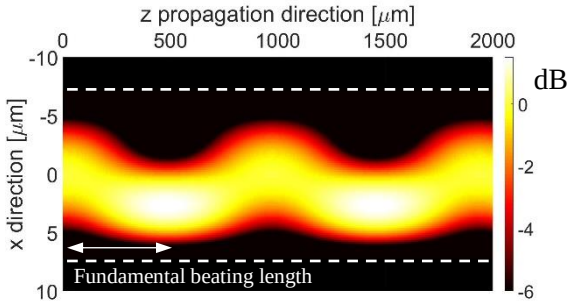

Figure 3-3. Colormap of the intensity distribution of the optical field propagating along the perturbed waveguide($\Delta n = 0.001$).

The field intensity distribution exhibits a periodic pattern, and the period relates to the beating between the zero- and the first- higher order modes, for which optimal lateral beam steering is observed. The beating length between the zero- and the first- order perturbed modes is defined by the distance for which a π phase propagation difference between the two modes occurs. The following is the expression of the perturbed beating length:

$$\tilde{L}_b = \frac{\pi}{\tilde{\beta}_1 - \tilde{\beta}_0} \tag{21}$$

A beating length of the order of 480 μm is observed in Figure 3-3. The beating length depends on the refractive index change and decreases when the refractive index is modulated. The beating length for different refractive index changes is shown in Figure 3-4.

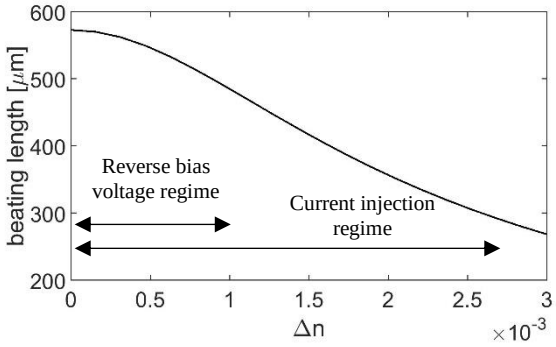

Figure 3-4. Beating length for different refractive index changes.

The beating length in Figure 3-4 shows that the final device length depends on the available refractive index change. A low level of refractive index change, up to 0.001, can be addressed through reverse bias voltage modulation [79], however current injection may be needed for higher refractive index modulation [80] in order to achieve larger steering. The possibility of achieving larger steering implies a reduction of the device length as the beating length decreases for large refractive index change.

The beam steering is studied by analysing the propagating field at the beating length, for which maximum beam steering is observed. The total field at the beating length is expressed by using the equations (20) and (21)

$$\tilde{\Psi}\left(\tilde{L}_b\right) = s_{11}\tilde{\Psi}_0 e^{-i\tilde{\beta}_0\tilde{L}_b} - s_{01}\tilde{\Psi}_1 e^{-i(\tilde{\beta}_0\tilde{L}_b-\pi)} \qquad (22)$$

The phase term $e^{-i\tilde{\beta}_0\tilde{L}_b}$ is a constant phase term and is assumed equal to 1. The total field at the beating length can be rewritten as a real quantity

$$\tilde{\Psi}\left(\tilde{L}_b\right) = (s_{11}\tilde{\Psi}_0 + s_{01}\tilde{\Psi}_1) \qquad (23)$$

The interference in (23) between $\tilde{\Psi}_0$ and $\tilde{\Psi}_1$ causes a steering of the total field intensity, which is shown in Figure 3-5 for the perturbation Δn = 0.001.

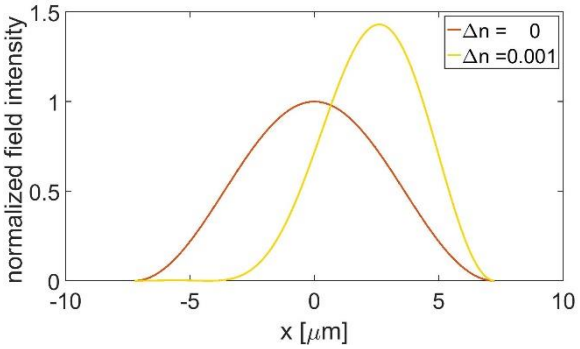

Figure 3-5. Total field intensity for Δn = 0 (red curved) and Δn = 0.001 (yellow curve). The output fields are selected at different beating lengths $\tilde{L}_b(\Delta n)$.

A lateral displacement of the field intensity is observed, together with a shrinkage of the intensity profile size. The beam steering is calculated by rewriting the perturbed modes in terms of unperturbed modes by means of (14):

$$\tilde{\Psi}(\tilde{L}_b) = s_{11}(s_{00}\Psi_0 + s_{01}\Psi_1) + s_{01}(s_{10}\Psi_0 + s_{11}\Psi_1) = \\ = (s_{11}s_{00} - {s_{10}}^2)\Psi_0 + 2s_{11}s_{01}\Psi_1 \quad (24)$$

where $(s_{11}s_{00} - {s_{10}}^2)$ is named A and $(2s_{11}s_{01})$ is named *B*. Notice that both *A* and *B* are real quantities since functions of the real s_{ij} matrix coefficients. By using the analytical form of the unperturbed modes, we can write the following expression:

$$\tilde{\Psi}(\tilde{L}_b) = \sqrt{\frac{2}{W}} A \cos\left(\frac{\pi}{W}x\right) + \sqrt{\frac{2}{W}} B \sin\left(\frac{2\pi}{W}x\right) \quad (25)$$

The equation in (25) represents the sum of a cosine field profile (unperturbed fundamental mode) and a weighted sine profile (unperturbed first- higher order mode) oscillating with double spatial frequency. The *B* coefficient is zero when $\Delta n = 0$ and slowly increases when the refractive index perturbation is perturbed. The field $\tilde{\Psi}_L(L_b)$ results in a slightly perturbed version of the cosine term for a low enough refractive index change, and the field maximum position coincides with the maximum position of the intensity profile. To analytically calculate the optical beam

steering in terms of field intensity peak displacement we look for local maxima points of the total field. The field local maxima points are obtained by setting to zero the derivative of equation (25):

$$\frac{d\,\tilde{\Psi}_L(\mathrm{L}_b)}{dx} = \sqrt{\frac{2}{W}}\left[-\frac{\pi}{W}\mathrm{A}\sin\left(\frac{\pi}{W}x\right) + B\frac{2\pi}{W}\cos\left(\frac{2\pi}{W}x\right)\right] = 0 \qquad (26)$$

$$\Rightarrow \mathrm{A}\sin\left(\frac{\pi}{W}x\right) - 2B\cos\left(\frac{2\pi}{W}x\right) = 0$$

Let's perform the substitution $\frac{\pi}{W}x = u$:

$$\mathrm{A}\sin(u) - 2B\cos(2u) = 0 \qquad (27)$$

The term $\cos(2u)$ can be expressed through trigonometry as $\cos(2u) = 1 - 2sin^2(u)$ and the previous equation becomes:

$$4B\,sin^2(u) + \mathrm{A}\sin(u) - 2B = 0 \qquad (28)$$

The solution of the quadratic equation in (28) is:

$$u = \arcsin\left(\frac{-A \pm \sqrt{A^2 + 32\,B^2}}{8B}\right) \qquad (29)$$

At L=$\tilde{\mathrm{L}}_\mathrm{b}$. The real solution is provided by the sign + and the actual beam steering formula can be expressed by re-substituting $\frac{\pi}{W}x = u$:

$$x = \frac{W}{\pi}\arcsin\left(\frac{-A + \sqrt{A^2 + 32\,B^2}}{8B}\right) \qquad (30)$$

Figure 3-6 shows the beam peak displacement x for different Δn perturbations. The curve in Figure 3-6 is anti-symmetrical for a negative refractive index change.

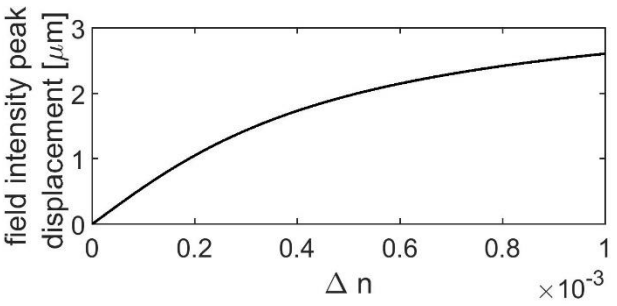

Figure 3-6. Peak displacement of the total field intensity profile for different refractive index perturbations and hence at different length $L=\tilde{L}_b(\Delta n)$.

The behaviour of the displacement for low and high Δn can be studied by calculating the limits of the beam steering for low and high perturbation. When Δn goes to zero, the displacement can be written as:

$$\lim_{\Delta n \to 0} x = -W^3 \frac{n\,\Delta n}{(\pi\,\lambda)^2}\,\frac{128}{9} \qquad (31)$$

The displacement is a linear function of the perturbation and depends on the cubic of the waveguide width. When Δn goes to infinite, the displacement saturates up to the following value

$$\lim_{\Delta n \to \infty} x = \frac{W}{4} \qquad (32)$$

The beam steering formula is calculated by considering the position of the maximum field intensity at the perturbed beating length, which is varying with the refractive index perturbation. However, a realistic device has fixed length, and a study of the beam steering at a fixed cross section is performed.

Beam steering at a fixed cross section

Beam steering is calculated at a distance of 500 μm inside the *perturbed waveguide* and compared with the beam steering calculated at the perturbed beating length, to understand the relationship between the practical and the idealized condition. The 500 μm length of the perturbed waveguide is chosen to provide comparison also with the experimental work in chapter 4. Beam steering at the distance of 500 μm is obtained numerically by calculating $\left|\tilde{\Psi}_L(500\ \mu\text{m})^2\right|$ and by detecting the maximum position. Beam steering at a fixed section and at the

perturbed beating length are shown in Figure 3-7 for a refractive index perturbation of up to 3×10^{-3}.

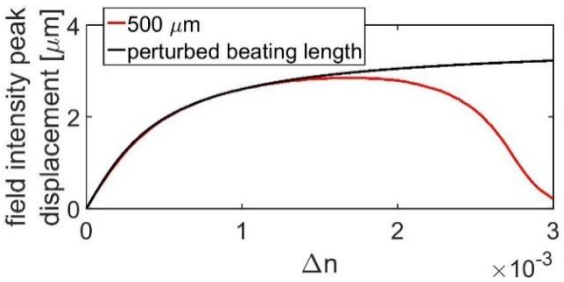

Figure 3-7. Beam steering for a perturbed waveguide length of 500 µm (red curve), and the beam steering calculated at the perturbed beating length (black curve).

The two curves present the same behaviour for a refractive index lower than 1.5×10^{-3}. The beam steering at fixed length becomes lower for higher Δn, whereas the beam steering at the perturbed beating length keeps on increasing towards the calculated limit in (32). The beam steering at 500 µm becomes lower for high Δn because the perturbed beating length becomes half the device size, and an image of the symmetric input field is present at the output section. Even though the beam steering calculated at the perturbed beating length cannot be practically implemented, it still gives important inputs since it represents the upper bound of the beam steering for a real device case.

Comparison between two-mode and n-mode calculation

The developed two-mode model enables the possibility of understanding how geometrical and physical parameters affect the optical beam steering, with relatively simple formulas. However, multiple modes might be excited in a realistic perturbed waveguide, leading an n-mode beam steering study to understand the level of accuracy of the two-mode approximation. Beam steering by considering multiple modes in the perturbed waveguide is numerically calculated by adapting equations (2), (5) and (6) for a larger number of modes. The perturbed eigenvalues and s_{ij} coefficients are numerically calculated. The beam steering for a realistic device 500 µm long is shown in Figure 3-8 for a number of considered unperturbed/perturbed modes up to 8.

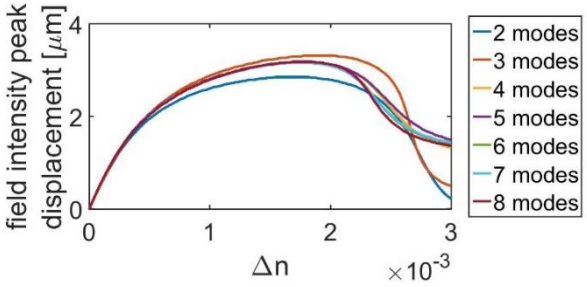

Figure 3-8. Beam steering at 500 μm for a larger number of modes.

Beam steering can be modelled by considering two modes for a refractive index change lower than 0.5×10^{-3}, but it still represents a qualitative description of the beam steering for high perturbation. The results start to convergence for a number of modes larger than three. The power coupled to the perturbed zero- and first- higher order mode is 70 % and 25 % the total input power for a refractive index change of 3×10^{-3} and eight considered modes.

3.3 Conclusions

A lateral steering of the optical field propagating in a waveguide can be enabled by tuning the refractive index in half the waveguide. A continuous beam steering is achieved by exploiting interference between the zero- and the first- higher order modes and the optimal operation is achieved at the perturbed fundamental beating length. The maximum beam steering tuning range is proportional to the waveguide width, whereas the maximum beam steering gradient is a cubic function of the waveguide width. Comparison with a generalized model based on a larger number of modes has been performed to show that the two-mode model gives good qualitative understanding of the proposed beam steering mechanism.

The possibility of achieving beam steering with either positive and negative refractive index change is interesting to implement devices based on reverse bias voltage control (towards low power consumption) or current injection (for extended tuning range), respectively. Reverse bias voltage and current injection enable two different ranges of refractive index change, and two different designs are needed for optimal steering since the beating length varies with the refractive index perturbation (see Figure 3-4).

Refractive index modulation has been employed in this chapter as control parameter to achieve beam steering, however, it is not clear yet what physical mechanisms in InP/InGaAsP materials can enable the needed refractive index

modulation. The physical mechanisms capable of enabling a refractive index modulation in InP/InGaAsP materials are presented in chapter 3.

4 Voltage driven electro-optical beam steering[2]

4.1 Introduction

The possibility of achieving beam steering by applying reverse bias voltage to a single p-i-n InP/InGaAsP waveguide is explored in this chapter. An electrical configuration providing practical control of the refractive index is proposed and tested through simulations and experiments. Electrical, electro-optical and optical simulations are performed by combining commercial simulation tools with the electro-refraction model developed in chapter 2, in order to validate the idealized steering concept and to achieve a more accurate device understanding. A prototype beam steering device is designed and tested in terms of near field characterization.

The possibility of achieving digital beam steering is numerically investigated by proposing the design of an optical switch based on the steering mechanism and reverse bias voltage control.

4.2 Reverse bias voltage driven steering device

A schematic 3D view of the proposed electronically controlled beam steering device is shown in Figure 4-1. The perturbed waveguide consists of a multimode ridge waveguide with on top two symmetrical electrodes. The InGaAsP optical guiding layer is confined by two InP cladding layers. The p++/p contact layers ensure efficient electro-optic modulation, but electrical isolation is required between the close-proximity electrodes. Simulations are performed for both a *high-isolation* and a *low-isolation* condition. The idealized high-electrical-isolation condition assumes that the two electrodes act as independent phase modulators with the top claddings separated by an intrinsic semiconductor region. This level of isolation might be achieved through selective area doping [59], regrowth [81], or ion implantation [82]. A *low-isolation* condition is considered where we assume that only the p++ layer is removed by etching between the electrodes as shown in Figure 4-1, providing a close match to the experimental work presented in section V.

[2] The fabrication of the chips employed for writing this chapter has been performed by SMART Photonics whereas the measurements and simulation have been performed by Simone Cardarelli.

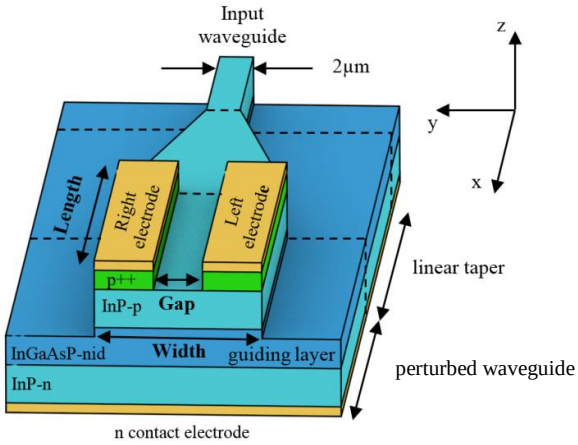

Figure 4-1. Schematic 3D view of the beam steering device.

4.2.1 Two dimensional reverse bias voltage simulation

The electrical simulation is performed by *Device* (*Lumerical*), provided with a Drift-Diffusion and Poisson solver. Under the assumption of infinitely long electrodes, the electric field and the charge-carrier densities are calculated for the cross section of the steering waveguide. The waveguide cross section is defined in terms of geometry, materials, doping profile and voltage excitation of the electrodes [79]. The shallow ridge geometry is defined by etched trenches 100 nm deep into the guiding layer. The InGaAsP guiding layer has a bandgap wavelength of 1.25 µm. This non-intentionally-doped layer is modelled with an n-doping concentration of 1×10^{16} cm^{-3}, representative of a realistic background n type doping. Asymmetric excitation of the guiding layer is performed by simulating a voltage sweep, ranging from 0 V to -10 V with a 1 V step, applied to one of the two p-electrodes. The second p-electrode and the n contact electrode are set to 0 V. A perfect Ohmic contact is assumed between the semiconductor and the electrodes. The vertical component of the electric field and the charge carrier density profile are exported into the electro-optic model to calculate the induced refractive index change across the device 2-D cross section. The simulation tool enables the calculation of the operational leakage current per unit length flowing between the p-electrodes for the two isolation conditions.

The optical beam propagation is simulated by using FIMMPROP (*Photon Design*). The unperturbed device cross-section is combined with the spatially-resolved refractive index perturbation to model the steering waveguide in Figure 4-1 for different voltage conditions. The output beam of the complete optical structure is

monitored in terms of beam waist and displacement. The polarization dependence of the device is studied by launching the TE and TM zero-order modes into the simulated steering section. In this work we assume that the first ten modes are sufficient to accurately describe the optical propagation. The top cladding is sufficiently thick to allow the role of the electrodes to be neglected in the optical cross section.

Asymmetric electric field induction

Simulations are compared for *high-* and *low-isolation* conditions in Figure 4-2. The electric field is shown for devices with a waveguide width of 15 μm and electrode gap of 7.5 μm, when the right electrode is biased with a voltage of -10 V. The white solid lines represent the waveguide to air interface and the white dashed lines indicate the epitaxial interface for the waveguide guiding layer. The white rectangles at the top left and top right of the waveguide represent the electrical contacts. The static electric field is laterally confined to the right side of the guiding layer. The maximum electric field in the middle plane of the guiding InGaAsP layer is 118 kV/cm for both designs.

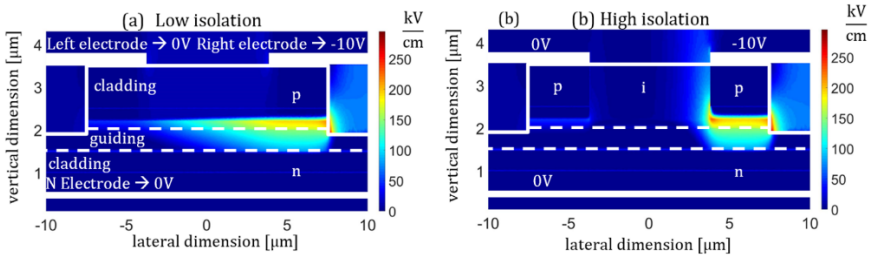

Figure 4-2. Electric field magnitude for a) *low-isolation* design and b) *high-isolation* design.

The current per unit length flowing between the two p-electrodes is 1.2 mA/μm in the *low isolation* device but this reduces to 8 fA/μm in the *high isolation* device.

Asymmetrical refractive index modulation

The local refractive index change is calculated to model how the electrical isolation affects the spatially resolved refractive index profile. Figure 4-3 shows the total refractive index variation taken at the center of the optical guiding layer at an optical wavelength of 1550 nm. The black dashed lines represent the waveguide edges. The extent of the refractive index perturbation beyond the waveguide edges is due to the static electric field extending beyond the shallow-etched ridge waveguide. The maximum refractive index change is 8×10^{-4} and 7×10^{-4} respectively for the TE

and TM polarizations and for both the *high-* and *low-isolation* designs. The refractive index modulation in the *low-isolation* device presents a smooth transition between the two electrodes whereas a step profile is achieved for the *high-isolation* device right underneath the excited electrode.

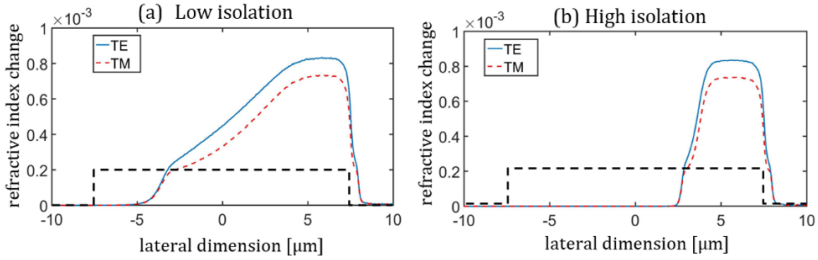

Figure 4-3. Total refractive index change for both polarizations for a) *low-isolation* design and b) *high-isolation* design. A bias voltage of -10 V is applied to the right electrode and 0 V is applied to the left electrode.

Pockels, Kerr, Band-filling and Plasma effects are separately analysed to compare field and carrier based refractive index perturbation. The comparison between the considered electro-optic effects is performed by locally monitoring the refractive index change underneath the excited p-electrode. This analysis holds for both the *high* and *low* isolation devices since they exhibit the same static field amplitude right underneath the excited electrode.

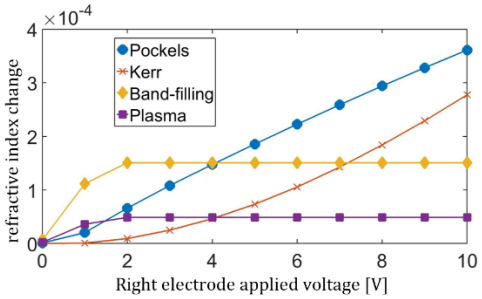

Figure 4-4. Refractive index change due to Pockels, Kerr, Band-filling and Plasma effects, for the TE case.

Figure 4-4 shows the refractive index change according to the four considered contributions, for a waveguide width of 15 µm and TE polarization. The Band-filling and the Plasma effects are dominant at low voltage, saturation occurs for a bias voltage larger than 2 V since the guiding layer becomes completely depleted. Carrier effects represent a 24 % of the total refractive index change at 10 V. The

Kerr effect becomes comparable with the Pockels contribution for high bias voltage values.

4.2.2 Perturbed optical beam propagation

Beam steering is studied by monitoring the optical energy density distribution along the steering waveguide. The *low isolation* design is considered in this paragraph to qualitatively understand the relation between optical energy distribution, beam steering and electrode length, while a quantitative comparison with the *high-isolation* design will be performed at the end of this sub-section. The top view energy density distribution of the propagating optical beam in the *low-isolation* steering waveguide is shown in Figure 4-5 when -10 V is applied to the right electrode. The two electrodes are schematically defined by the dashed lines and the white solid lines represent the ridge waveguide. The optical energy density is normalized with respect to the peak optical input value.

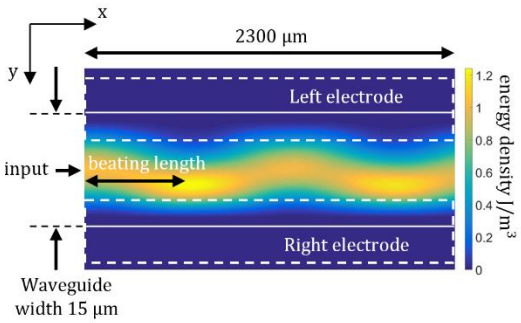

Figure 4-5. Top view energy density distribution along the steering waveguide when -10 V is applied to the right electrode in the *low-isolation* case.

Figure 4-5 shows a characteristic longitudinal beat length of the order of 600 µm corresponding to the beating between the fundamental and the first- higher order mode. An effective refractive index of 3.2851 and 3.2813 is calculated for the TE zero- and first- order modes. An output probe allows for mode decomposition to show that a 3% worst case of the total input power is coupled to the first-higher order mode. The power content in the remaining higher order modes is predicted to be less than 0.032 % worst case.

Optical simulations are also performed for waveguide widths of 5, 10, 15 and 20 µm, in order to explore the design space in terms of relationship between beam steering and the geometrical device parameters. The spacing between the electrodes is half the waveguide width for all the cases. Figure 4-6 shows the beam displacement at the output facet in terms of peak displacement versus electrode

length for the *low-isolation* device. A voltage of -10 V is applied to the steering electrode and the TE polarized input field is considered. The dashed line, labelled as operation line, shows the maximum beam steering obtained for each waveguide width for the range of electrode length at -10 V. The local maximum points of the steering curves show a tolerant steering operation with respect to the electrode length.

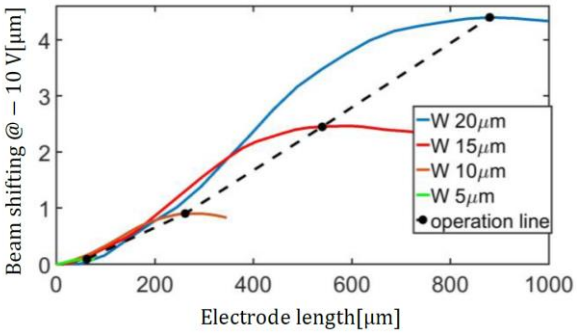

Figure 4-6. Optical peak intensity displacements (TE) at -10 V as a function of electrode length for four waveguide widths in the *low isolation* case.

The optical beam profile is monitored at the output facet of the device in order to understand how the output beam is shaped as a result of the local refractive index perturbation and the modal interference. Figure 4-7 shows the horizontal optical field profile extracted from the middle of the guiding layer at the output facet of the steering device for an optimum electrode length of 540 μm. The optical near field distributions are shown for three different voltage configurations in Figure 4-7:

1. Both the p-electrodes are biased with 0 V (red curve),
2. -10 V is applied to the right electrode and 0 V is applied to the left electrode (blue curve),
3. -10 V is applied to the left electrode and 0 V is applied to right electrode (green curve).

When no excitation is applied (red curve) the output profile is symmetric. The biasing of only one of the p-electrodes leads to an asymmetric beam and a steering toward the excited electrode. The asymmetric profiles present a maximum peak energy density increase of 22 (14) % and maximum full width half maximum (FWHM) decrease of 25 (12) % for the TE (TM) polarization.

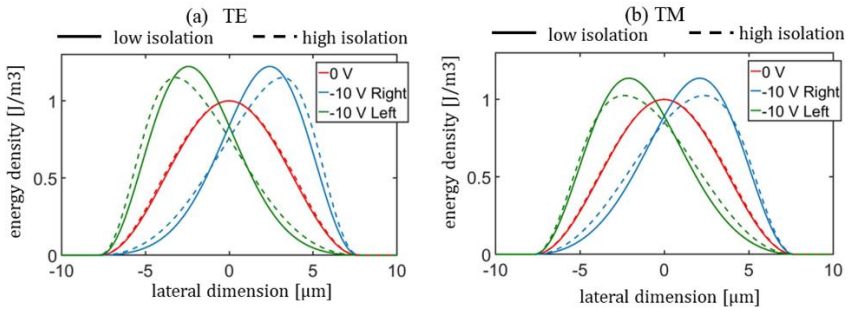

Figure 4-7. Energy density output profiles for the *low isolation* and the *high isolation* design for a) TE and b) TM polarization. A bias voltage of 10 V is applied.

Optical and electrical performance of the *high-* and *low- isolation* designs with varied width/length combinations is summarized in Table 4-1.

Width [µm]	Gap [µm]	Length [µm]	*Low isolation* current[A]	*High isolation* current[A]	*Low isolation* steering[µm]	*High isolation* steering[µm]
5	2.5	62	0.18	2.8×10^{-7}	0.09	0.12
10	5	262	0.46	4×10^{-10}	0.91	0.99
15	7.5	540	0.66	0.45×10^{-12}	2.45	2.46
20	10	880	0.82	1×10^{-12}	4.4	4.9

Table 4-1. Beam steering for one electrode at -10V.

The beam steering is quantified in terms of energy peak displacement of the output profiles for one electrode. The current is reported for the steering electrode biased with -10 V. The layouts are identified with the geometrical parameters defined in Figure 4-1: waveguide width (Width), gap between the electrodes (Gap) and electrode length (Length).

The *low isolation* device draws a leakage current of hundreds of mA, flowing in between the p-electrodes, which scales linearly with the device length and the electrode gap. The most critical design parameter is the waveguide width of the steering section since it defines the maximum beam displacement, FWHM, the electrode length and the electrical power consumption. Higher beam steering is achieved with wider waveguides at the expense of a longer device and higher current consumption.

In the *high isolation* design, the current flowing between the p-electrodes is six orders of magnitude lower with respect to the *low isolation* case. This is attributed to the high resistive path of the intrinsic region in the p-i-p doped top cladding. The type of electrical isolation does not affect significantly the optical

beam steering as indicated by the comparable *low* and *high-isolation* steering values. A best case total beam steering of 4.9 μm is predicted for an electrical power consumption of 4.5 pW for the *high-isolation* case with a 15 μm wide waveguide. The maximum observed optical loss at -10 V, due to carrier and electro-absorption, is of the order of -0.16 dB, for the TE case and a waveguide width of 20 μm.

4.2.3 Impact of the input modal purity

The wide multimode steering section is coupled to a 2 μm wide input waveguide by means of an adiabatic taper. The 2 μm wide input waveguide can guide both the fundamental and first-higher order mode. The impact of the input multi modal content is studied by launching different combinations of the fundamental and first-higher order modes into the adiabatic taper. The taper is 800 μm long and matches the input mode size to a waveguide width of the order of 15 μm.

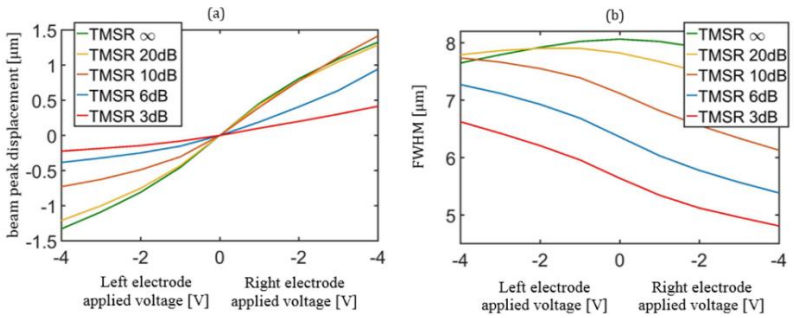

Figure 4-8. a) Beam peak displacement and b) FWHM for different TMSR.

The power ratio of the two launched modes, defined in this work as the transverse mode suppression ratio (TMSR), is varied between 3 dB and 20 dB while the phase relationship between the two input modes is fixed at zero. A TMSR equal to ∞ represents the pure fundamental mode launching condition. The impact of the first-higher order mode is quantified by monitoring the peak displacement of the output beam and the beam size, expressed as FWHM, when voltage is applied to the steering electrodes. The voltage applied to the *right* and *left* electrodes is swept from 0V to -4 V to provide a comparison with the experimental results in the next section. Figure 4-8a shows the simulated peak intensity displacement for a range of TMSR values. For a TMSR higher than 20 dB (1 % of total input power coupled to the first order mode) no significant change in the steering performance is detected with respect to the ideal case (TMSR = ∞). For a TMSR of 10 dB the total tuning range is

reduced by 20 %, and for a TMSR value of 6 dB, the steering efficiency reduced by 50 %.

Figure 4-8b shows the FWHM for different TMSR values. Reduction of the TMSR causes a perturbation of the FWHM, and the electrically unperturbed field condition (0 V applied) does not exhibit maximum FWHM anymore. Maximum FWHM can be re-established by applying voltage to the left electrode. The choice of the left electrode is connected to the input phase relation between the fundamental and first-higher order mode whereas the beam shrinkage is caused by the interference between the output fundamental mode and the first-higher order mode. The FWHM variation with respect to the maximum value is 5 % and 27 % for a TMSR of ∞ and 6 dB respectively. The impact of difference phase relationships between the zero- and the first-higher order mode has been also studied. A phase difference of 90°, 180° and 270° has been introduced between the two input modes for a TMSR of 6 dB. When a phase of 180° is introduced between the two input modes, the total steering and FWHM change are preserved. However, the energy profile of the output field spreads with a FWHM of up to 9.6 μm for the quadrature input phase difference of 90° and 270°, and two energy lobes become visible. The lobes of the first order mode are not in phase with the zero-order mode during the quadrature phase condition and destructive interference in one side of the waveguide is compromised, resulting in the observed FWHM increase.

The presence of the first-higher order mode in the input field degrades the steering performances and integration of higher order mode filters [83] may be required to optimize the input modal content. MMI mode filters with a suppression ratio of 18 dB [84] have been demonstrated, representing a solution to achieve beam steering operation in the highest TMSR region.

4.3 Generic foundry enabled voltage driven steering

A proof of concept PIC is designed, produced and analysed. This is considered to be equivalent to the *low isolation* design presented in section IV. The PIC has been designed and fabricated has been performed through the Smart Photonics MPW foundry service [85].

The beam steering PIC

The circuit was integrated with an on-chip laser. The foundry design kit rules recommended a minimum electrode separation gap of 7.5 μm. Each electrode overlaps the waveguide by 3.5 μm. This is expected to be sufficiently large to contact the p++ layers and minimizes potential asymmetry from mask overlay

tolerances. A waveguide width of 14.5 µm and an electrode length of 500 µm is used.

A microscope photograph of the fabricated PIC is shown in Figure 4-9a. The right dashed box in the full PIC photograph highlights the steering section with the two p-electrodes. A close-up of the steering section is shown in the upper photograph. The left dashed box includes the co-integrated, single-frequency tunable laser source which uses a previously reported coupled cavity concept [86]. The PIC schematic is presented in Figure 4-9b. The red and the blue waveguides represent the laser section and the steering device, respectively. Three MMI couplers are used in the laser to provide internal feedback and coupling to the output waveguides. The second output provided by the laser is not used in this work. The grey areas are deep etched 200 nm below the guiding layer. An s-bend with a minimum radius of curvature of 147 µm and waveguide width of 2.25 µm connects the laser output with the taper input. The s-bend I/O ports have an x- and y-offset of 115 µm and 15.25 µm. The linear 800 µm long taper with a 0.5 degree half angle matches the laser output waveguide width to the steering section. The p-electrodes of the steering section are connected to pad 1 and pad 2 for wire-bonding to a neighbouring printed circuit board for electrical control.

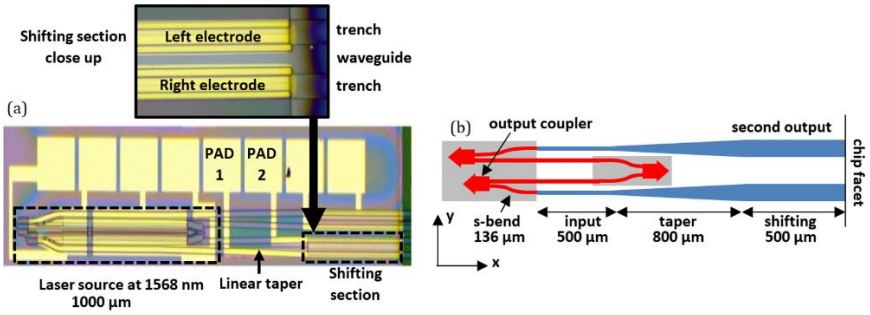

Figure 4-9. a) Microscope photograph of the fabricated PIC. Above the PIC picture is a close-up of the steering device. b) Schematic layout of the PIC.

The near field imaging measurement setup

Beam steering is quantified by means of the measurement setup shown in Figure 4-10. A current source drives the two gain sections of the laser with a current of 50 mA and 48 mA to enable laser oscillation at the wavelength of 1568 nm, with a side mode suppression ratio of 38 dB. The TE zero-order mode is expected to be generated by the laser. The near field at the chip facet is imaged with a 100 X objective, with a numerical aperture of 0.9, to a Xenics infra-red camera at a distance of 140 cm from the chip facet. Magnification calibration has been

performed by imaging the output of two 2 μm wide integrated waveguides placed at a distance of 50 μm. A magnification of 575 is achieved. The effective focal length (e.f.f. in Figure 4-10) of the imaging objective is 2.4 mm at the operated wavelength. An effective image distance of 137.6 cm has been estimated, together with an object distance of 4.2 μm from the front focal point. The camera provides an image of 320 x 256 pixels, with a pixel pitch of 30 μm in the horizontal and the vertical directions. A calibrated intensity scale is used for the data recorded by the camera. A 20 dB optical attenuator is placed between the beam splitter cube and the camera to avoid pixel saturation. A 50:50 beam splitter cube is additionally placed in-line to monitor beam stability. The 50 % power reflected by the beam splitter cube is collected into a flat cleaved facet single mode fiber by means of a 40 X objective. The optical power collected into the optical fiber is then split with a 3 dB splitter to simultaneously monitor the optical spectrum and integrated power. The imaged optical beam has been moved across the camera sensor, by tuning the 100 X objective position with respect to the optical axis, in order to confirm the absence of significant reflections within the optical path.

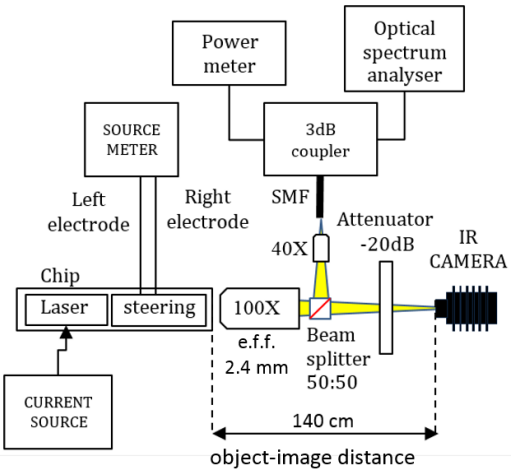

Figure 4-10. Measurement setup.

4.3.1 Sub-micron beam steering

The voltage applied to the *right* electrode (Figure 4-1) is swept from 0 V to -4 V and back to 0 V with a step of 0.1 V while the voltage applied to *left* electrode is initially fixed at 0 V. The range is limited by the inter-electrode leakage current. The same procedure is repeated for the *left* electrode with the *right* electrode set to 0 V. The near field, the optical spectrum and the integrated optical power are measured

for each voltage step. One line of pixels is recorded at the peak intensity point of the near field profile. The leakage current path between the two p-electrodes leads to a current of 40 mA at -4 V and can be defined by a resistance value of 100 Ω. The observed resistance path is 7 times higher than expected, this is attributed to the tolerance in the realized p-doping concentration profile. A dark current of 15.4 μA is observed at a reverse bias voltage of 1 V.

Figure 4-11a shows the lateral optical beam profile acquired from the camera for three conditions: 1) the output waveguide in the steering section is not perturbed (red curve), 2) -4 V is applied to the right electrode and 0 V is applied to the left electrode (blue curve), and 3) -4 V is applied to the left electrode and 0 V is applied to the right electrode (green curve). The vertical beam profile, assumed single mode, is constant and symmetric during the voltage tuning. The lateral intensity curves are normalized to their peak value for comparison, but the total integrated power varies by less than 7 % over the measurement range.

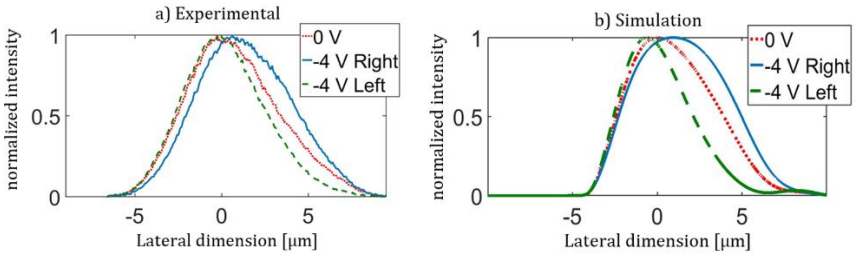

Figure 4-11. a) Measured and b) Simulated optical intensity profiles. Red, unperturbed beam; Blue, -4 V is applied to right electrode; Green, -4 V is applied to the left electrode.

The beam moves to the right (left) side of the waveguide as the negative bias voltage increases for the right (left) electrode. The FWHM is 6 μm for the unperturbed optical beam and a maximum reduction of 1.4 μm is observed when voltage is applied.

In Figure 4-12 a colormap of the beam intensity shows the behaviour of the optical beam over the complete set of applied voltages. The upper and lower halves of the graph refer to the excitation of the *right* electrode and *left* electrode, respectively. The black dashed line represents the positions of the maximum intensity. The beam profile intensity is normalized with respect to the maximum value and expressed in dB. The colormap shows that the beam moves continuously as the voltage is tuned. The steering gradient is 0.20 (0.05) μm/V for the right (left) electrode corresponding to predicted levels of TMSR of 6 (3) dB (Figure 4-7a), assuming that the rate of steering is limited by spatial higher order mode content in the input field. A maximum beam steering of 0.8 μm is achieved when the right

electrode is biased with -4 V, which is attributed to an estimated refractive index modulation of 4×10^{-4}.

The asymmetric steering, the beam asymmetry for the 0 V condition and the FWHM reduction, indicate the presence of higher order mode in the input field with a TMSR of order 3-6 dB. The simulated intensity profile of the steered beam is shown in Figure 4-11b for comparison, for a maximum applied voltage of -4 V and TMSR of 6 dB. Higher order mode excitation is attributed to the presence of the s-bend connecting the output laser and the taper. Optical power coupled to the TE first-higher order mode, with a TMSR of 12 dB, is observed through the optical simulation of the s-bend. A further TMSR contribution is attributed to a ± 200 nm tolerance in the fabricated waveguide width which could affect the imaging properties of the laser output coupler. Not significant optical power is coupled to TM modes during the propagation through the s-bend. The theoretical analysis performed in section IV would therefore indicate that symmetric and higher-efficiency voltage-driven beam steering would be feasible with improved electrical isolation and an improved input optical mode quality. The possibility of achieving an extended and symmetric beam steering through an improved input mode quality is investigated in next section.

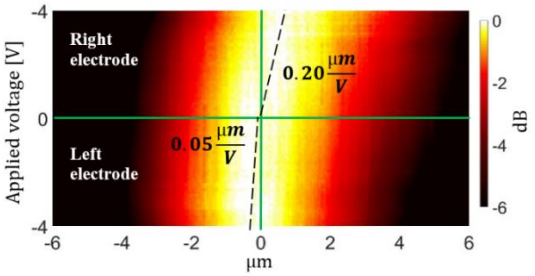

Figure 4-12. Beam profile colormap for different applied voltages.

4.3.2 Enhanced beam steering through a controlled input condition

Beam steering through an improved quality of the input field is studied to validate the impact of the first-higher order mode on the beam steering efficiency. The input waveguide of the beam steering device enables propagation of the zero- and first-higher order mode, however, the power content in the first-higher order mode can be reduced by designing a photonic circuit with components which promote the propagation of symmetrical modes. This can be achieved by employing straight waveguides and MMI mode filters before the beam steering device. A schematic of the designed PIC is shown in Figure 4-13.

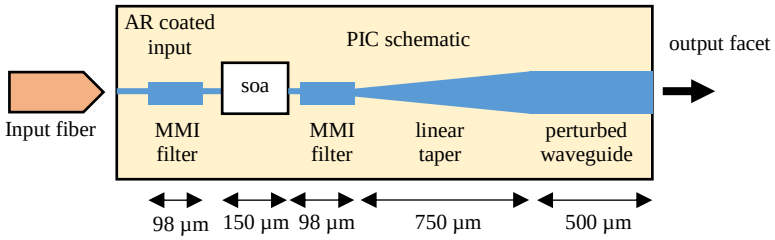

Figure 4-13, Schematic of the PIC with edge coupled input waveguide for the beam steering device.

Two MMI mode filters 98 µm long are inserted along the photonic circuit, the SOA 150 µm long is employed for alignment purpose, the linear 750 µm long taper and the perturbed waveguide represent the beam steering device. The perturbed waveguide is 500 µm long and 14.5 µm to provide comparison with previous experiments. An input lensed fiber couples the light of an external laser (not shown in Figure 4-13) into the chip. A polarization controller is inserted between the laser and the input fiber. It is assumed that the quality of the field at the input of the beam steering device can be optimized by achieving a symmetrical profile of the output field intensity. This is motivated by the fact that the taper and the perturbed waveguide are symmetrical components and are not expected to cause asymmetrical mode excitation. Symmetry of the output field intensity is obtained by tuning the position of the input fiber to optimize the chip output optical power. The best symmetry condition has been achieved for a TM polarization and an optical wavelength of 1465 nm. The unusual wavelength for the optimal PIC operation is suspected to be due to an over-etch of the mode filter trenches. Imperfect higher order mode filtering was observed by other designers on the same MPW run. The same beam steering measurement explained in previous section is performed. Beam steering results are shown in Figure 4-14a, in terms of near field intensity profiles.

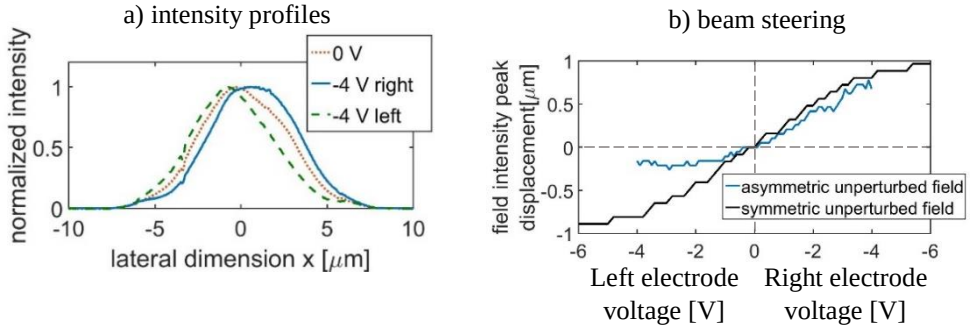

Figure 4-14. a) Recorded intensity profiles and b) beam steering curve.

Figure 4-14a shows the recorded magnified field intensity at the output of the steering device for three conditions: 0 V is applied to both the electrodes (dotted red curve), -4 V is applied to the right electrode (solid blue curve), -4 V is applied to the left electrode (dashed green curve). When negative voltage is applied to the left/right electrode, 0 V is applied to the right/left electrode. A higher level of symmetry has been achieved for the unperturbed beam in Figure 4-14a with respect to the device presented in previous section. This can be translated in a lower excitation of the asymmetric first-higher order mode at the input of the beam steering device, according to the study performed in 4.2.3. The steered beam exhibits comparable degree of displacement for both the right and left electrode case. The benefit that a symmetrical input condition has on the beam steering is quantified by comparing steering performance between the device demonstrated in previous section and the device with improved input modal purity. Beam steering has been calculated for the tested devices by fitting the recorded intensity profiles with polynomial functions of order 18, and by detecting the maximum position of the obtained curves. Fitting has been performed to remove possible errors in the detection of the maximum position of the intensity profiles, attributed to residual particles on the protection screen of the image sensor. The obtained beam steering curves are show in Figure 4-14. The blue curve is related to the beam steering device with asymmetric unperturbed field (described in 4.3), whereas the black curve is related to the device with improved symmetry condition and symmetric unperturbed field. The steering curve for the symmetric unperturbed case shows improved symmetry and steering range with respect to the device with asymmetric unperturbed field. A total tuning range of the order of 2 μm, twice the range for the asymmetrical case, is detected for the device with improved input condition with a maximum applied voltage of -6 V.

4.4 Design of an energy efficient 1x2 voltage driven switch

Integrated optical space switches routing the signal through the optical network should provide broadband and polarization insensitive characteristics to handle high data capacity [87], [88]. Several switching techniques based on semiconductors have been proposed and demonstrated, and a comprehensive review is reported in [89]–[91]. Gate arrays enable optical switching through electronic control on each individual path of a switch network. Path activation/deactivation can be provided through suppression of the split signal by means of electro-optic absorption, at the expense of poor power efficiency [92]. Optical routing through electro-optic phase modulation enables splitting losses reduction. Techniques from digital optical switches, MMI switches, directional couplers to Mach-Zehnder interferometers are here reported [93]. Digital optical switches exploit current injection through a branched optical waveguide to control the mode evolution and to switch output port. A low branching angle guarantees good cross talk and low insertion loss, however it leads a challenging device fabrication [94]. Cross talk of the order of 20 dB with an operational current of 6 mA has been demonstrated [95]. MMI switches can be electronically reconfigured by current injection to digitally steer the optical image of the input field to different output ports. A compact 1x2 switch based on current induced suppression of modal interference exhibited an extinction ratio of 16 dB with switching currents of up to 30 mA [60]. Directional couplers offer switching functionalities by electrically controlling the mode evolution through two optically coupled waveguides. Lateral directional couplers enable the electrical separation of the control electrodes at cost of a larger design footprint and switching voltage [96]. The input light in Mach-Zehnder interferometers (MZIs) is divided in two electrically and optically separated waveguides which are phase modulated to achieve constructive or destructive output recombination. Splitting and combining are implemented by MMI couplers whereas the phase can be modulated by reverse bias voltage. A voltage driven and polarization independent MZI switch has been demonstrated with an extinction ratio of 15 dB and switching voltage of 4.5 V [97]. The width and etch depth deviation of the fabricated waveguide, and the loss imbalance between the arms may significantly affect the extinction ratio depth.

The proposed voltage driven beam steering is interesting to achieve optical switching in MMI couplers, commonly controlled through current injection, while keeping a low level of electrical power consumption. Furthermore, the proposed two-mode interference mechanism has potential to achieve switching in a single waveguide, without an optical power splitting component which might be source of imbalance-limited extinction ratio.

In this section we propose the design of a 1x2 InP/InGaAsP electro-optical switch based on the introduced voltage driven beam steering. Electro-optic characteristics in InP can be tuned by changing the device orientation with respect to the crystal axes [98], opening an alternate route to high speed and polarization insensitive switching. The numerical prediction of the device performance is reported in terms of extinction ratio and excess losses in the C band and for both the polarizations. A fabrication tolerance analysis is shown before the conclusions.

4.4.1 Schematic of the voltage driven optical switch

The schematic 3D view of the optical switch device is shown in Figure 4-15. Same layer stack as for the presented *high-isolation* beam steering device (section 4.2) is assumed in this work.

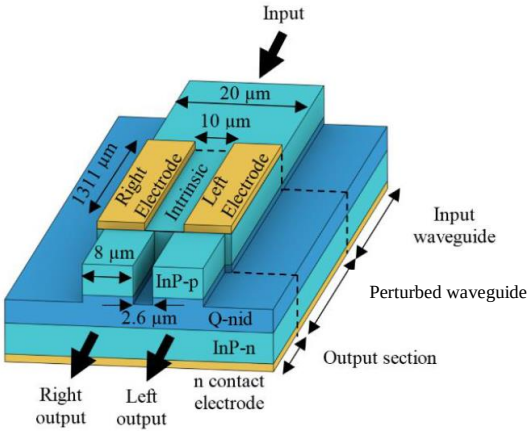

Figure 4-15. 3D schematic view of the optical switch.

A 20 µm wide perturbed waveguide is chosen to achieve sufficient beam steering to comply with the output ports gap of 2.6 µm. Such a large perturbed waveguide also enables significant size reduction of the steered beam, and the possibility to connect two 8 µm wide output ports at the output section, with sufficient mode size matching. The output waveguides marked as *left* and *right output* are symmetrically connected at the output cross section of the perturbed waveguide. The fundamental mode of a 20 µm wide waveguide is employed to define the input field condition. It is assumed that adiabatic tapering is possible to mode match the fundamental modes of the input/output ports with the mode of a standard 2 µm InP waveguide.

4.4.2 Optical switch performance

Simulations are performed to understand how beam steering can address different output ports and the impact that an asymmetrical steered beam has on mode-matching with butt-coupled integrated waveguides. The intensity distribution of the field propagating through the device is monitored to show the switching mechanism. Figure 4-16 shows the energy density profile through the device when the left electrode is biased with -12 V while keeping the right electrode at 0 V. The solid white lines represent the waveguide edges whereas the dashed lines indicate the electrode positions. The input field is the TE zero-order mode of the input waveguide. The energy density profile is normalized with respect to the maximum value of the input field energy density. The beating in the intensity distribution in the left output waveguide motivates an analysis of power content in higher order modes. A 3 % of the input power is coupled to higher order modes of the left output waveguide. Higher order modes in the output waveguide can be filtered by tapering down the output waveguide to a single mode operation width. An operational dark current of the order of 1.5 pA is recorded for the two switch states. A symmetrical energy distribution behaviour is observed for the right switch state.

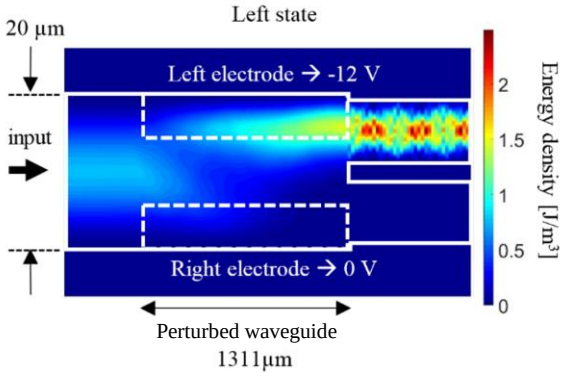

Figure 4-16. Energy density profile for the left state.

Excess losses and extinction ratios are quantified by monitoring the optical power coupled to the zero-order mode of the output waveguides, while sweeping the voltage applied to the electrodes. Excess losses and extinction ratio are expressed in dB in this section in order to provide practical comparison with different techniques demonstrated in the literature. Figure 4-17a shows the output power normalized to the total input power at the two output ports when the voltage applied to the electrodes is swept from 0 V to -12 V. The voltage applied to the left electrode is swept in the left half of the graph, whereas the right electrode voltage is tuned in the right half. The TE and TM polarizations of the input field are identified by the solid

and the dashed curves, respectively. An excess loss of -0.6 dB and -1 dB is predicted for the TE and TM cases at -12 V whereas the extinction ratio is -29 dB and -17 dB. The 3 % and 8 % of the total input power couples to higher order modes of the addressed output waveguide for the TE and TM case. The 1 % and 4 % power couples to the not selected output port for TE and TM polarization. A 6 % of power lost due to electro-absorption and carrier absorption for both the polarizations. The reported polarization dependence of the excess loss and the extinction ratio is mainly attributed to the choice of the device orientation with respect to the crystal axes. For the considered crystal orientation the TM polarization is not affected by Pockels effect, exhibiting a less efficient steering and poorer overlap with the output port.

The wavelength dependence of the electro-optic coefficients and of the modal propagation leads an analysis of the switch performance for different operational wavelengths. The wavelength dependence of the extinction ratio and the excess loss is shown in Figure 4-17b across the C band range. A maximum variation of the excess loss of 0.08 dB and 0.36 dB is predicted for the TE and TM polarizations, the extinction ratio over the analysed wavelength range is larger than 21 dB and 13 dB for the TE and TM cases, respectively.

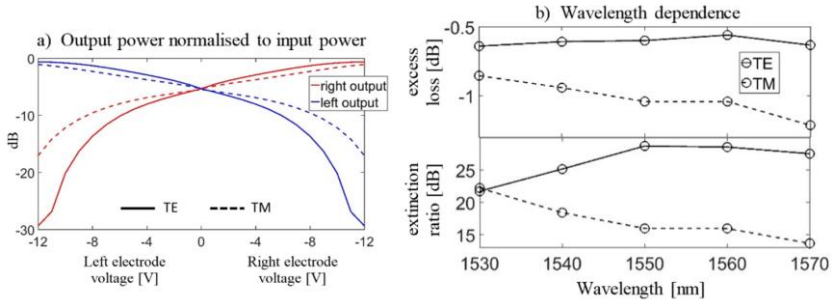

Figure 4-17. a) Optical output power for the two output ports; b) Wavelength dependence of the excess loss and the extinction ratio.

4.4.3 Tolerance analysis

MMI splitters/combiners exploited in MZI switches exploit single mode I/O ports and MMI sections with a width of the order of 2 μm and 10 μm, respectively. Due to the design dimensions, MMI based splitters/combiners are sensitive to sub-micron fabrication tolerances, and the insertion loss can be critically compromised [99]. Simulations of MMI combiners/splitters optimized for MZI switches by P. Maat [98] and W. Yao [100] show how the fabricated linewidth variation impacts the switch excess loss for a device with layer stack comparable to the one used in this work. The MMIs used in [98] and [100] exhibit a width of 16 μm and 13 μm

and simulation results show that a waveguide width variation of ± 200 nm impacts the excess loss with a maximum increment of 1.5 dB and 1.7 dB, respectively.

The proposed switching mechanism is based on a 20 μm wide waveguide and is expected to be more robust with respect to sub-micron fabrication variations. This is motivated by the fact that the relative change of the beating length with respect to the waveguide width is inversely proportional to the waveguide width [83]. The impact on the switch performance due to waveguide width variation, over/under etch of the waveguide trenches and isolation misalignment is studied.

A simplified version of the proposed optical switch is exploited for the tolerance fabrication study. The electro-optic effect is modelled by tuning the refractive index underneath the electrodes in the guiding layer, uniformly across the vertical dimension. A waveguide width variation of ± 200 nm with respect to the designed width is considered, and the extinction ratio and excess loss are recorded while scanning the refractive index. The maximum extinction ratio achieved across the waveguide width variation range and the related excess loss are shown in Figure 4-18.

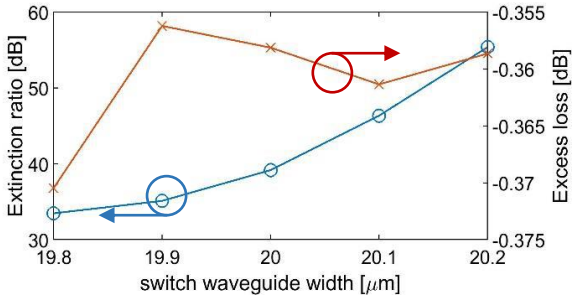

Figure 4-18. Maximum extinction ratio and excess loss for a perturbed waveguide width variation of ± 200 nm.

The extinction ratio increases for larger waveguide width. A wider waveguide implies improved steering and larger FWHM reduction, and better mode matching with the output port can be achieved. However, a reduction of 6 dB of the extinction ratio occurs for a waveguide width variation of -200 nm. The excess loss is of the order of -0.3 dB and is confined in a range of 0.02 dB. The excess loss is attributed to residual mode mismatch. The etch depth of the waveguide trenches is varied in a ± 20 nm range for a waveguide width of 20 μm. An extinction ratio higher than 37 dB is retained, with a not significant change of the excess loss which is still higher than -0.4 dB. A lateral misalignment range of ± 200 nm is also considered for the isolation region and while a reduction of 5 dB is observed for the extinction ratio, the excess loss is higher than -0.4 dB.

4.5 Conclusions

Voltage-driven optical beam steering in an InP PIC has been demonstrated. Simulations show that an induced electric field and charge-carrier depletion can enable beam steering across the output facet of a single optical waveguide. High electrical isolation is predicted to enable a total beam steering of 4.9 μm with maximum applied voltage of 10 V and with a maximum power consumption of 4.5 pW. A proof of concept experimental device shows a lateral total beam steering of 1 μm with a voltage of 4 V. This has been attributed to a maximum refractive index change of 4×10^{-4}. While a beam steering efficiency of 0.34 μm/V has been numerically predicted, experiments show values of up to 0.2 μm/V which is believed to be limited by higher order mode excitation. A beam steering device with improved input modal quality has been tested to validate the link between the level of symmetry in the unperturbed beam and the steering range. A higher level of symmetry of the unperturbed beam has been achieved together with a wider steering range of 2 μm, with a maximum applied voltage of 6 V.

Digital beam steering has been numerically demonstrated through reverse bias voltage control to enable new concepts for low-power consumption optical switch solutions. Electro-optical switching between the two output ports is possible with an excess loss of the order of 0.6 dB and 1 dB for the TE and TM polarizations, indicating that sufficient beam quality is retained by the steered field. The use of a large waveguide as a beam steering section represents potential to achieve robustness with respect to fabrication tolerances, at cost of larger device footprint.

5 Current driven electro-optical beam steering[3]

5.1 Introduction

Current injection is employed in this chapter to explore the steering range limits achievable in an optical waveguide through the proposed two-mode interference mechanism. The possibility of reconfiguring the refractive index profile of an optical waveguide through current injection is interesting to achieve a large refractive index modulation with respect to reverse bias voltage control [101]. The impact that a large refractive index perturbation has on the design of the beam steering device is studied.

Current injection has been employed in [60] to achieve a digital form of beam steering. Beam steering has been demonstrated between two output ports in [60], however the possibility of achieving continuous tuning between the two switch states has not been explored. Studying the possibility of a wide steering range with continuous tuning control is interesting to enable novel assembly methods based on optical control. The study of novel alignment solutions is relevant for the photonic packaging industry, for which fiber to chip alignment is one of the most critical and expensive operations [12]. Alignment between an optical fiber and a photonic chip in a package may be compromised by factors such as thermal expansion [102], shrinkage of the fixation glue [103], and continuous in plane dynamic control of the on chip beam position represents a revolutionary alignment solution with potential to relax assembly tolerances and requirements on the package.

The steering performance of the current injection beam steering device is studied in terms of near field measurements. A fiber-to-chip coupling experiment is performed to understand how degradation of coupling efficiency due to misalignment losses can be electro-optically compensated through beam steering.

5.2 Current injection beam steering device

A schematic 3D view of the proposed current driven beam steering device is shown in Figure 5-1. The device is based on the same geometrical structure of the voltage driven device. The input field is laterally expanded through the 1200 μm long adiabatic linear taper to match the mode size of the perturbed waveguide. The

[3] The fabrication and measurement employed for the writing of this chapter have been performed by Simone Cardarelli.

taper length is 550 μm longer than previous designs in order to suppress the risk of high order mode excitation which may complicate the beam steering investigation and compromise the total tuning range. The perturbed waveguide is 280 μm, as long as the electrodes. The electrode length is the main difference between the design for the current and the voltage driven devices. Voltage driven beam steering has been demonstrated with an electrode length of 500 μm, related to the unperturbed beating length of the waveguide. However, as predicted by the analytical model in chapter 2, the beating length exhibits a significant reduction for high refractive index change and leads an electrode-length re-adjustment to achieve optimal beam steering. For the current driven electrode design, the injected current is expected to flow through half the waveguide due to the symmetry of the control electrodes, and the perturbed beating length is expected to tend to half the unperturbed value. This explains the re-design of the electrode length.

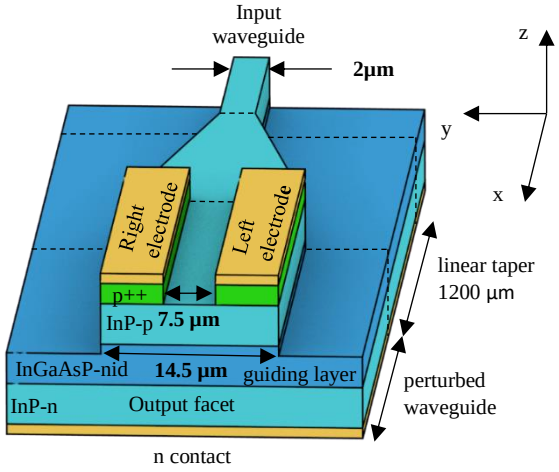

Figure 5-1. Schematic 3D view of the beam steering device.

The principle of operation is similar to the voltage driven case. The control right and left electrode are alternatively biased with positive voltage with respect to the n electrode in order to inject direct current through one side of the guiding layer. When positive voltage is applied to one of the two electrodes, the second electrode can be either set as an open connection or set to 0 V. Since forward biasing of the p-i-n waveguide enables filling of free carriers in the guiding layer, a negative refractive index change is expected to occur in the current injected region. As a consequence, beam steering is achieved towards the opposite direction with respect to the biased electrode.

The fabricated PIC

A proof of concept PIC has been internally fabricated (fabrication details reported in Appendix 10). Active and passive sections have been integrated in the custom fabrication process flow. A microscope photograph of the fabricated PIC is shown in Figure 5-2a. The input waveguide of the PIC is angled at 7° to suppress Fabry-Perot resonances in the PIC. The input waveguide is 3.5 µm wide and is tapered down to a width of 2 µm through a 150 µm long linear taper. A curved waveguide with radius of curvature of 800 µm connects the angled input to the 4870 µm long straight waveguide. An SOA 150 µm long is inserted through the optical path before the beam steering device. The linear taper is shown in the right side of the PIC photograph whereas a close-up of the beam steering device is shown in Figure 5-2b. The electrodes of the PIC are wire-bonded to a neighbouring printed circuit board for electrical control. Both the input and the chip output facets are defined through scribe and break procedure.

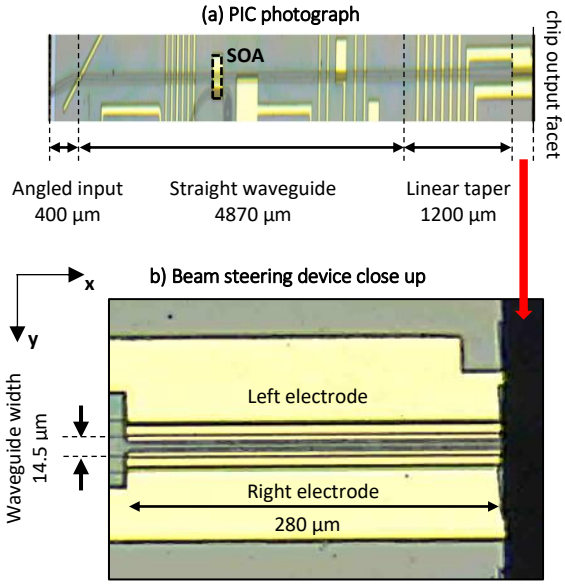

Figure 5-2. Microscope photograph of the fabricated PIC and b) close-up of the beam steering device.

The near field measurement setup

The impact that current injection has on the optical beam position, power and shape is characterized through the measurement setup shown in Figure 5-3. The on chip SOA (Figure 5-2a) is operated in transparency and driven with a current of 3.17 mA, set by the current source. The tunable commercial laser is operated at a

wavelength of 1550 nm. An attenuator and a polarization controller are inserted between the laser and the input fiber. The input fiber is ended with a spherical lens with radius of 7.5 μm to achieve sufficient input mode matching and is aligned with an angle of 23° with respect to the chip facet normal. An optical power of -3.3 dBm is guided by the input fiber. The p-electrodes are biased by the power supply. The intensity profile of the optical electric field at the output facet has been magnified and recorded through the near field imaging setup shown in Figure 5-3.

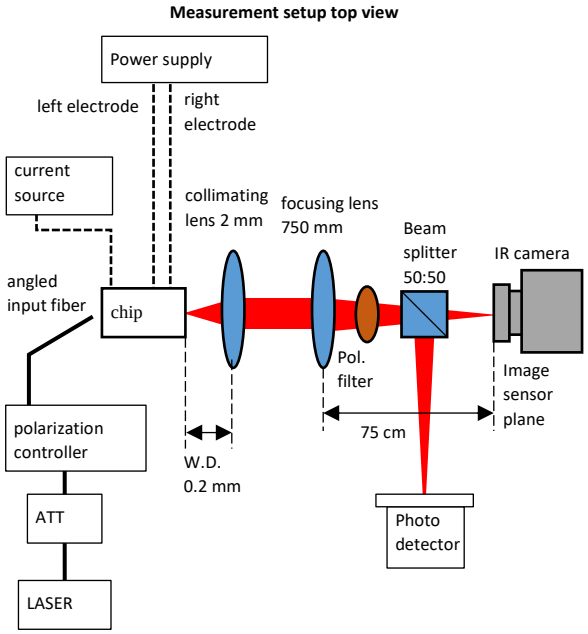

Figure 5-3. Near field measurement setup.

The near field imaging setup has been modified, with respect to the voltage driven measurements, to comply also with the far field measurements reported in chapter 6. Two anti-reflection (AR) coated lenses of focal length 2 mm and 750 mm magnify the optical near field. The collimating lens has a numerical aperture of 0.5 and a working distance of 0.2 mm. The focusing 750 mm focal lens is 11 cm far from the collimating lens. The magnified field is recorded at a distance of 75 cm from the focusing lens, by an infrared camera. A magnification of 375 is achieved. A 50:50 beam splitter cube is additionally placed in-line to monitor the beam optical power. The 50 % power reflected by the beam splitter cube is collected into a photo detector. A polarization filter, used to define the optical field polarization, is inserted at 15 cm from the collimating lens.

The electrical characterization of the device is performed to link beam steering and electrical current. The electrical behaviour of the beam steering device is characterized by measuring the resistance between the p-electrodes and the IV curves of the left (right) electrode when setting the right (left) electrode as open circuit. A resistance path of 75 Ω is measured between the p-electrodes. The IV curves of the independently tested electrodes are characterized by an activation voltage of 1 V and a gradient of 13 Ω and 19 Ω for higher voltage values, for the right and left electrode respectively. The difference in gradient is attributed to a misalignment of the mask defining the p++ contacts (see Figure 5-1), observed through optical microscope. The observed misalignment is expected to be limited in a ± 0.5 μm range. Beam steering is performed through the following electrical configuration: the voltage applied to the *right* electrode (Figure 5-1) is swept from 0 V to 3 V and back to 0 V with a step of 0.1 V while the voltage applied to the *left* electrode is initially fixed at 0 V. The same procedure is repeated for the *left* electrode with the *right* electrode set to 0 V. A maximum current of 143 mA and 100 mA is injected through the right and left electrode at the maximum applied voltage of 3 V. The near field intensity profile and the integrated optical power are measured for each voltage step. One line of pixels is recorded at the peak intensity point of the near field profile.

5.2.1 Enhanced optical beam steering

Figure 5-4 shows the lateral optical beam profile acquired from the camera for three conditions: 1) the output waveguide in the perturbed section is not perturbed (red curve), 2) 100 mA (2.4 V) is applied to the right electrode and (blue curve), and 3) 100 mA (3 V) is applied to the left electrode (green curve). The same current injection is considered for both the right and left electrodes in order to compare beam steering results induced by a similar level of carrier injection. The vertical beam profile, assumed single mode, is constant and symmetric during the current tuning.

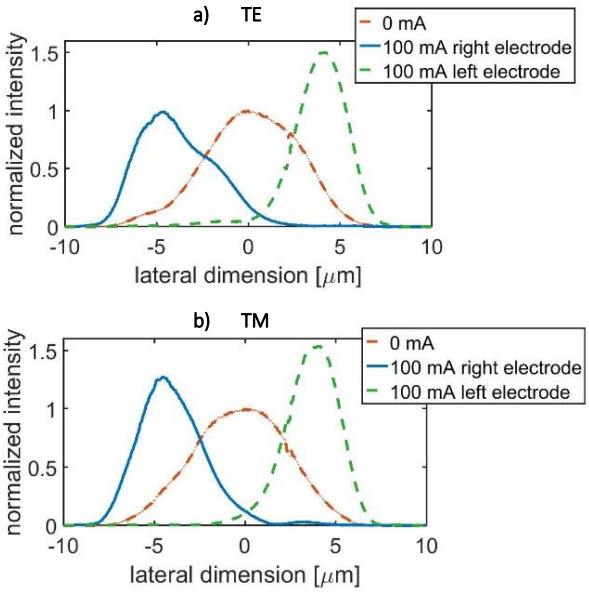

Figure 5-4. Measured a) TE and b) TM optical intensity profile. Red, unperturbed beam; Blue, 100 mA is injected through the right electrode; Green, 100 mA is injected through the left electrode.

The beam moves to the right (left) side of the waveguide as the voltage increases for the left (right) electrode. The field displacement occurs toward the opposite side with respect to the tuned electrode, due to the negative sign of the refractive index change induced by carrier injection. A total peak displacement of 8.8 μm and 8.5 μm is recorded for the TE and TM cases. The full width half maximum (FWHM) of the TE and TM unperturbed fields is of the order of 6.4 μm. A reduced FWHM of up to 3.2 μm and 3.4 μm is observed for the left and right electrode operation. In Figure 5-5 a colormap of the beam intensity shows the behavior of the optical beam over the complete set of injected currents. The upper and lower halves of the graph refer to the excitation of the *right* electrode and *left* electrode, respectively. The left and the right y axis are related to the injected current and applied voltage, respectively. The beam profiles intensity are normalized with respect to the maximum value of the unperturbed field and expressed in dB. The colormap shows that the beam moves continuously as the current is tuned. The beam displacement starts at the activation voltage, for which significant carrier injection is expected to occur in the guiding layer. The beam steering exhibits saturation for high current values, and reaches range on the order of 8.5 μm. The beam steering saturation is attributed to the displacement limitation represented by the confinement waveguide trenches. A 22 % difference in maximum tuning range is detected between the experimental and

the analytical results. The difference may be attributed in part to the different lateral confinement conditions, weakly confined for the fabricated shallow etched waveguide and perfectly confined in the idealized case, and in part to the two-mode approximation. The observed peak total displacement has a maximum variation of the order of 0.4 dB in the wavelength range from 1530 nm to 1560 nm, for both the polarizations. A maximum excess loss of 1.2 dB and 0.9 dB, attributed to free carrier absorption, is observed for the TE and TM polarizations in the C band during current injection.

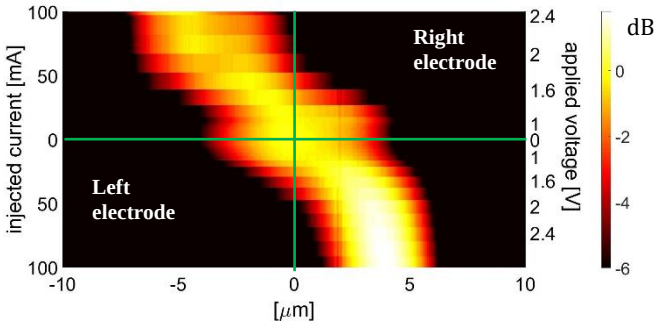

Figure 5-5. Beam profile colormap for different injected currents.

5.2.2 Chip-to-fiber misalignment compensation

The potential of the proposed device for micro-optical alignment is studied in this section. The link between the measured steering range and the capability of compensating misalignment losses in a butt-coupling condition with subsequent optical modules is studied through a chip-to-fiber coupling experiment. The fiber-chip coupling experimental setup is shown in Figure 5-6.

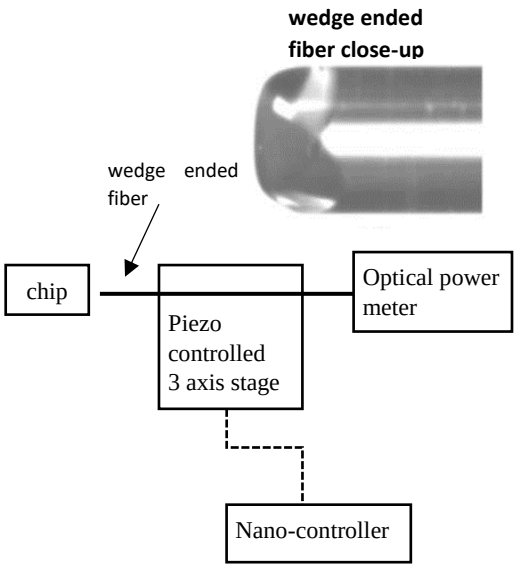

Figure 5-6. Fiber-chip coupling measurement setup.

The optical excitation and the electrical connection to the chip is not shown since it is unchanged with respect to the measurement setup in Figure 5-3. The near field imaging optics is replaced with an optical fiber manipulated through a nano-controlled piezo axis stage. The optical fiber is single mode at the operated wavelength, and wedge ended in order to match the elliptical shape of the on chip optical beam. The far field of the radiated by the optical fiber exhibits a full angle divergence of 10.3° and 31.7° in the horizontal and vertical direction, measured where the beam intensity drops by the factor $1/e^2$. The 3 axis stage is controlled in the lateral direction with a resolution step of 400 nm. The fiber is connected to the optical power meter to monitor the coupling efficiency. The optical fiber is aligned to the chip waveguide to optimize the optical power coupling. The fiber is placed at a working distance of the order of 16 μm ± 2 μm from the chip facet.

The optical fiber is shifted in front of the integrated waveguide and for each fiber-chip misalignment, the coupled optical power is recorded. The coupled power is recorded in two cases: 1) the on chip beam is steered through current injection to optimize the coupled optical power and 2) in absence of electro-optical control. The results of the misalignment losses with and without electro-optical compensation are shown in Figure 5-7.

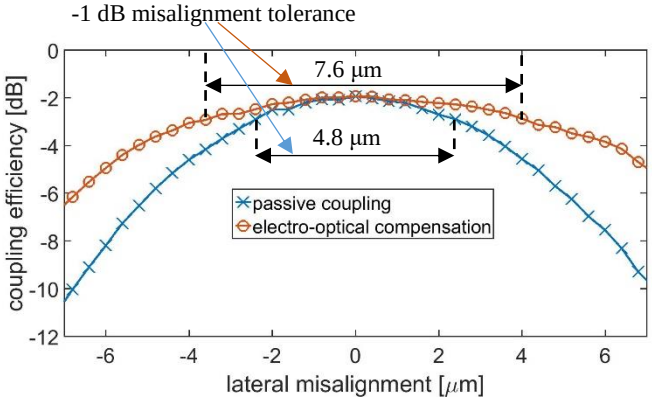

Figure 5-7. Coupling efficiency for passive and compensated alignment.

A maximum coupling efficiency of -1.9 dB is attributed to a mode mismatch between the InP waveguide and the optical fiber. A -1 dB misalignment tolerance of 4.8 µm is measured for the passive coupling case. The -1 dB misalignment tolerance is enhanced up to 7.6 µm if the beam steering is activated. A power compensation of 1.2 dB and 1.7 dB is achieved at the left and right limits of the -1 dB misalignment tolerance region. Loss compensation in the improved -1 dB misalignment tolerance region has been performed with a maximum current of 60 mA, for which a maximum optical loss of the order 0.7 dB has been measured in previous section. Optical loss by free-carrier absorption is expected to limit further loss compensation in the -3.6 µm to 4 µm misalignment range. A minimum misalignment loss compensation of 3 dB is achieved for a misalignment of ± 6 µm.

5.3 Conclusions

Near field measurements have shown that the current driven optical beam steering device enables displacement of the intensity field peak in a range of 8.8 µm and 8.5 µm for the TE and TM polarization, with a maximum current of 100 mA. Steering saturation is observed at the edges of the tuning range. Optical losses of 1.2 dB and 0.9 dB are observed for the TE and TM polarizations at a current of 100 mA.

A wedge ended optical fiber has been artificially misaligned with the beam steering waveguide and tracked by the steered beam to show electro-optical compensation of the misalignment losses. Misalignment loss compensation through beam steering has shown an improvement of the -1 dB misalignment tolerance of 60 %, from 4.8 µm to 7.6 µm. Full misalignment loss compensation in the improved -1 dB misalignment tolerance range is expected to be compromised by the observed

free-carrier absorption. Results indicate that electro-optical beam steering has potential to relax alignment tolerances during micro-optical alignment of I/O chip-fiber connections and may also enable new concepts for on chip vertical beam alignment.

On-chip optical coupling of the proposed device with integrated waveguides has been studied in chapter 4 through the investigation of a 1 x 2 optical switch, whereas off-chip edge coupling with an optical fiber has been treated in this chapter. The possibility of exploiting the proposed beam steering device also in the far-field region is interesting for free-space functionalities and will be discussed in chapter 6.

6 Far field beam steering[4]

6.1 Introduction

The possibility of achieving enhanced free space beam steering functionalities is considered by combining the beam steering device with a curved integrated facet. Integrated curved facets have been employed by researches to demonstrate integrated collimation solutions [104] or to enable high power lasers [105]. However, the possibility of using curved facets as passive methods to redirect beams steered across the facet of a chip has not been explored. Reconfiguration of the radiation pattern of an optical emitter is an interesting capability for a number of applications such as LIDAR [9], free-space communication [49] and localization [106].

The curved facet beam steering device is studied numerically and compared with the beam steering device with flat facet. Experimental far field reconfiguration for a curved and flat facet terminated device is analysed, for both voltage and current tuned steering. A localization experiment has been performed to understand how the proposed far field steering method behaves in a real free space indoor communication scenario.

6.2 Enhanced far field beam steering through a curved output facet

6.2.1 Curved facet functionality

The proposed concept for far field reconfiguration, by exploiting a curved geometry as output facet of the beam steering device is here explained. The proposed device and far field steering mechanism are shown in Figure 6-1a and Figure 6-1b, respectively. The device presents the same basic structure with respect to the device presented in chapter 4 and 5, except for the curved output facet. Different electrode lengths will be considered in section 6.3 of this chapter to study both voltage and current control. The curved facet is implemented by a cylindrical lens. The far field reconfiguration mechanism is based on the fact that steered beams propagating through the cylindrical lens at different distances from the lens optical

[4] The fabrication of the voltage driven steering device demonstrated in this chapter has been performed by SMART Photonics. The fabrication of the current injected beam steering device has been performed by Simone Cardarelli. The FIB processing for the fabrication of the curved facets has been performed by Simone Cardarelli and Sebastian Koelling. The reported measurement and simulation results have been performed by Simone Cardarelli.

axis, experience different semiconductor/air interfaces and are radiated towards different angles in the free space. Figure 6-1b shows the schematic radiation pattern for an unperturbed beam and perturbed beam condition, through the top view of the emitting device. The optical field propagates straight through the device when 0 V is applied to both the electrodes. The beam position across the waveguide output facet is represented by the red ellipse. The output beam propagates through the center of the cylindrical lens and is radiated towards the direction parallel to the device. If the voltage applied to one of the two electrodes is tuned, beam steering occurs across the waveguide facet. The perturbed steered beam position is represented by the black ellipse. In the perturbed condition, the steered beam propagates through a tilted semiconductor/air interface and the radiation lobe is directed towards a different angle with respect to the unperturbed case.

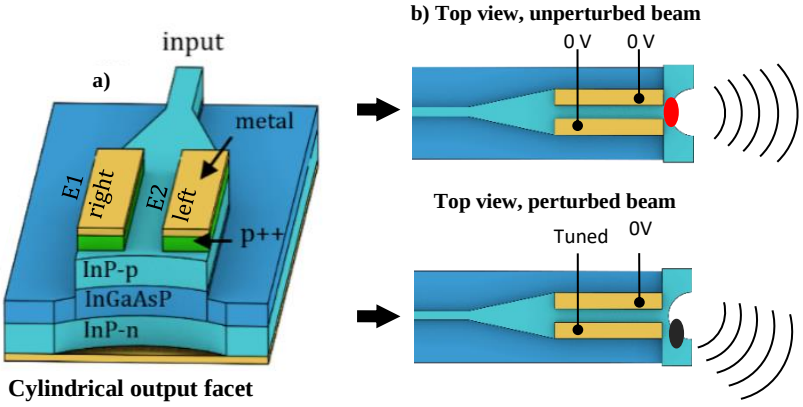

Figure 6-1. a) Schematic of the proposed far field beam steering device combined with a cylindrical lens and b) steering mechanism.

6.2.2 Far field beam steering: simulations

Simulations are performed for the curved and flat facet device in order to numerically validate the concept and to understand how the cylindrical shape affects the optical beam profile and the radiation angle. A voltage driven beam steering device is considered in this section, with a waveguide width of 14.5 µm and an electrode length of 500 µm. A cylindrical facet with a radius of 20 µm is considered. The numerical analysis is performed by adding an extra step to the simulation flow introduced in chapter 4. The output field calculated through FIMMPROP is exported to OMNISIM, a *finite difference time domain* solver, to simulate the optical propagation through the lens. The imported output field is injected through a field launcher at the final stage of the perturbed waveguide and propagates through the

cylindrical facet. A two dimensional analysis of the device is performed through the effective index approximation in the vertical direction. The tuned radiation is shown through the simulated field intensity pattern of Figure 6-2, when 0 V is applied to both the electrodes (Figure 6-2a) and when -10 V is applied to the right electrode (Figure 6-2b).

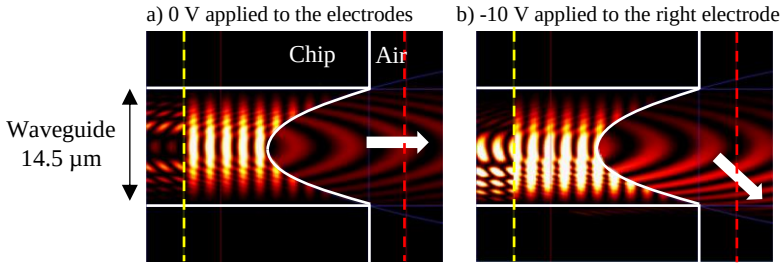

Figure 6-2. Real electric field intensity distribution when a) 0 V is applied to both the electrodes and b) -10 V is applied to one of the two electrodes.

Figure 6-2 represents a top view of the device and the solid white lines define the waveguide edges and the curved facet interface. The two images are vertically compressed. The yellow dashed line represents the field launcher. The red dashed line represents a field monitor and enables recording of the travelling optical field, and the calculation of the far field radiation pattern by Fourier transform. The optical beam is symmetrical when 0 V is applied to the electrodes and is cantered at the angle 0°, that is the direction parallel to the device. A change in the radiation angle is observed for the perturbed case. The arrows represent the direction of the main lobe radiation. The radiation patterns are shown in Figure 6-3 in terms of intensity of the far field.

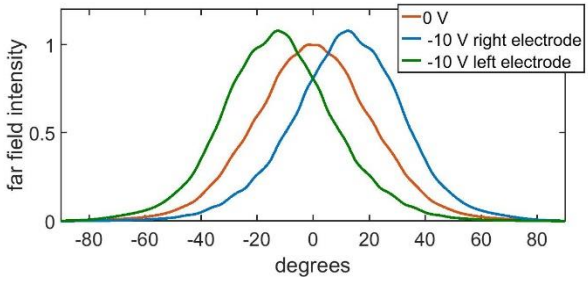

Figure 6-3. Far field intensity profiles.

A symmetrical beam steering is qualitatively observed for both the electrodes. A FWHM of 46° is detected for the unperturbed beam, a factor of 7 larger with respect to the flat facet case. Beam steering is in this section quantified as the

position of the mean energy to provide comparison with the results presented in the experimental section. To calculate the beam steering, the far field intensity profile is multiplied by the radiation angle domain, integrated over the angle and divided by the total field energy. The formula used to quantify the beam steering is

$$Mean\ energy\ displacement\ [\text{degrees}] = \frac{\int I(\vartheta, V) \cdot \vartheta\ d\vartheta}{\int I(\vartheta, V) d\vartheta}$$

Where $I(\vartheta, V)$ is the far fiend intensity profile for different bias condition, V is the applied bias voltage and ϑ is the angular radiation domain and is expressed in degrees. The simulated beam steering achieved with the curved facet is shown for an applied voltage ranging from 0 V to -10 V in Figure 6-4, and the simulation results of a device with flat facet are also reported for comparison.

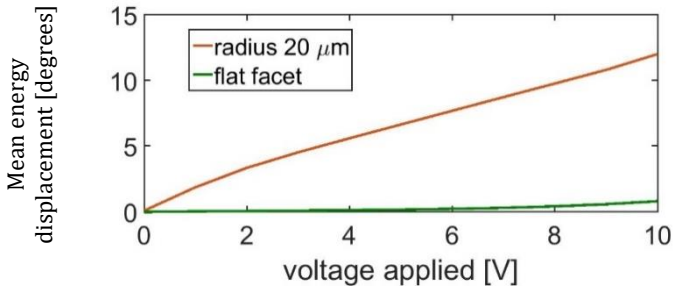

Figure 6-4. Average position of the steered far field radiation

A total tuning range of 12° is achieved for the curved facet case, whereas a steering smaller than 1° is provided by the flat facet. The steering gradient is of the order of 1.2°/V for the curved facet case. The not significant far field beam steering observed in Figure 6-4 in the flat facet case indicates that the phase front of the beam steered across the chip facet is not significantly perturbed. The observed beam steering in the curved facet case indicates that a passive cylindrical lens can enable control of the beam output phase front if combined with the two-mode steering concept.

6.3 Experimental far field beam steering

Both voltage and current driven beam steering have been exploited to validate the enhanced far field beam steering concept. A voltage based beam steering chip has been fabricated through an MPW run offered by SMART Photonics whereas the current injection based chip has been internally fabricated (se Appendix 10 for the

details of the fabrication). The cylindrical facets have been fabricated for both the chips with a post-processing step.

6.3.1 The voltage driven far field reconfiguration

The far field beam steering is here studied for the voltage driven beam steering device. Two PICs are considered from the same cell, one PIC with curved facet and one PIC with flat facet as control experiment. An optical microscope image of the two test PICs containing the steering devices is shown in Figure 6-5a. The steering section is 500 µm and with a waveguide width of 14.5 µm. The linear taper is 750 µm long. Apart from the facets, the two devices are identical. The inputs are on the left side of the chip. A semiconductor optical amplifier (SOA) is placed after the input for alignment purposes with external optical sources. An MMI mode filter is placed before and after the SOA. A 3D view and a top view of the curved facet are shown respectively in Figure 6-5b and Figure 6-5c. The curved facets have been etched by post processing by means of focused single pass ion beam (FIB), with an acceleration voltage of 30 kV, beam current of 2.7 nA and dwell time of 2 ms with 32.4 nm pitch. The curved facet has been etched on top of a cleaved facet. The etching path is an inside-out circular spiral with outer radius of 20 µm.

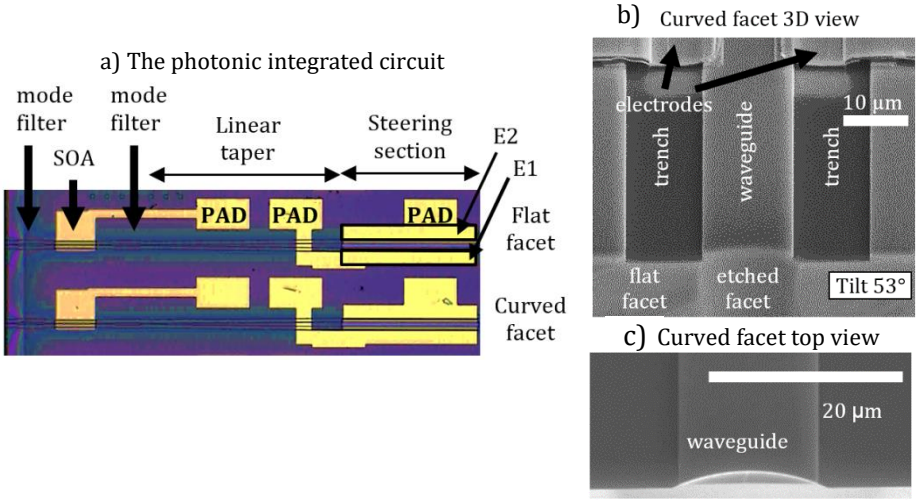

Figure 6-5, a) microscope photograph of the tested PICs. Scanning electron microscope image for b) 3D view and c) top view of the curved facet.

The effect of the on-chip cylindrical facet has been studied by the experimental setup shown in Figure 6-6. First, we compare the two steering devices by near field characterization to show that the beam at the chip facet has comparable movement for both the flat and cylindrical facet devices. The near field

measurement setup is shown in Figure 6-6a. An external laser at 1465 nm and output power of -6 dBm is fed through a polarization controller (to set the TE polarization) into the chip by exploiting a lensed single mode fiber. The SOA is operated near transparency. The optical field at the facet of the chip is collimated by an infrared aspherical lens with focal length of 2 mm and focused by the lens f1 with focal length 750 mm. The 2 mm has a NA of 0.5. A magnification of 375 is achieved for the imaged beam. The image is acquired by a 320 x 256 pixels XENICS IR camera. The scheme of the far field experimental setup is shown in Figure 6-6b. The lens f1 is replaced with the lenses f2 and f3 having a focal length of 150 mm and 250 mm respectively. The lens f2 makes a magnified image of the near field which is collimated by f3. The Fourier plane is created at 250 mm from f3 and acquired from the camera. The imaged far field window represents a 162° x 130° angle domain, however, the 0.5 NA of the objective lens limits the effective field of view to a full angle range of 67°.

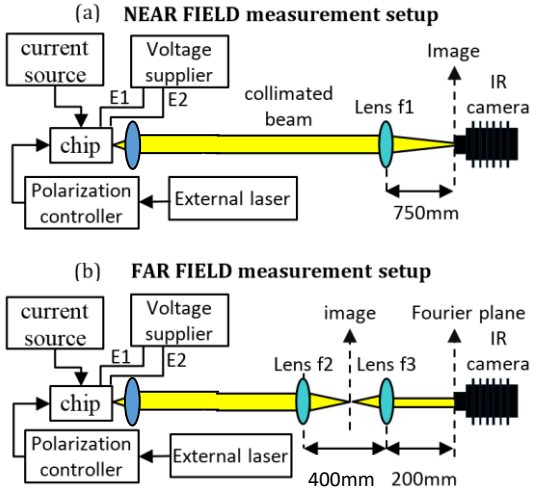

Figure 6-6. a) Near field measurement setup; b) far field measurement setup.

The voltage applied to the electrode E1 (Figure 6-1) is swept from 0 V to -6 V and back to 0 V with a step of 0.2 V, while the voltage applied to the electrode E2 is initially fixed at 0 V. Afterwards, the complementary electrical configuration is applied to E1 and E2 and the voltage sweep is repeated for electrode E2. The electrical current drawn by the device is monitored during the beam steering measurement. A maximum leakage current of 40 mA is recorded and attributed to the top cladding path present in between the p-electrodes. The horizontal section passing through the centre of the recorded far field profiles is shown in Figure 6-7a

for the device with flat output facet and in Figure 6-7b for the device with curved output facet. Profiles are shown for the unperturbed condition (red curve), when -6 V is applied to the right electrode (blue curve) and when -6 V is applied to the left electrode (green curve).

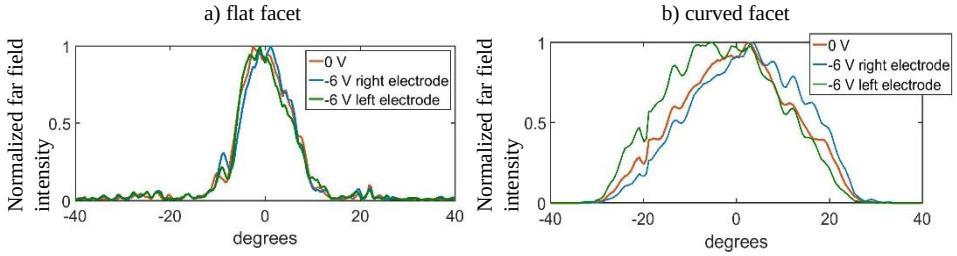

Figure 6-7. Far field intensity profiles for the beam steering device with a) flat output facet and b) curved output facet.

The far field for the flat output facet does not exhibit significant steering, whereas lateral reconfiguration is observed for the curved output facet case. An increase of the FWHM from 13° to 30° is observed between the flat and curved facet case. The FWHM magnification is due to the diverging properties of the etched cylindrical lens. A low level (2.7% of the total energy) of interference pattern is visible in the intensity profiles of both the graphs, which is expected to be attributed to substrate optical leakage. For the far field intensity profiles of both the flat and curved output facet cases, a vertical integration of the recorded beam is applied to reduce the level of the interference pattern and to quantify beam steering through the mean energy displacement calculation.

The beam steering in the near and far field for both the flat and curved facet devices is shown in Figure 6-8. Near field is reported to show that the far field comparison is performed for two devices with similar steering behaviour at the chip facet. Figure 6-8a shows a total beam steering displacement of 0.8 μm and 1.2 μm, for the flat and the 20 μm radius curved facet device, respectively. The far field steering in Figure 6-8b is not significant for the flat facet device whereas it reaches a total tuning range of 5° for the curved facet case.

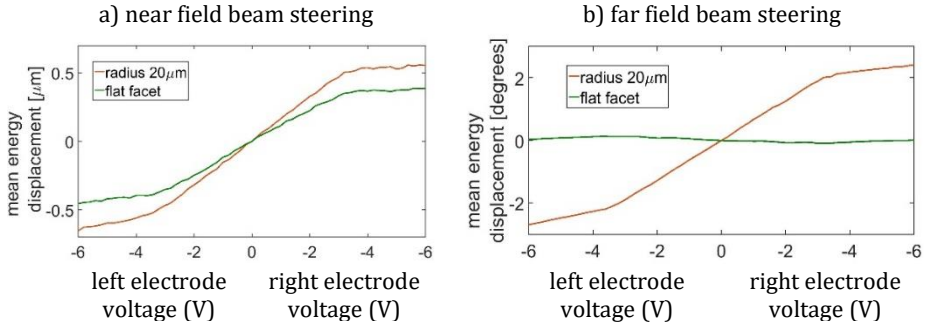

Figure 6-8. Mean energy displacement for the flat and curved facet device in the a) near field and b) mean energy displacement in the far field.

The total beam steering of 15.4° is predicted for a maximum applied voltage of 6 V. Experimental symmetric beam steering is observed, and the explanation of the steering difference with the predicted results cannot rely on the presence of asymmetric higher order modes at the input of the beam steering device. However, the MMI mode filter connected to the taper of the beam steering device is suspected to generate higher order modes due to an imperfect imaging. The mode filter is directly connected to the taper and higher order modes generated at the taper input might expand and propagate into the beam steering device. The effects that the second order mode has on the near field beam steering has been studied and preliminary results indicate that power content in the second higher order mode can also degrade the simulated near beam steering results up to the experimentally observed values. This is expected also to reduce the far field beam steering. Further investigation is needed to attribute the cause of reduced measured beam steering to the modal content in the second higher order mode. However, a possible suggestion to optimize the PIC design and to promote the single mode presence at the beam steering device input, is to move the MMI at the right of the SOA (see Figure 6-5) far from the taper input, in order to enable higher mode filtering through a long enough 2 μm straight waveguide.

6.3.2 The current driven far field reconfiguration

The far field beam steering is here studied for the current driven beam steering device. The curved facet device is compared with the device with flat facet presented in chapter 5. The flat and curved facet PICs belong to different cells and have been internally fabricated (see appendix 10 for the fabrication details). An

optical microscope photo of the PIC with curved facet is shown in Figure 6-9a. The photo has been vertically extended for visual clarity.

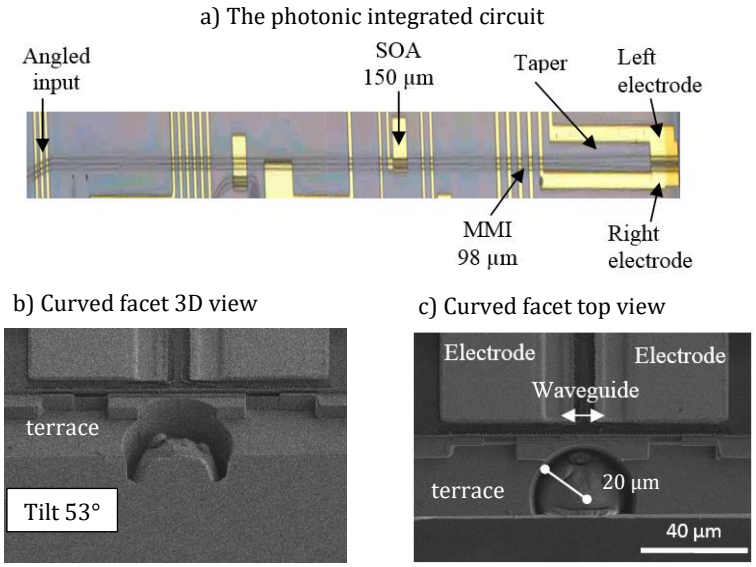

Figure 6-9. a) Optical microscope photo of the photonic integrated circuit, b) angled and c) top view SEM photo of the beam steering device output.

The steering waveguide is 14.5 µm wide and the electrode length is 280 µm. The optical input of the PIC is a waveguide angled at 7°. The end section of the angled waveguide is 2 µm wide. An SOA is inserted after the angled waveguide for alignment purposes. An MMI mode filter connects the SOA and the input waveguide of the beam steering device in order to provide sufficient mode purity. A SEM photo of the fabricated device output section is shown in Figure 6-9c. The top view photo shows the two electrodes, the waveguide underneath and the cylindrical facet. The curved facet has been fabricated by FIB also in this case, however, the initial waveguide facet has been defined by etching and not by cleaving (see appendix 10 for the fabrication details). This explains the terrace, visible in the SEM photos of Figure 6-9, between the etched facet and the cleaved facet.

As for the voltage driven case analysed in previous section, a near filed measurement is performed to be sure to compare far field steering for devices that exhibit comparable steering performance across the chip facet. Near field characterization has been performed by exploiting an optical setup based on the same lenses used for the near field measurement in Figure 6-6. The near field steering curves are shown in Figure 6-10a for the flat and curved facet case. The two devices exhibit comparable performance in the near field. The far field beam

steering characterization for the flat facet case has been performed and a not significant steering has been detected for a maximum applied current of 100 mA. A far field FWHM of 10° is observed for the flat facet current injected device. The far field pattern of the curved facet is shown Figure 6-10b. The far field for the curved facet device presents a FWHM of 35° and beam steering measurements have shown that the radiation pattern is steered out of the field of view of 67°. An alternative method is proposed in next section to characterize the far field beam steering of the current injected device with curved facet.

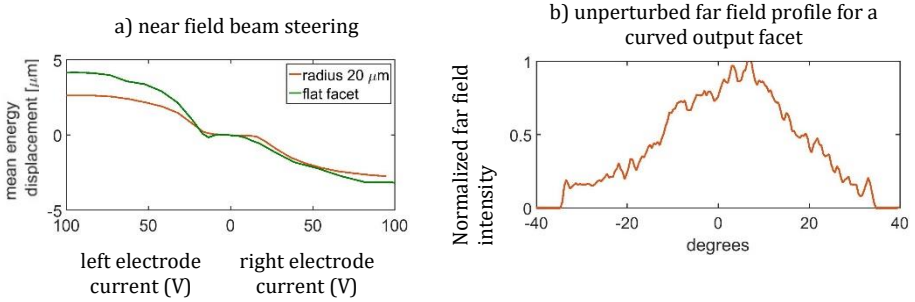

Figure 6-10. a) mean energy displacement in the near field a b) unperturbed far field for the curved output facet.

6.4 Angle of arrival detection

An alternative measurement exploiting an optical fiber as a probe in the far field is here proposed to characterize the total steering range of the device with curved output facet. The proposed measurement is based on the detection of the angle of arrival (AOA) between the emitting optical chip and a receiving optical fiber. The measurement setup for the AOA detection is schematically shown in Figure 6-11a. A laser source provides the optical signal at the optical wavelength of 1.55 μm. An attenuator and a polarization controller are inserted straight after the laser source to control the optical power and to select the TE polarization. A lensed fiber couples the laser light into the PIC. The PIC is at a fixed position and electrically connected to a current source and a power supply to drive the SOA (I_{SOA}) and the electrodes (V_{LEFT} and V_{RIGHT}) of the AOA detection device respectively. The SOA is biased with a current of 3 mA and operated in transparency. The receiver module consists of a flat facet single mode optical fiber, mounted with a focusing lens with focal length of 4.51 mm and diameter of 6.2 mm. An in plane shift along the x axis is applied to the receiver module in order to define an AOA range. The receiver optical module is rotated towards the chip for each position along the x axis. The linear shift of the receiver occurs at a distance of 15 cm from the chip facet. An optical power meter is connected to the flat facet optical

fiber. The measurement procedure is the following. For each angle AOA, the radiation pattern of the PIC is steered by tuning the current injected through the control electrodes. The power coupled to the receiver optical fiber is recorded at each injected current value. An AOA range included between 30° and -30° is studied. The optical power coupled into the fiber, recorded for each current condition and for different AOAs, is shown as a colormap in Figure 6-11b. The optical power has been normalized for each misalignment angle for better visual understanding. The x axis is divided for the left and the right electrode operation. The power is expressed in dB and limited between 0 dB and -10 dB.

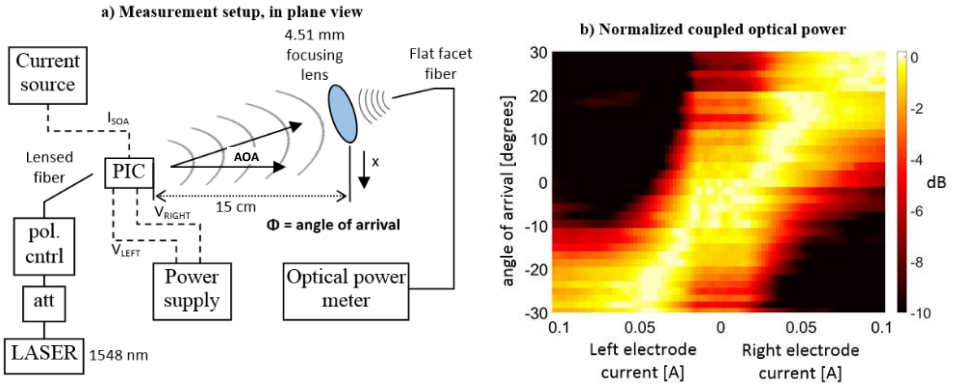

Figure 6-11. a) Setup for the AOA detection experiment and b) colormap of the optical power coupled to the optical fiber for a range of AOAs injected currents.

The colormap shows that optimization of the coupled power can be achieved by tuning the current applied to the control electrodes. The AOA can be continuously detected in the considered angle range of 60°, since a maximum in the coupled power can be obtained for each angle. At the angle of 30°, the coupled optical power is optimal for the maximum current of 100 mA and further angle ranges are not investigated. The wide detection is implemented at the cost of a highly divergent beam with a FWHM of the order of 35° in the horizontal direction. The best absolute coupling efficiency ranges between -48 dB and -61 dB across the AOA detected range.

Transmission loss analysis

An explanation of the transmission losses observed in the AOA detection setup can be addressed by considering three contributions: losses due to the vertical divergence of the optical beam radiated from the chip, to the horizontal divergence and to mode mismatch with the optical fiber. Vertical and horizontal divergence are

expected to result in a transmission loss of 14 dB and 11 dB, respectively. Mode mismatch losses are calculated by estimating the size of the optical beam focused into the fiber by the lens with 4.51 mm focal length, and by applying the butt-coupling theory [107] between the focused spot and the fiber optical mode. The focused beam is expected to be de-magnified and diffraction limited, and is assumed as a Gaussian beam with a beam width $w_0 = 1.7$ μm (half beam size at $\frac{1}{e^2}$ intensity drop) if the Rayleigh diffraction limit definition is used [108]. A mode size mismatch loss of 10 dB is estimated. A total transmission loss of 35 dB has been estimated for the beam steering device with cylindrical facet radius of 20 μm. The gap between the experimental and the estimated data may be attributed to a further mode profile mismatch loss contribution coming from the poor beam quality observed in Figure 6-10b, expected to be compromised by the terrace shown in Figure 6-9. Further investigation would be needed to validate the given hypothesis. Losses due to the vertical beam divergence might be compensated through vertical collimation and the mode size mismatch loss might be addressed by applying a lens to the fiber facet. The loss due to the horizontal beam divergence can be reduced by using an integrated cylindrical lens with larger radius. A loss reduction of 7 dB has been predicted with a 100 μm radius lens, at cost of a total beam steering reduction up to 12°.

6.5 Conclusions

A cylindrical facet has been fabricated through FIB at the output facet of the beam steering device to enhance far field beam steering, and both voltage and current driven beam steering devices have been tested. A total tuning range of the order of 5° has been observed for the voltage driven device. The flat facet version of the beam steering device has shown not significant steering in the far field region. Tracking of an optical fiber has been demonstrated for an AOA range of ± 30°. A transmission loss larger than 48 dB has been observed during the AOA detection. While the loss contribution due to vertical divergence and mode size mismatch can be ideally compensated, the reduction of the loss due to the horizontal divergence has to be traded off with a steering range reduction. A further transmission loss of 13 dB may be attributed to a poor beam quality, which we suspect to be affected by the terrace between the cleaved and the FIB processed facet. The FIB fabrication time per device is relatively slow, of the order of tens of minutes, and is not practical for wafer level processing. The possibility of fabricating curved facets at wafer level is investigated in next chapter, together with a solution to achieve an obstruction free optical aperture.

7 Manufacturing method for etched facets[5]

7.1 Introduction

The fabrication of optical facets through plasma etching is attractive to realize functional on-chip terminations with arbitrary shape [105], [109], [110] at wafer level. Inductively coupled plasma (ICP) reactive ion etching (RIE) is the commonly used technique to etch waveguide sidewalls [111] and laser mirrors [112] in InP technology. Etched facets require high quality smoothness and verticality, and several etching chemistries have been investigated. Etching through Cl_2 has shown good smoothness [91] but it may suffer from anisotropy and poor facet verticality [113]. Anisotropy has been improved by adding Ar to Cl_2 [114], however, good verticality has been demonstrated for a chamber pressure $\leq$ 1 mT [115], which is not available on all ICP systems. $Cl_2/H_2/Ar$ provides anisotropic etching at a more practical pressure, and has shown good smoothness and verticality in the fabrication of distributed Bragg reflectors [116]. ICP RIE based on $Cl_2/H_2/Ar$ has been exploited in [117] to fabricate angled etched facets.

A problem investigated in [117] is the obstruction of the output optical beam due to the terrace separation originating between the etched and the cleaved facet. Common InP based waveguides radiate highly vertically divergent beams and die singulation has to be performed with an accuracy comparable to the depth of the etched facet, usually on the order of 1 – 5 µm. InP dies are commonly singulated through "scribe and break" technique [118]. A diamond tip scribes the semiconductor to make a scribe mark, which is broken afterwards by applying forces in three points. Best in class commercial dicing machines can enable sub-micrometer positioning of the diamond tip. However, the scribed mark is imperfect and the final cleaved facet is defined with a position accuracy on the order of 10 µm [119], [120]. Since "scribe and break" techniques may not be suitable for singulation of dies with etched facets, alternative solutions have to be explored.

The optical terrace problem has been approached in [117] by Br_2 based wet etching of a V-groove running all the way in front of the etched facets. A schematic of the solution proposed in [117] is shown in Figure 7-1.

[5] The fabrication and measurements employed for the writing of this chapter have been performed by Simone Cardarelli. Smart Photonics has performed grinding, polishing and back side metallization of the reported chip.

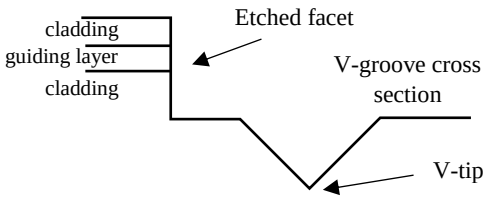

Figure 7-1. Schematic of the solution proposed in [117] to achieve an obstruction free etched facet.

The V-groove tip defines the singulation line, and a distance of 25 µm between the etched and the cleaved facet has been achieved. Even though the resulting terrace enables an improved degree of clearance due to the V shape, still it may represent an obstruction for edge coupled micro-optics or fibers. Smaller cleaved/etched facet distance can be fabricated with a narrower V-groove. However, a narrower V-groove would result in a shallower V-groove tip and this may compromise the cleaving yield since the cleaving capability of a wafer depends on the relationship between the scribe mark depth and the wafer thickness [121].

In this chapter we propose a strategy to realize high quality and obstruction-free etched facets. The strategy is based on employing wet etched grooves as scribe marks, to achieve highly controlled separation between etched and cleaved facets. The scribe mark works as a starting point for the cleaving line, which can be ideally designed at a sub-micrometer distance from the etched facets. High quality etched facets are produced through $Cl_2/H_2/Ar$ plasma chemistry, whereas the scribe mark is fabricated through an HCl/H_3PO_4 based wet etching [11]. The quality of the plasma etched facets is analysed through comparison with a high quality FIB processed facet. The benefit of the high precision cleaving is shown by studying the impact that different terrace widths have on the optical beam quality.

7.2 Etched facets fabrication

The proposed strategy for the fabrication of etched facets is composed by three macro steps: facet etching, realization of wet etched scribe marks and singulation. The facet etching and the scribe mark wet etching are performed in a front end process (wafer level), whereas the die singulation is a back end process (chip level) and requires handling of wafer bars and chips.

7.2.1 Facet and scribe mark etching

The front end processing has been performed on a (100) oriented wafer 600 μm thick. The layer stack is composed from top to bottom by an InGaAs contact layer, an InP top cladding, an InGaAsP guiding layer and the InP substrate. The process steps for the etched facets and scribe marks realization are described in Figure 7-2 through the schematic cross sections of the processed wafer.

An 800 nm thick SiN mask has been deposited by PECVD and patterned to define the etched facet geometry and the scribe mark locations (Figure 7-2a). Such a thick mask enables deep etch of the optical facets while guaranteeing a negligible erosion of the waveguide top cladding corners. ICP RIE with CH_4/H_2 is applied to expose the InGaAsP layer which is used as mask for the final scribe mark wet etching. The ICP etching is performed up to 100 nm into the InGaAsP layer (Figure 7-2b). The SiN mask areas defining the optical facets are protected by hard baked AZ resist during the CH_4/H_2 ICP steps, in order to retain a sufficient thickness for the deep facet etching. A further CH_4/H_2 plasma step is performed to access the InP substrate in the scribe mark trench (Figure 7-2c), using AZ resist as a mask. ICP RIE with $Cl_2/H_2/Ar$ chemistry at 200° is applied for 6 minutes to realize 4.6 μm deep etched optical facets (Figure 7-2d), using polyimide to protect the rest of the wafer. The wafer is rinsed in a 10 minutes water bath after the Cl_2 based dry etching, to suppress the risk of HCl formation due to a possible reaction between Cl_2 residues and air. Wet etching of the scribe marks is applied for 10 minutes through HCl/H_3PO_4 with a 5:1 ratio, only at the end of the front end process flow. The concentration in water for HCl and H_3PO_4 is 36 % and 85 % respectively. The scribe mark is 180 μm long and 20 μm wide. A 7.6 μm thick AZ resist protects the wafer during the wet etching step (Figure 7-2e). The wafer is finally thinned up to 250 μm in order to ease the cleaving procedure.

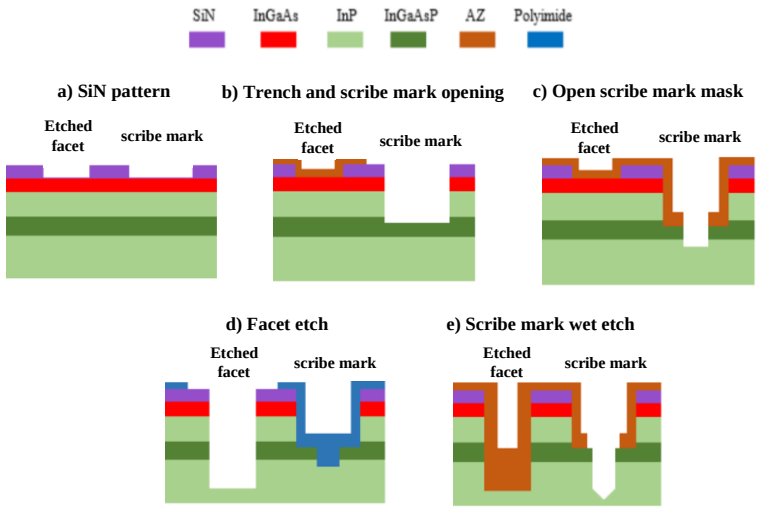

Figure 7-2 Schematic cross sections of the processed wafer during the facet/scribe marks fabrication steps.

Etched facet roughness

The quality of the fabricated etched facets is characterized through comparison with a reference high quality facet polished through FIB. The FIB has been applied with single pass ion mode, with an acceleration voltage of 30 kV, beam current of 2.7 nA and dwell time of 2 ms. A SEM photo of the etched facet and the reference facet are shown in Figure 7-3 for a first qualitative analysis.

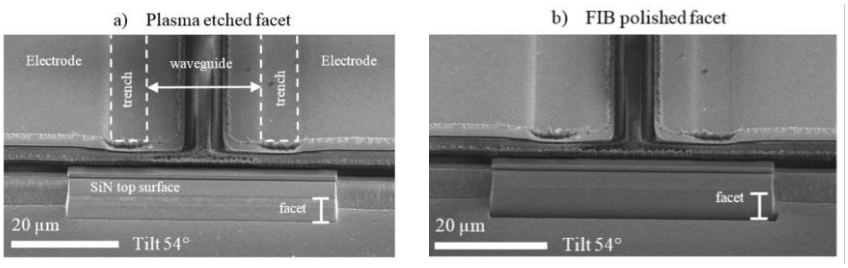

Figure 7-3. SEM photo of a) plasma etched facet and b) FIB polished facet.

The photo is acquired by setting an electron acceleration voltage of 5 kV. The facet is indicated by the double T solid line. The SiN mask defining the facet geometry is still present at the end of the batch processing. There are two electrodes overlapping the central waveguide, but those are not used in this work. The morphology of the two waveguide trenches is visible underneath the electrodes. By comparing the two SEM photos, it is visible that the plasma etched facet exhibits a

higher level of roughness with respect to the FIB polished facet, which appears to be highly uniform. The observed roughness is attributed to a projection of the SiN mask roughness into the semiconductor during dry etching. A poor facet roughness may affect the performance of optical devices [13], leading a quantitative facet characterization which is performed through atomic force microscopy (AFM).

The AFM measurement has been performed in tapping mode, by a 10 µm high scanning tip with a full cone angle of 10 °. The facets are scanned horizontally from bottom to top over a window of size 4.2 µm x 10 µm. AFM measurement of the FIB processed facet is also performed for comparison. Figure 7-4 shows the measured surface for a plasma etched facet (Figure 7-4a) and the FIB etched facet (Figure 7-4b).

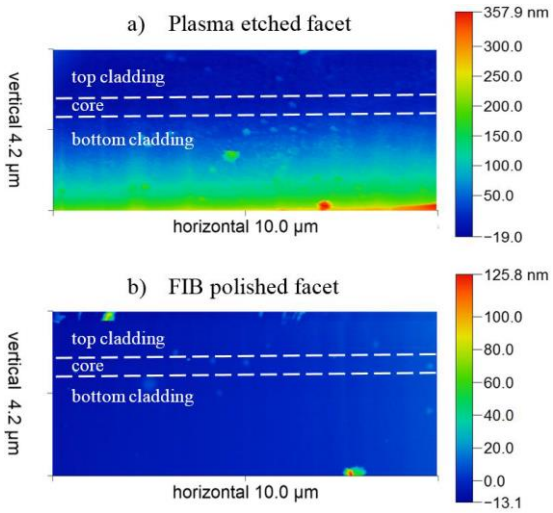

Figure 7-4. AFM surface measurement for a) plasma etched facet and b) FIB polished facet.

The waveguide core is marked for both the facets by the dashed white lines. A concave curved profile (from blue to green) is observed for the plasma etched facet whereas a flat facet is obtained by FIB. The plasma etched bottom cladding deviates of 200 nm with respect to the top cladding. This motivates a study of the side wall angle of the facet. A vertical line has been extracted from the measured surface and fitted though a quadratic polynomial. The fitting function has been calculated at the edges of the guiding layer, and the gradient between the two obtained points has been used to compute the side wall angle. The 90° reference plane is fixed by the upper part of the top cladding which is the first part to be etched and is assumed to be perfectly vertical. A side wall angle of 85.4° is measured for the plasma etched

facet in the core region. The facet roughness has been quantified in terms of root-mean-square (RMS). Surface variations due to the SiN mask roughness or material re-deposition from FIB polishing, can be detected by decoupling the slow surface variations from the measured AFM data. Slow surface variations have been removed by background extraction. The background of the measured surfaces has been extracted and removed through a two dimensional polynomial interpolation, with a polynomial of the second order in both directions. The plasma etched facet and the FIB polished facet exhibit a roughness of 7 nm and 1 nm, respectively. Good quality facet is achieved if compared to the roughness of a cleaved facet, which has been measured to be of the order of 1 nm.

7.2.2 Singulation

Singulation is defined in two steps: a bar and a die separation step. These are implemented through a preliminary cleaving and a precision cleaving step. A schematic top view of a wafer area is shown in Figure 7-5a to help the procedure explanation.

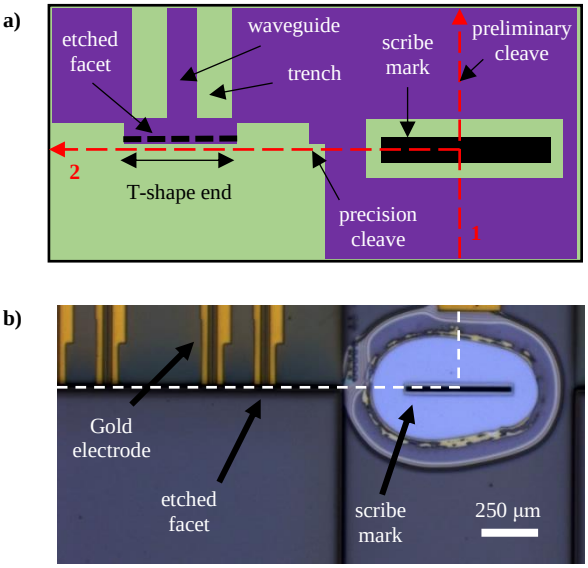

Figure 7-5. a) Schematic top view of a wafer area to explain the cleaving procedure, b) microscope image of the etched facets and scribe mark.

A bar of chips is initially separated from the wafer through two preliminary cleaves, perpendicular to the optical facets. The standard “scribe and break” technique is used for the preliminary cleaving. One of the two preliminary cleaves

(red dashed arrow labelled with the index 1 in Figure 7-5a) is defined in the middle of the scribe mark. When access to the scribe mark cross section is provided, the scribe mark can be exploited as a weakness point to perform the precision cleaving (red dashed arrow labelled with the index 2 in Figure 7-5a) for the final die separation. The precision cleaving occurs by applying force to the scribe mark through the rolling break wheel of an LSD-100 (LOOMIS) dicing machine. The precision cleaving line is generated from the middle of the scribe mark and is designed at a distance of 4 μm from the etched facet. The scribe mark design is aligned with the wafer flat. The distance between the designed cleaving line and the etched facet is employed as a safe margin to allow a 0.02 ° angle tolerance of the wafer flat orientation with respect to the crystalline structure, defined by the wafer specifications. The waveguide trenches are designed 10 μm far from the etched facet. The gap between the trenches and the facet causes the T-shaped waveguide end. The extension of the waveguide trenches up to the etched facet would generate critical rounding of the waveguides edges due to diffraction effects occurring during the SiN mask lithography. This is avoided since might impact the beam quality. The same T-shape waveguide concept has been used in [110] with a distance of 2 μm between the trenches of a 2 μm wide waveguide and the etched facet. A larger trench-to-facet distance may affect the field at the etched facet due to the free lateral propagation in the slab waveguide of the T-structure end. The trench-to-etched facet distance employed in this work is 5 times larger than the work in [110], however, the employed waveguide width is 14.5 μm and a consistently smaller lateral divergence is expected to occur in the slab propagation. A T-shape end facet of 50 μm is employed. A top view microscope photo of a processed wafer is shown Figure 7-5b. The photo shows the corner of a cell before applying the preliminary cleaving step to the scribe mark. The black rectangle is the wet etched scribe mark. This is surrounded by an irregular circular area, which is expected to be due to lateral wet etching confined between the p++ contact layer and the InGaAsP guiding layer. Four devices are shown in the photo through the gold electrodes. The etched facet position of one of the devices is indicated.

Cleaving accuracy

The die containing the etched facets characterized in 7.2.1 has been separated from the wafer through the explained cleaving procedure. An optical photo of the die is shown in Figure 7-6 for the design explanation.

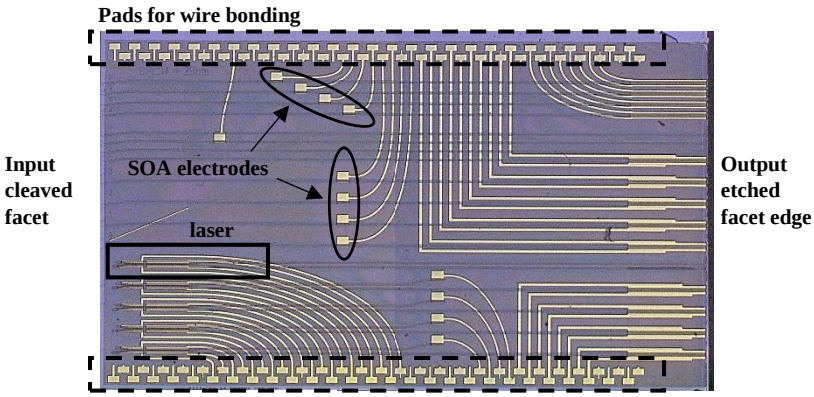

Figure 7-6. Optical microscope photo of the singulated die.

Multiple etched facets are distributed across the die edge indicated as *output etched facet edge*. The etched facets of the waveguides belonging to the upper section of the die are connected to SOAs 150 μm long. The electrodes of the SOAs are indicated by the black ellipses. The SOAs are connected to angled input waveguides on the left side of the chip. The input chip facet is defined by "scribe and break" procedure, resulting in cleaved input waveguide facets. The facets belonging to the lower part of the die are connected to integrated lasers [86]. The spontaneous emission provided by the laser active region is used in this section. The laser is shown in the black solid rectangle. The SOAs and the laser active regions are electrically connected through the wire bonding pads shown in the dashed black rectangles.

The cleaving accuracy for the *output etched facet edge* is characterized by visual inspection of the cleaving line along the etched facets. The SEM top view photo of an area of the cleaved die is shown in Figure 7-7d. The black small rectangle in the top-left corner of the chip indicates the wet etched scribe mark. The scribe mark is placed at the chip corner, 410 μm far from the facets to avoid possible facet damages due to acid lateral erosion occurring during the scribe mark formation. The brighter shapes, indicated as example by the dashed black rectangles, are electrodes. The area with angled lines is the chip holder. The waveguide in the left red rectangle (Figure 7-7d) is the closest to the scribe mark and is named *reference* waveguide. The *reference* waveguide is expected to exhibit best cleaving accuracy with respect to the rest of the waveguides. This is motivated by the fact that the cleaving deviation with respect to the designed line (due to a rotation alignment tolerance of the waveguide mask with respect to the crystal) is limited in proximity of the scribe mark. A higher magnification photo of the *reference* waveguide termination is shown in Figure 7-7a to quantify the cleaving precision,

and a cleaved-to-etched facet distance smaller than 1 μm is observed, however, a distance of 4 μm is expected by design. This is attributed to a crystal jump occurring between the scribe mark and the *reference waveguide*. Multiple crystal jumps or direction changes may occur during the cleaving line propagation, and a SEM analysis is performed for a waveguide termination at the opposite side of the die, with respect to the scribe mark. Figure 7-7c shows that a facet/cleaving line distance of 17.7 μm is observed at 2900 μm from the reference waveguide. A cleaved-to-etched facet distance analysis is performed all along the die edge to understand where the cleaving line deviations originate and how this affects the rest of the etched facets. Figure 7-7b shows the cleaved-to-etched facet distance across the die for a set of thirteen waveguides. The x axis represents the distance between the analysed optical waveguide and the *reference* waveguide. Data points in Figure 7-7b are aligned with the waveguides in the SEM cell photo (Figure 7-7d) for better visual understanding. The cleaved facet is aligned with the etched facet over a distance of 1150 μm from the reference waveguide, with a cleaved-to-etched facet distance shorter than 1 μm. The cleaved line exhibits a deviation of 0.9 μm at a distance of 1400 μm, the deviated cleaving direction propagates across the chip with an angle of 0.6° with respect to the initial direction.

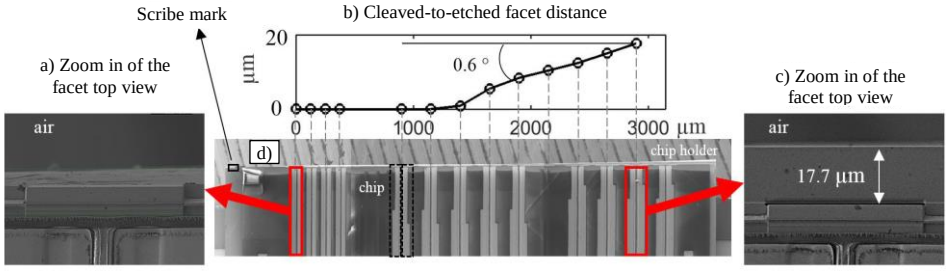

Figure 7-7. a) zoom in of the optical facet for the device adjacent to the scribe mark; b) cleaved-to-etched facet distance across the die edge; c) zoom in of the optical facet for a device on the opposite side of the scribe mark; d) SEM top view photo of the die.

The scribe mark

The error in the cleaved line direction for the *reference* waveguide and the observed sudden deviation of the propagation angle motivate a deeper investigation of the quality of the scribe mark. The SEM photo of the cross section of the employed scribe mark is shown in Figure 7-8a. The photo has been acquired after cleaving and the missing half scribe mark is represented by the dashed black line. The expected tie-shape scribe mark is observed and the cleaving line started at the lowest tip of the mark with an offset of 2 μm. The scribe mark depth is 63 μm. This offset between the cleaving line origin and the tip of the tie-shape groove has not

been observed in separated experiments for a 500 μm long scribe mark. A longer scribe mark enables a longer definition of the groove tip, and this is suspected to enable higher cleaving yield. No significant under-etching with respect to the InGaAsP wet etch mask was observed, however, a lateral acid erosion of the InP top cladding confined between the InGaAs and the InGaAsP layers occurred, possibly due to the poor adhesion between the AZ resist and InGaAsP. The acid propagates up to the dry deep etched area which is unprotected from the InGaAsP layer, causing deep InP erosion. A crystal plane jump is observed at the beginning of the InP eroded area, which is shown in Figure 7-8b. The InP acid erosion can be easily avoided by placing the scribe mark sufficiently far from the etched facet area.

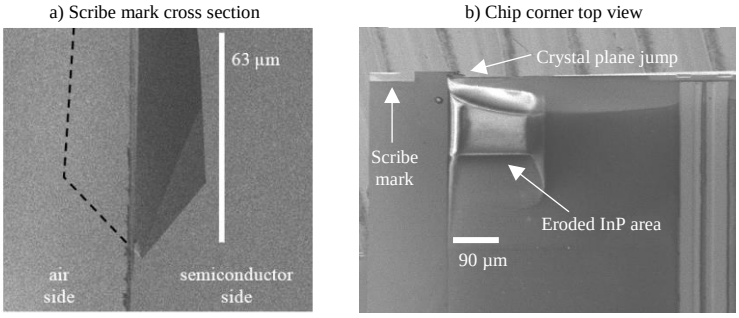

Figure 7-8. a) SEM photo of the scribe mark cross section and b) SEM photo of the die corner top view.

7.3 Optical beam quality

In this section, the effect that the measured roughness has on the optical beam profile is characterized in terms of near and far field measurements, for the etched and the FIB processed facet. Output waveguides with the cleaved facet perfectly aligned to the etched facet are considered for this experiment.

7.3.1 Near and far field characterization

The optical beam profile emitted by the plasma etched optical facet is compared with the radiation profile of the FIB polished optical facet, in terms of near and far field. Plasma and FIB etched facets with perfectly aligned cleaved facets are considered for this experiment. The optical facets have been excited by an external laser with a TE polarized electric field at the optical wavelength of 1.55 μm. The intensity profile of the electric field at the output facets has been magnified and recorded through a near field imaging setup. Two anti-reflection (AR) coated lenses of focal length 2 mm and 750 mm magnify the optical near field. The 2 mm focal lens collimates the output beam, the focusing 750 mm focal lens is 11 cm far from

the collimating lens. The magnified field is recorded at a distance of 75 cm far from the focusing lens, by an infrared camera (Xenics) with 320 x 256 pixels. The far field measurement setup is obtained by substituting the 750 mm lens with two lenses of focal length of 150 mm and 250 mm, placed at a distance of 19 cm and 71 cm from the collimating lens. The lateral profile passing through the maximum intensity point is extracted and normalized.

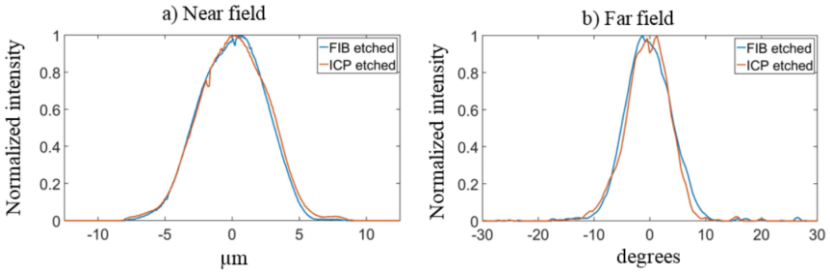

Figure 7-9. a) Lateral near field and b) lateral far field for the plasma and FIB etched facets.

The acquired near and far field are shown in Figure 7-9. Both the output facets exhibit a beam with FWHM of 6 µm and 9° for the near and the far field, respectively. A near and far field FWHM of 8 µm and 6.6° is simulated and the experimental deviation is expected to be attributed to the presence of higher order modes. Horizontal beam scattering has not been detected for both the plasma etched facet and the FIB polished facet. A difference of 7.5° in the vertical radiation angle has been measured between the plasma and the FIB etched facet, which is attributed to the difference in verticality between the two optical terminations.

7.3.2 Singulation requirements

Optical etched facets with perfectly aligned cleaved facets have been fabricated, however, it is interesting to know what minimum level of accuracy is needed to obtain an optically obstruction free facet. The far field of etched facets has been measured for a terrace width ranging from 0 µm to 17.7 µm. An output optical signal with a power of -30 dBm is provided by each facet through the spontaneous emission of the on-chip integrated SOAs. The optical spectrum of the spontaneous emission has an emission peak at 1.56 µm. The on chip optical waveguides are single mode in the vertical direction. The vertical far field profiles for an output facet with terrace width of 0 µm and 5.5 µm are shown in Figure 7-10.

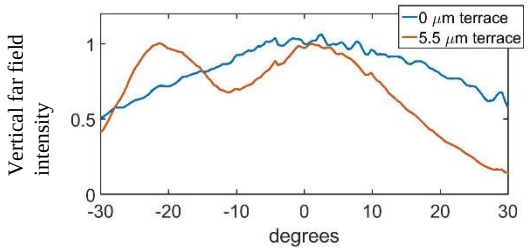

Figure 7-10. Vertical far field intensity profile for a waveguide output facet with 0 μm (blue curve) and 5.5 μm terrace width (red curve).

An interference pattern is visible for the etched facet with terrace width of 5.5 μm. The observed interference is due to reflections occurring from the optical terrace, indicating that the terrace represents an obstruction for the beam. The interference pattern exhibits a field intensity drop at an angle of order of -10°, which is 68 % the initial intensity. Furthermore, a side lobe is visible at an angle of -20°. Far field measurements have been performed for different terrace widths. Results indicate that a cleaved-to-etched facet distance of 0.9 μm is sufficiently precise to obtain a negligible effect of the resulting separation terrace.

7.4 Conclusions

Plasma etched facets have been fabricated and enabled through precision cleaving based on a wet etched scribe mark. AFM measurements performed on etched, FIB polished and cleaved facets have shown roughness of 7 nm, 1 nm and 1 nm, respectively. The near field of the etched facet is in agreement with the field emitted from the high quality FIB polished facet. A scribe mark 63 μm deep, 20 μm wide and 180 μm long has been used to cleave a 250 μm thick sample in proximity of the etched facets. Waveguide terminations with sub-micrometre cleaved-to-etched facet separation have been fabricated, and an obstruction free radiation field has been shown. A cleaving accuracy of the order of 0.9 μm is sufficient to fabricate free obstruction etched waveguides, with a guiding layer which is 2.5 μm far from the etched bottom surface.

.

8 Conclusions

Optical beam steering has been demonstrated across the facet of an optical chip, by electronically controlling the refractive index profile of a single optical waveguide. The proposed method based on two-mode interference has enabled sub-micrometre beam steering with the use of two electrodes only. The low level of requested electrical connectivity makes this solution interesting for scalable designs and more complex circuits such as optical switches and LIDAR systems. Furthermore, the footprint of the proposed device is relatively small if compared to beam steering solutions based on MEMS or optical phase arrays.

A beam steering of ± 1 μm across the chip facet has been experimentally demonstrated for a reverse bias voltage driven and current injected device with a maximum electrical power consumption of 240 mW and 35 mW, respectively. Reverse bias voltage control was expected to enable lower power consumption operation with respect to the current injection device. However, the employed technology has shown that the voltage driven device efficiency is compromised by the leakage current path present between the control electrodes. Reverse bias voltage is expected to enable sub-microwatt power consumption beam steering with improved electrical isolation between the p-electrodes. It is suggested that this can be achieved with a selectively doped top-cladding.

An extended steering range of ± 4 μm has been achieved with the current injected device by employing larger electrical power up to 420 mW. The best beam steering across the chip facet has been reported in the literature through a tuned MMI solution with a steering efficiency of 0.57 μm/mA, and electrode length of 500 μm. In this work, a current injection steering efficiency of 0.056 μm/mA has been demonstrated with an electrode length of 280 μm. This is an order of magnitude lower with respect to the state of the art. However, the device studied in this work is based on bulk materials and steering efficiency improvements can be addressed by introducing multiple quantum wells for enhanced electro-refraction in the guiding layer.

The proposed beam steering has shown sub-micrometre resolution steps and in principle enables continuous tuning. This has been used to investigate precision control of on-chip and off-chip optical coupling. A numerical model of on-chip coupling has shown that continuous beam steering enables optimal switching between two ports with sufficient beam quality. This has been demonstrated through simulations of a 1 x 2 optical switch based on the proposed beam steering device. Simulation results have shown that the beam quality of the steered beam is sufficient to achieve switching performance comparable with the state of the art MZI switches.

The off-chip coupling characteristics of the beam steering device has been studied through a chip-to-fiber coupling experiment. The experimental results have shown that the possibility of steering an optical beam can improve the optical coupling when a misalignment is present between the chip and the fiber, despite the steered beam asymmetry. Beam steering has enabled an enhancement of the in-plane -1 dB misalignment tolerance up to 7.6 µm, an improvement of 60% if compared to a conventional mode converter based on passive lateral tapering.

Beam steering in the far field has also been investigated. The combination of the beam steering device with a curved optical facet has been proposed to achieve wide beam steering in the far field. A 20 µm radius diverging cylindrical facet has been etched by FIB at the output section of the beam steering device. An enhancement of the full far field beam steering range up to 5° and 60° has been measured for the voltage and current driven beam steering device respectively. This improvement comes at cost of a higher lateral beam divergence on the order of 35°. Improving beam divergence for the devices described in this thesis is interesting for future investigation. This might be addressed by using the proposed beam steering device to excite different parts of an array of waveguides. This would be similar to optical phased arrays, but the number of electrodes, power consumption and control complexity would be greatly reduced.

A process flow to enable the fabrication of etched facets at wafer level has been proposed, in order to replace the time consuming FIB process step used to shape the beam steering device output facet. High quality straight facets with a roughness of 7 nm have been produced, and obstruction free radiation is achieved after singulation thanks to the proposed precision cleaving strategy. We have shown that a cleaving accuracy of the order of 0.9 µm may be necessary to fabricate obstruction free etched facets. The needed cleaving precision represents a problem when fabricating diverging (concave) lenses with low radius, since a minimum cleaved-to-etched facet separation is unavoidable. As future work, exploring the possibility of integrating Fresnel lenses as output etched curved facets is attractive to achieve a compact lensing solution while complying with the strict singulation requirements.

9 Appendix - Piezoelectric based fiber aligner in two dimensions[6]

9.1 Introduction

In parallel with the electro-optical beam steering work, an alignment technique based on piezoelectric actuation has been developed in collaboration with *VTEC lasers and sensors*. We propose a proof of concept alignment system based on the combination of two bimorph piezoelectric actuators capable of bending when driven with voltage. Coupling experiments with and without alignment compensation, are performed between an InP/InGaAsP based laser and a lensed single mode optical fiber to show the benefits of the piezo benders as manipulators in a critical optical alignment situation.

9.2 Two dimensional piezoelectric actuator

9.2.1 Design and principle of operation

The 3D schematic and the electrical configuration of the proposed alignment system are shown in Figure 9-1a. The two commercially available bimorph piezoelectric actuators and the optical fiber are fixed together through epoxy. A spherical lens with radius of 7.5 μm is applied to the fiber output facet to optimize the optical mode matching. The optical fiber is a single mode fiber with core diameter of 8.2 μm. Each of the piezo actuators is composed by a stack of two PZT ceramics layers separated by a metal plate electrically connected to ground. A second metal plate is present on one of the external sides of the piezo actuators. Control pads are available from the metal plates to operate the actuators by voltage control. The horizontal actuation piezo is rotated 90° with respect to the vertical actuation piezo to enable two dimensional fiber displacement.

[6] The measurements employed for the writing of this appendix have been performed by Simone Cardarelli.

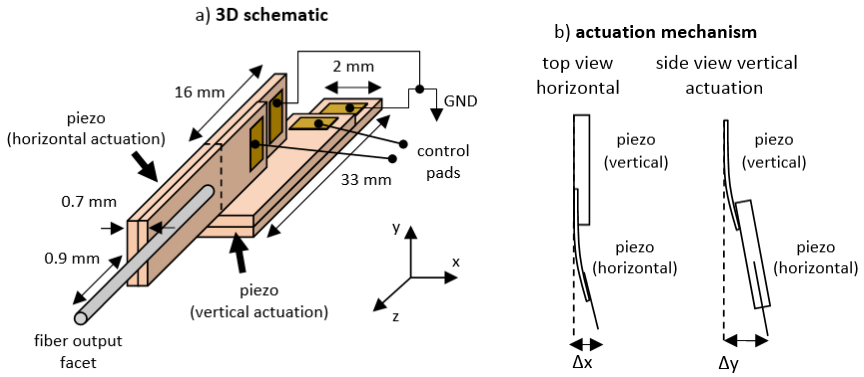

Figure 9-1. a) Schematic of the alignment assembly and b) the actuation mechanism.

The actuation mechanism is shown in Figure 9-1b. The piezo actuators are bent by applying voltage to the control pads. Horizontal and vertical displacement of the fiber can be independently achieved by applying voltage to the horizontal and vertical piezo, respectively.

9.2.2 Piezo assembly characterization

The proposed alignment system should exhibit sub-micrometric resolution, long range displacement and low vibration in order to assure reliable optical coupling. Displacement, creep and vibration have been characterized by injecting light through the shifted optical fiber while monitoring the beam position at the fiber output with a near field imaging setup. The schematic of the setup is shown in Figure 9-2. Optical connections are represented by the solid lines whereas the dotted thick lines represent electrical connections. The light source at 1550 nm and with an optical power of -6 dBm is provided by an external laser. The beam at the output fiber facet is collimated by a 2 mm focal length lens and focused by a lens with focal length of 200 mm to achieve a magnification of 100. The magnified beam at the image plane is recorded by a Xenics infrared camera with 320 × 256 pixels. A 20 dB optical attenuator is placed in the optical path in order to avoid the saturation of the camera pixels. Two power supplies with maximum output voltage of 25 V provide the electrical signals to the piezo actuators. The vertical displacement capability of the piezo system is characterized by applying a voltage sweep to the vertical actuation pad from 0 V to 25 V and back to 0 V with 1 V step, while keeping the horizontal pad at 0 V.

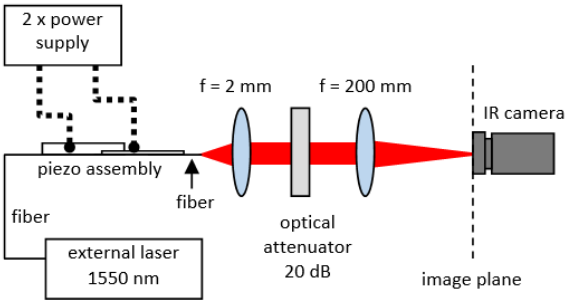

Figure 9-2. Near field imaging setup

The same experiment is performed for the horizontal characterization by sweeping the voltage applied to the horizontal actuator while keeping at 0 V the vertical actuator. The imaged beam is recorded at every voltage step and fitted by a Gaussian function. The position of the beam relatively to the camera sensor is represented by the center values of the Gaussian distribution. The beam position represents the fiber displacement through the applied voltage range and is shown in Figure 9-3a for both vertical and horizontal actuation. Comparable displacements of 49 µm and 41 µm are achieved for the vertical and horizontal actuation respectively. The typical piezoelectric hysteresis behavior is observed as well with a difference of 4.8 µm between the increasing and decreasing displacement at 12 V. A 2.3 µm difference between the start and the end of the experiment is attributed to the piezo creep. A two dimensional scanning window is obtained by combining vertical and horizontal operation. Figure 9-3b shows the two dimensional displacement of the beam when the two actuators are operated simultaneously. A voltage of 12.5 V is applied to the actuators for the spot in the middle of the sensor, the left and right spots are obtained by applying 0 V and 25 V to the horizontal actuator while keeping at 12.5 V the vertical actuator. The lower and upper spots are achieved by applying 0 V and 25 V to the vertical actuator while keeping at 12.5 V the horizontal actuator.

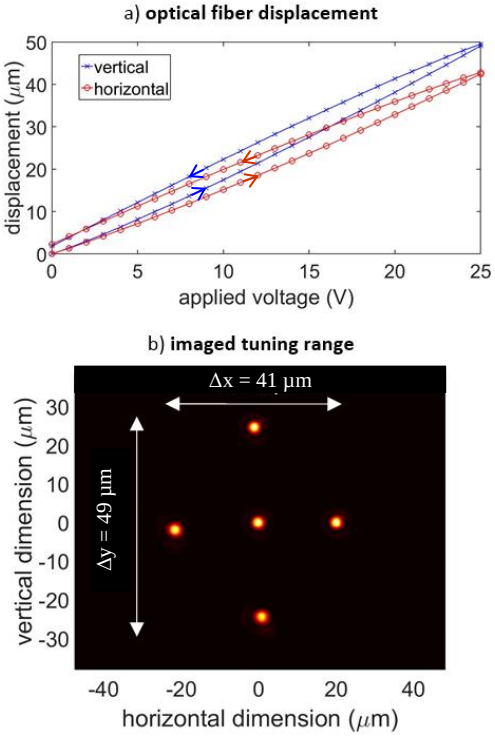

Figure 9-3. a) Optical fiber displacement for vertical and horizontal actuation b) near field image of the output beam of the optical fiber for different fiber positions.

Creep has been characterized for a time length of 30 minutes by applying 25 V to both the actuators while monitoring the beam position at a frame rate of 4.6 Hz. A total drift of 5.4 µm and 3 µm with an initial gradient of 0.5 µm/minute and 0.4 µm/minute has been recorded for the vertical and horizontal directions. A vertical vibration of the order of 0.1 µm is detected as difference between the upper and lower envelope of the recorded beam position, no significant vibration is observed for the horizontal case. A maximum electrical current of 2.6 nA and 0.9 nA is measured for the two actuators at 25 V, indicating a sub-microwatt maximum alignment power if used in-situ.

9.2.3 Photonic integrated circuit

The optical chip exploited for the coupling experiment has been fabricated by the III/V SMART Photonics foundry through the JEPPIX multiple wafer run (MPW) service [85]. Figure 9-4a shows a photograph of the PIC.

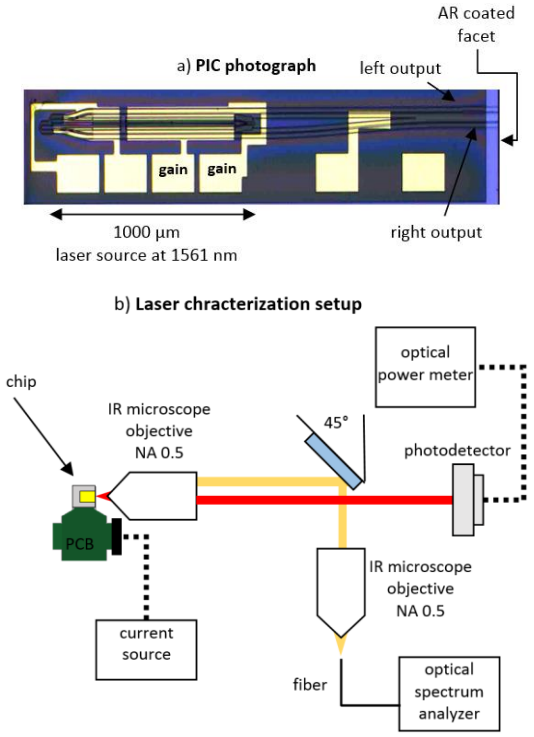

Figure 9-4. a) Photograph of the photonic integrated circuit b) experimental setup for the characterization of the optical spectrum and power of the integrated laser.

The light source is provided by an integrated coupled cavity laser [86] which is composed by two phase sections, two gain sections, two multimode interference mirrors and two output ports. The phase sections are not electrically connected for this experiment. The two laser output waveguides are 2 µm wide and separated by 25 µm at the chip facet. The output facet of the chip is anti-reflection coated. The *gain* section electrodes have been ball bonded to the external printed circuit board to provide the electrical signals. The absolute output optical power of the laser has been measured by the setup shown in Figure 9-4b. The small yellow rectangle represents the InP optical chip. An infrared coated objective with numerical aperture of 0.65 collects the output power of both the laser outputs. The beam coming from the output port used for the coupling experiment is focused into a photodetector connected to the optical power meter. The beam from the other laser output is reflected by a 45° angled mirror and focused into a flat facet optical fiber connected to the optical spectrum analyzer. The chip temperature is stabilized by a water cooling system with temperature set at 18° C. The current source drives the gain sections with currents of 49 mA and 40 mA to operate the laser at the wavelength of

1561 nm and with a side mode suppression ratio of 36 dB. An optical power of -2.85 dBm is measured by the optical power meter for the laser output used for the coupling experiment.

9.3 Fiber-chip coupling

Fiber-to-chip coupling experiments are performed with and without alignment compensation to show the benefit of the bimorph piezo actuators in terms of optical coupling efficiency. The optical coupling experimental setup is shown in Figure 9-5. The piezo assembly is mounted on top of a six axes stage which is stabilized by a nano controller through closed loop control. The lensed optical fiber is on one side coupled to the chip and on the other side connected to a 99:1 power splitter in order to monitor optical power and spectrum. The 99 % power is measured by the optical power meter while 1 % travels to the optical spectrum analyzer. The synchronization of the measurement tools occurs by MATLAB script through USB and GPIB interfaces.

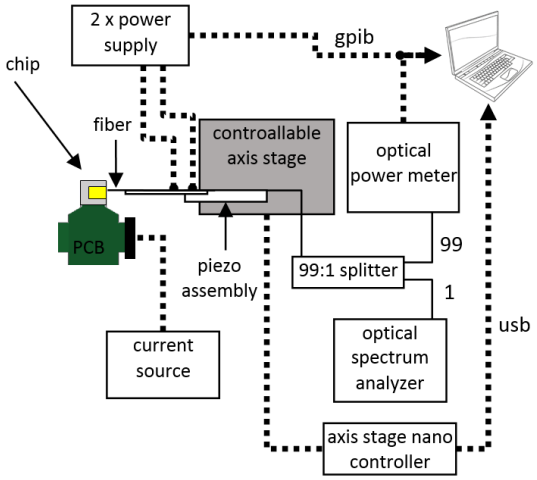

Figure 9-5. Experimental setup for misalignment losses characterization and compensation.

Experimental procedure

Coupling efficiency without piezo assembly compensation is characterized for different fiber-chip misalignments introduced by the nano-controlled stage. Coupling efficiency is quantified by subtracting the power measured from the optical power meter (Figure 9-5) from the laser output power measured in section

III. The transmission power is initially optimized by controlling the fiber position, afterwards the fiber is translated across the plane parallel to the chip facet while recording the coupled optical power. The distance between the fiber and the chip facet is initially optimized and fixed during the experiment. The coupling efficiency is recorded along six fiber paths shown in Figure 9-6. The dashed lines indicate the movement of the fiber and the arrows indicate the direction of travel. The ridge orange profile represents the laser output waveguide and the crossing point of the dashed paths indicates the position of maximum optical power coupling. The optical fiber is shifted by vertical and horizontal steps of 400 nm.

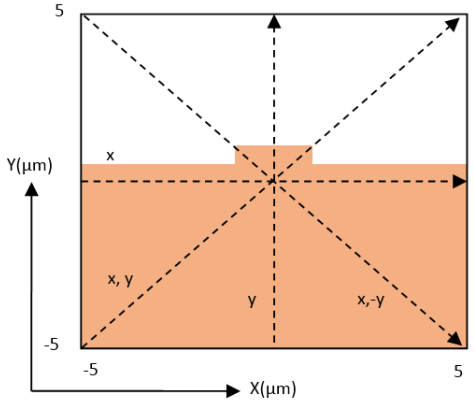

Figure 9-6. Movement of the fiber relative to the waveguide.

A second coupling experiment is performed by activating the piezo-assembly for misalignment compensation. A bias voltage of 12.5 V is applied to the vertical and horizontal piezo actuators to enable sufficient compensation range for negative and positive misalignments. After initial power optimization the fiber position is re-scanned in front of the chip (along the paths shown in Figure 9-6). The coupling power is optimized for each misalignment position by tuning the voltage applied to the piezo actuators.

9.3.1 Piezoelectric misalignment compensation

The coupling efficiency along the different paths for both the compensated and non-compensated cases is shown in Figure 9-7. Results for the vertical and horizontal shifts are shown in Figure 9-7a whereas Figure 9-7b shows the results for diagonal fiber movements. The x axis shows the offset from the optimal transmission power position. The curves with circles and cross markers show the coupling efficiency when no compensation is present during the scanning, the hexagon and diamond markers identify the recorded coupling efficiency when the

piezo compensation is active. A maximum coupling efficiency of -2.1 dB is obtained for zero misalignment. The 2.1 dB loss are attributed to the InP waveguide-lensed fiber mode mismatch. When misalignment compensation is applied to the optical system the coupling efficiency is fixed at -2.1 dB over the full 100 μm^2 misalignment window. The voltage is tuned in a maximum range of 5.8 V around the initial bias point of 12.5 V for both the actuators.

9.3.2 Automatic compensation

A further coupling experiment has been performed to test the piezo assembly over longer operational time. A preliminary control algorithm has been developed to automatically optimize the coupling efficiency during the experiment. The recorded profile of the coupling efficiency (Figure 9-7) exhibits a typical central main lobe, enabling the possibility of using the *hill climbing* optimization technique [122].

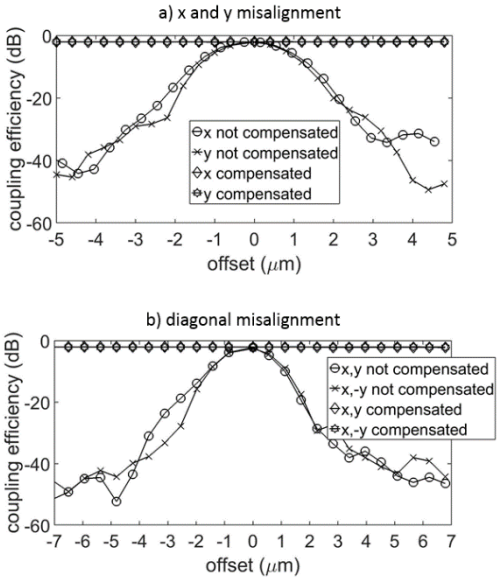

Figure 9-7. Coupling efficiency in the a) vertical and horizontal misalignment case and b) diagonal misalignment case.

This technique can be applied in a misalignment window of 3 × 3 μm^2, larger misalignment may cause the alignment system to stop in a local minimum state for which a random optimal search would be needed. The *hill climbing* technique monitors the spatial gradient of the coupling efficiency in order to move the fiber toward the optimal point. The gradient measurement is achieved by driving the piezo actuators with small voltage steps to scan the fiber between two close positions

while measuring the transmitted power. Two voltage steps of 0.2 V and 0.1 V are considered to enable both a course and a fine step displacement of the order of 0.12 µm and 0.06 µm respectively. After generating an initial misalignment of 2 µm in the vertical and horizontal directions the piezo assembly has been activated to perform misalignment compensation for 1 hour experiment. The behaviour of the coupling efficiency and actuation voltage is shown in Figure 9-8.

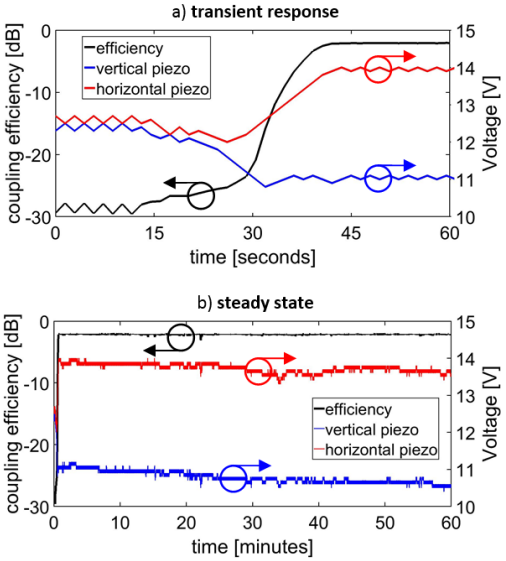

Figure 9-8. Controlled coupling efficiency and actuation voltage of the piezo actuators in a) transient phase and b) steady state.

The transient response of the system during the first minute of experiment is shown in Figure 9-8a. The left y axis shows the coupling efficiency whereas the right y axis is relative to the voltage applied to the piezo actuators. After 45 seconds the coupling efficiency reaches the optical value of -2.1 dB from a starting point of -29 dB while the actuation voltage varies with small steps to constantly monitor the optical coupling with low alignment perturbation. The coupling efficiency remains optimal in the steady state phase as shown in Figure 9-8b, the actuation voltage reduces from 14 V (11.1 V) to 13.5 V (10.5 V) in the x (and y) directions to compensate for an estimated total misalignment of the order of 0.3 µm which is attributed to the piezoelectric creep.

9.4 Conclusions

We have demonstrated a two dimensional alignment system, based on bimorph piezoelectric bending actuators. The piezo system is capable of optimizing the optical coupling efficiency between a 2 μm wide InP waveguide and a lensed optical fiber by tuning the voltage applied to the two individual piezo actuators. A coupling efficiency of -2.1 dB has been achieved across a misalignment window of 100 μm^2 through piezo compensation. A bias voltage of 12.5 V with a tuning range of the order of 5.8 V are sufficient to achieve misalignment compensation with sub-microwatt electrical power consumption. A 1 hour long automatically controlled compensation experiment has been performed to show the potential of the piezo assembly in a relatively long time operation. Optimal optical power transmission has been retained during the experiment by means of an automatic control based on the *hill climbing* algorithm.

10 Appendix-The fabrication process flow[7]

10.1 Introduction

Fabrication of the PICs reported in this thesis has been performed either through the MPW service [85] offered by the foundry SMART Photonics or through a custom process flow. SMART Photonics provides the possibility of using a generic integration oriented [123] process flow to obtain a number of fabricated optical chips for a convenient cost. Generic integration enables the use of pre-defined building blocks to assemble more complex photonic circuits, however, the flexibility in design aspects such as I/O facet geometry, etching profiles and cell footprint is limited by the foundry rules and a custom fabrication might be needed to develop advanced structures. The integration of etched facets and wet etched scribe marks (see chapter 7) with the standard optical elements opens possibilities for realizing complex PICs in combination with on chip collimation, on chip enhanced beam steering (see chapter 6) and accurate singulation. In this chapter we describe the custom fabrication process employed in this work, standard process steps are presented together with the details of the added custom steps.

10.2 Process flow

The process flow employed for this thesis is inspired to the COBRA flow developed by the Eindhoven University of Technology. This process flow enables the fabrication of basic optical elements which are schematically shown in Figure 1-1. These basic optical components can be fabricated through a set of standard fundamental fabrication steps: active/passive integration, waveguides definition, passivation, metallization and singulation. Two extra steps are added to the standard COBRA flow to achieve the work in this thesis: deep I/O facet etching and wet etching of the scribe marks for accurate singulation.

[7] The fabrication has been performed by Simone Cardarelli.

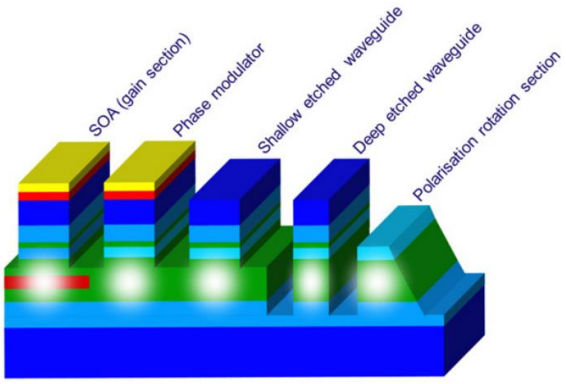

Figure 10-1. Schematic representation of the basic optical elements which can be fabricated through the COBRA process flow. Figure from [123].

10.2.1 Active/passive integration

The active/passive integration is a step performed to provide commercially available passive InP wafers with both passive and active guiding layer stacks. A first growth of lattice matched InGaAsP is performed on the InP wafer to provide passive guiding properties. The active regions are fabricated by etching areas of passive guiding layer and by re-growing active material. A final regrowth is performed to provide the wafer with a top cladding and contact layer. The active/passive integration has been performed on a three-inch InP wafer and the schematic steps are shown in Figure 10-2.

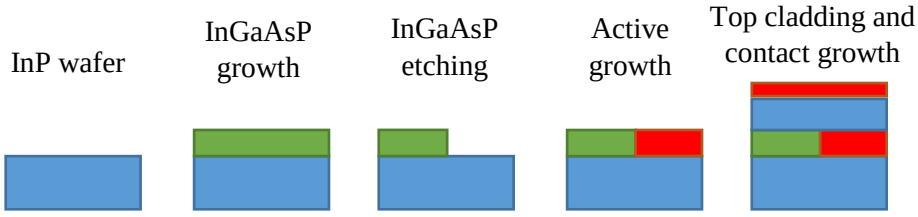

Figure 10-2. Schematic steps for the passive/active integration on an InP wafer.

The final functional layer stack used in this thesis is composed by a 250 nm thick contact layer, a 1300 nm thick InP top cladding, a 500 nm thick InGaAsP guiding layer and by the 600 µm thick InP substrate.

10.2.2 Waveguides definition

The definition of the optical waveguides is performed through a sequence of dry etching steps, by using a thick SiN mask. An 800 nm thick SiN layer is deposited and patterned in the initial stage of the process flow for the waveguide mask definition. Optical waveguides with multiple functions have been fabricated: shallow etched waveguides, deep etched waveguides and electrically isolated waveguides. Shallow etched waveguides present confinement trenches which are etched up to 100 nm into the guiding layer. These waveguides present low scattering losses and are commonly used for phase modulation and SOAs. Deep etched waveguides present trenches etched up to 200 nm into the bottom cladding, providing high confinement propagation. Low radius bends can be implemented with such waveguides. The top cladding of electrically isolated waveguides is etched up to 400 nm from the guiding layer in order to achieve sufficient electrical isolation between the optical components connected through the same waveguide.

10.2.3 Passivation

After the definition of the waveguides, the waveguide walls are protected through polyimide. A second function of the polyimide is to achieve planarization of the top surface of the processed wafer, in order to promote the correct fabrication of the metal tracks. A polyimide layer with thickness of the order of 1 μm has been spun on the processed wafer.

10.2.4 Metallization

Electrical excitation of phase modulators and SOAs is possible by contacting the contact layers thorough electrodes. Electrodes have been fabricated with a two-step process: lift-off and electro-plating. Lift-off is first performed in order to achieve good contact quality. Titanium, platinum and gold have been evaporated for the lift-off process. A thickness of the order of 375 nm is achieved with the first metallization. The electro-plating step is then performed to increase the thickness of the electrode up to 2 μm. Such a step is important to achieve low resistance electrical connections and reliable pads for wire bonding.

10.2.5 Etched facets

The fabrication of deep etched facets is the first custom step introduced in the COBRA flow. Etched facets characterized by an etch step of 5 μm are defined with

one etching step by using $Cl_2/H_2/Ar$ based dry etching chemistry. The deep etched facets might affect subsequent critical photolithography steps, and for this reason are fabricated after the waveguides definition and the metallization. A double masking process is performed for the etching of the etched facets. The mask for the etched facets is the same used for the waveguide definition in order to achieve perfect alignment between waveguides and I/O terminations. The SiN mask related to the facets is protected during the waveguide definition in order to retain sufficient thickness of the mask. Two layers of polyimide are spun, exposed and developed as a protection for the part of the wafer which is not meant to be etched during the facet etching step. The double masking strategy is shown in Figure 10-3.

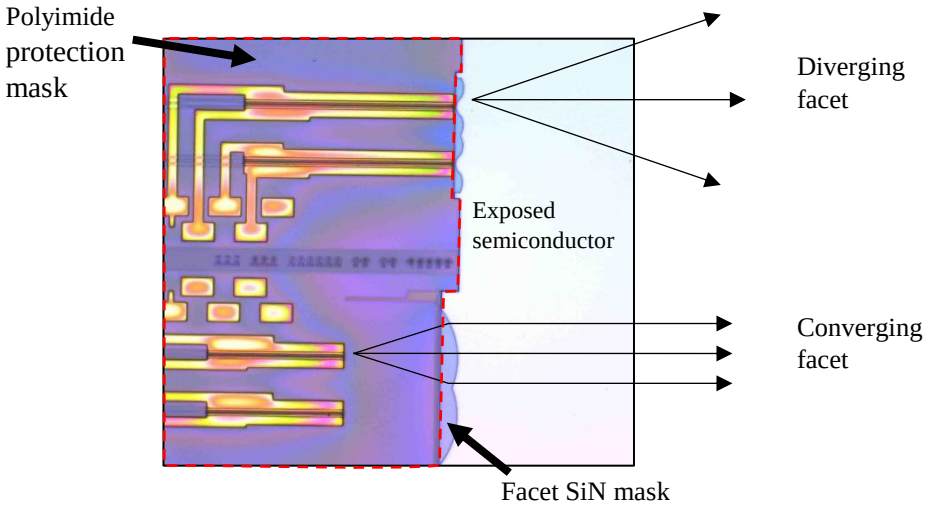

Figure 10-3. Optical microscope photo of a portion of a chip before the facet etching step.

The polyimide protection mask is the uninform purple layer inside the dashed red line. The curved light blue mask is the facet SiN mask. The lightest area is the exposed semiconductor to be etched. Both diverging and converging etched facets are present in Figure 10-3.

The wafers have been rinsed 10 minutes in the water after the facet etching, in order to avoid post processing reactions between chlorine residues and air. Such a reaction might generate HCl which is an etchant for the InP and facet damaging may occur. Etched facets are only defined for one side of the designed cells, whereas the I/O ports on the remaining side are defined through cleaving. The design for the etched facets mask is shown in Figure 10-4.

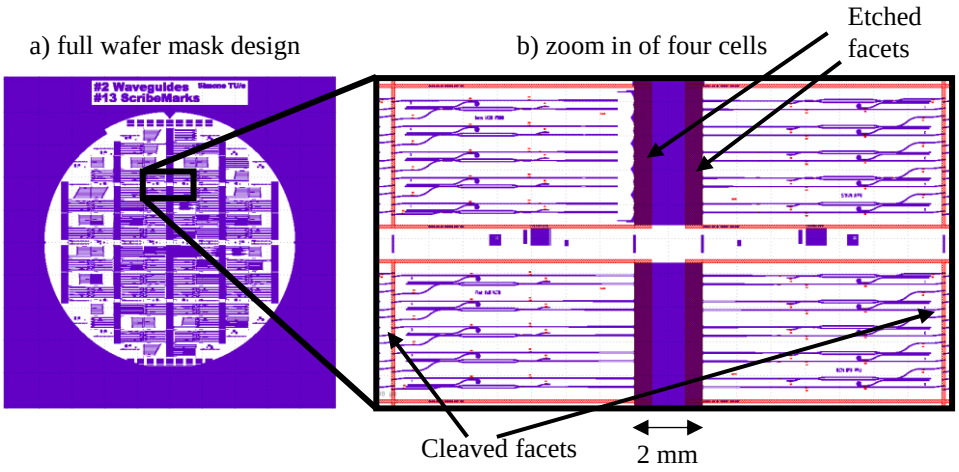

Figure 10-4. a) full mask design for the etched facets definition and b) zoom in of a portion of the full mask, contain four cells.

Figure 10-4a shows the full mask design used for the definition of the etched facets. A portion of Figure 10-4a is magnified to show how cells are arranged. Figure 10-4b shows a set of four cells 7 mm × 4 mm. A 2 mm wide separation area is designed between the etched facets. The purpose of such a wide separation area is to provide the possibilities for both precision cleaving (see chapter 7) and "scribe and break" technique. In case accurate cleaving is not necessary "scribe and break" can be applied to the left and right side of the separation area in order to achieve singulation.

10.2.6 Wet etched scribe marks

The fabrication of wet etched scribe marks is the final processing stage of our process flow. Wet etched scribe marks are also fabricated by using a double masking process. The mask for the scribe mark is defined by the InGaAsP layer whereas the rest of the wafer is protected through a hard baked 7 µm thick AZ resist. The full wafer is immerged in a $HCl:H_3PO_4$ solution for 10 minutes to achieve wet etching of the scribe marks. The wafer is etched in a vertical position to avoid that the large quantity of gas generated during the process accumulates beneath the wafer. This may cause unwanted wafer movements which may damage the sample. The back side of the wafer is unprotected during this step, however, only a layer thickness of the order of 60 µm is removed from the back. Back side grinding up to 250 µm and polishing have been finally performed by SMART Photonics to thin the wafer and to

achieve a smooth back side surface. Back side metallization has been also performed by SMART Photonics.

10.2.7 Singulation

The singulation step is performed as a combination of coarse cleaving steps and accurate cleaving steps. An example for chip singulation is schematically shown in Figure 10-5. Black solid arrows represent cleaving lines generated from a scribe mark made thorough a diamond tip, whereas the dashed arrows represent cleaving lines originating from the wet etched scribe marks. During the step a), three coarse cleaving lines are generated through “scribe and break” in order to obtain a quarter of wafer. A 2 cells wide and 4 cells long horizontal bar is obtained through the step b) with “scribe and break”. The horizontal bar is cleaved along the etched facets through the wet etched scribe marks as shown in the step c), in order to obtain 2 × 2 cells sections. Two horizontal bars are separated in step d) with “scribe and break”, however, the breaking force is for this time applied to the back of the chip. The single chips of the bars separated with the scribe line number 9 are separated through the precision cleaving number 10.

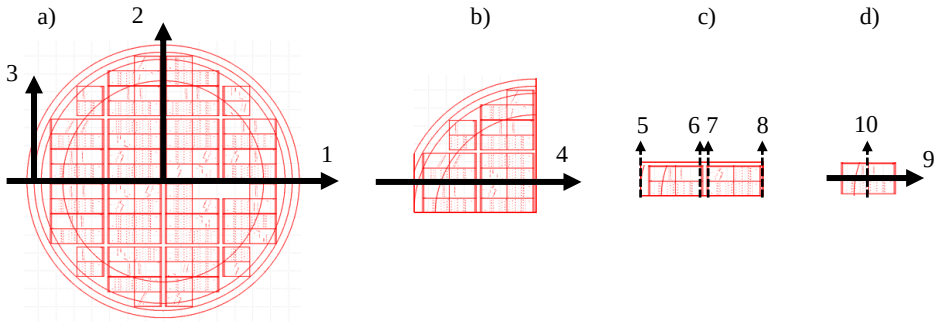

Figure 10-5. Schematic steps for the singulation procedure.

Bibliography

[1] C. V. Poulton *et al.*, "High-Performance Integrated Optical Phased Arrays for Chip-Scale Beam Steering and LiDAR," in *Conference on Lasers and Electro-Optics*, 2018, p. ATu3R.2.

[2] M. Mansouree, L. Yousefi, and M. K. Esfahani, "Optical Beam Steering for Bio-sensing Application," in *Asia Communications and Photonics Conference 2016*, 2016, p. ATh3K.4.

[3] B. Muralikrishnan, S. Phillips, and D. Sawyer, "Laser trackers for large-scale dimensional metrology: A review," *Precis. Eng.*, vol. 44, pp. 13–28, Apr. 2016.

[4] V.-F. Duma, J. P. Rolland, and A. G. Podoleanu, "Perspectives of optical scanning in OCT," 2010, vol. 7556, p. 75560B.

[5] C. W. Oh, E. Tangdiongga, and A. M. J. Koonen, "Steerable pencil beams for multi-Gbps indoor optical wireless communication," *Opt. Lett.*, vol. 39, no. 18, p. 5427, Sep. 2014.

[6] G. F. Marshall, *Laser beam scanning : opto-mechanical devices, systems, and data storage optics*. Marcel Dekker, 1985.

[7] T. K. Chan *et al.*, "Optical beamsteering using an 8 × 8 MEMS phased array with closed-loop interferometric phase control," *Opt. Express*, vol. 21, no. 3, p. 2807, Feb. 2013.

[8] M. Zohrabi, R. H. Cormack, and J. T. Gopinath, "Wide-angle nonmechanical beam steering using liquid lenses," *Opt. Express*, vol. 24, no. 21, p. 23798, Oct. 2016.

[9] A. Yaacobi, J. Sun, M. Moresco, G. Leake, D. Coolbaugh, and M. R. Watts, "Integrated phased array for wide-angle beam steering," *Opt. Lett.*, vol. 39, no. 15, p. 4575, Aug. 2014.

[10] Weihua Guo *et al.*, "Two-Dimensional Optical Beam Steering With InP-Based Photonic Integrated Circuits," *IEEE J. Sel. Top. Quantum Electron.*, vol. 19, no. 4, pp. 6100212–6100212, Jul. 2013.

[11] M. Jarrahi, R. F. W. Pease, D. A. B. Miller, and T. H. Lee, "Optical switching based on high-speed phased array optical beam steering," *Appl. Phys. Lett.*, vol. 92, no. 1, p. 014106, Jan. 2008.

[12] T. Tekin, "Review of Packaging of Optoelectronic, Photonic, and MEMS Components," *IEEE J. Sel. Top. Quantum Electron.*, vol. 17, no. 3, pp. 704–719, May 2011.

[13] J. H. C. van Zantvoort, F. M. Huijskens, G. P. Herben, and H. de Waardt, "Fiber-array pigtailing and packaging of an InP-based optical cross-connect chip," *IEEE J. Sel. Top. Quantum Electron.*, vol. 5, no. 5, pp. 1255–1259, 1999.

[14] T. Barwicz *et al.*, "Automated, high-throughput photonic packaging," *Opt.*

Fiber Technol., vol. 44, pp. 24–35, Aug. 2018.
[15] M. Liehr, “AIM Photonics – Manufacturing Challenges for Photonic Integrated Circuits,” in *Frontiers in Optics 2016*, 2016, p. FF1E.1.
[16] R. Y. Fang *et al.*, “1.55-μm InGaAsP-InP spot-size-converted (SSC) laser with simple technological process,” *IEEE Photonics Technol. Lett.*, vol. 10, no. 6, pp. 775–777, Jun. 1998.
[17] J. C. C. Lo and S. W. R. Lee, “Experimental assessment of passive alignment of optical fibers with V-grooves on silicon optical bench,” in *Proceedings of 6th Electronics Packaging Technology Conference (EPTC 2004) (IEEE Cat. No.04EX971)*, pp. 375–380.
[18] C. Kallmayer, H. Oppermann, G. Eugelmann, E. Zakel, and H. Reichl, “Self-aligning flip-chip assembly using eutectic gold/tin solder in different atmospheres,” in *Nineteenth IEEE/CPMT International Electronics Manufacturing Technology Symposium*, pp. 18–25.
[19] R. A. Boudreau, S. M. Boudreau, and S. M. Boudreau, *Passive Micro-Optical Alignment Methods*, vol. 98. CRC Press, 2005.
[20] J. V. Galan *et al.*, “CMOS compatible silicon etched V-grooves integrated with a SOI fiber coupling technique for enhancing fiber-to-chip alignment,” in *2009 6th IEEE International Conference on Group IV Photonics*, 2009, pp. 148–150.
[21] R. Klockenbrink, E. Peiner, H. -H. Wehmann, and A. Schlachetzki, “Wet Chemical Etching of Alignment V-Grooves in (100) InP through Titanium or In[sub 0.53]Ga[sub 0.47]As Masks,” *J. Electrochem. Soc.*, vol. 141, no. 6, p. 1594, Jun. 1994.
[22] D. Karnick, N. Bauditsch, L. Eisenblatter, T. Kuhner, M. Schneider, and M. Weber, “Efficient, Easy-to-Use, Planar Fiber-to-Chip Coupling Process with Angle-Polished Fibers,” in *2017 IEEE 67th Electronic Components and Technology Conference (ECTC)*, 2017, pp. 1627–1632.
[23] “High Precision V-Groove in Silicon and Glass Chip.” [Online]. Available: http://www.o-eland.com/passive/FiberArray/vgroove.htm. [Accessed: 03-Mar-2019].
[24] T. Alder, R. Heinzelmann, S. Leonhard, A. Stohr, and D. Jager, “Fiber-chip-coupling based on in InP V-groove technology,” in *Conference Proceedings. LEOS’98. 11th Annual Meeting. IEEE Lasers and Electro-Optics Society 1998 Annual Meeting (Cat. No.98CH36243)*, vol. 1, pp. 40–41.
[25] R. Hauffe, U. Siebel, K. Petermann, R. Moosburger, J.-R. Kropp, and F. Arndt, “Methods for passive fiber chip coupling of integrated optical devices,” in *2000 Proceedings. 50th Electronic Components and Technology Conference (Cat. No.00CH37070)*, pp. 238–243.
[26] Yu-Cheng Tsao, Jing-Jou Tang, and Ya-Ling Hsieh, “Analysis of probing effects on solder bump,” in *Proceedings of 6th Electronics Packaging Technology Conference (EPTC 2004) (IEEE Cat. No.04EX971)*, pp. 303–

307.
[27] J. Salonen and J. Salmi, “A flip chip process based on electroplated solder bumps,” *Phys. Scr.*, vol. T54, no. T54, pp. 230–233, Jan. 1994.
[28] C. Li, “Silicon-based opto-electronic integration for high bandwidth density optical interconnects.” 27-Jun-2018.
[29] M. Wale and M. Goodwin, “Flip-chip bonding optimizes opto-ICs,” *IEEE Circuits Devices Mag.*, vol. 8, no. 6, pp. 25–31, Nov. 1992.
[30] D. D’Agostino, E. Kleijn, R. Santos, H. P. M. M. Ambrosius, and M. K. Smit, “A dense spot size converter array fabricated in a generic process on InP,” 2013, vol. 8767, p. 87670Q.
[31] M. J. Picard, Y. Painchaud, C. Latrasse, C. Larouche, F. Pelletier, and M. Poulin, “Novel spot-size converter for optical fiber to sub-μm silicon waveguide coupling with low loss, low wavelength dependence and high tolerance to alignment,” in *European Conference on Optical Communication, ECOC*, 2015, vol. 2015–Novem, pp. 1–3.
[32] J. Fernandez Herrera and H. E. Hernandez-Figueroa, “Coupling experience between conical micro-lenses fiber and SOI photonic chip,” in *Latin America Optics and Photonics Conference*, 2016, p. LTu4A.31.
[33] P. Karioja, J. Ollila, V.-P. Putila, K. Keranen, J. Hakkila, and H. Kopola, “Comparison of active and passive fiber alignment techniques for multimode laser pigtailing,” in *2000 Proceedings. 50th Electronic Components and Technology Conference (Cat. No.00CH37070)*, pp. 244–249.
[34] C. Errando-Herranz, M. Colangelo, S. Ahmed, J. Bjork, and K. B. Gylfason, “MEMS tunable silicon photonic grating coupler for post-assembly optimization of fiber-to-chip coupling,” in *2017 IEEE 30th International Conference on Micro Electro Mechanical Systems (MEMS)*, 2017, pp. 293–296.
[35] “Active alignment system for laser to fiber coupling,” Oct. 1992.
[36] T.-J. Peters and M. Tichem, “Mechanically flexible waveguide arrays for optical chip-to-chip coupling,” 2016, vol. 9760, p. 97600D.
[37] Yilong Hao and Dacheng Zhang, “Silicon-based MEMS process and standardization,” in *Proceedings. 7th International Conference on Solid-State and Integrated Circuits Technology, 2004.*, vol. 3, pp. 1835–1838.
[38] S. Yang and Q. Xu, “A review on actuation and sensing techniques for MEMS-based microgrippers,” *J. Micro-Bio Robot.*, vol. 13, no. 1–4, pp. 1–14, Oct. 2017.
[39] O. Degani *et al.*, “Pull-in study of an electrostatic torsion microactuator,” *J. Microelectromechanical Syst.*, vol. 7, no. 4, pp. 373–379, 1998.
[40] S. Trolier-McKinstry and P. Muralt, “Thin Film Piezoelectrics for MEMS,” *J. Electroceramics*, vol. 12, no. 1/2, pp. 7–17, Jan. 2004.
[41] B. Sheeparamatti, P. Hanasi, and V. Abbigeri, “Critical analysis of different actuation techniques for a micro cantilever,” *waset.org*.

[42] T. G. King, M. E. Preston, B. J. M. Murphy, and D. S. Cannell, “Piezoelectric ceramic actuators: A review of machinery applications,” *Precis. Eng.*, vol. 12, no. 3, pp. 131–136, Jul. 1990.
[43] S. Cardarelli, N. Calabretta, R. Stabile, K. Williams, X. Luo, and J. Mink, “Wide-Range 2D InP Chip-to-Fiber Alignment Through Bimorph Piezoelectric Actuators,” in *2018 IEEE 68th Electronic Components and Technology Conference (ECTC)*, 2018, pp. 1124–1129.
[44] M. Bale and R. E. Palmer, “Deep plasma etching of piezoelectric PZT with SF[sub 6],” *J. Vac. Sci. Technol. B Microelectron. Nanom. Struct.*, vol. 19, no. 6, p. 2020, Dec. 2001.
[45] W. König and E. Verlemann, “Machining Advanced Ceramics — A Challenge in Production Technology,” in *Designing with Structural Ceramics*, Dordrecht: Springer Netherlands, 1991, pp. 187–200.
[46] S. Cardarelli, N. Calabretta, R. Stabile, K. Williams, X. Luo, and J. Mink, “Wide-Range 2D InP Chip-to-Fiber Alignment Through Bimorph Piezoelectric Actuators,” in *2018 IEEE 68th Electronic Components and Technology Conference (ECTC)*, 2018, pp. 1124–1129.
[47] Xiaohua Ma and Geng-Sheng Kuo, “Optical switching technology comparison: optical mems vs. other technologies,” *IEEE Commun. Mag.*, vol. 41, no. 11, pp. 50–57, Nov. 2003.
[48] V. A. Aksyuk *et al.*, “Beam-steering micromirrors for large optical cross-connects,” *J. Light. Technol.*, vol. 21, no. 3, pp. 634–642, Mar. 2003.
[49] C. W. Oh, Z. Cao, E. Tangdiongga, and T. Koonen, “Free-space transmission with passive 2D beam steering for multi-gigabit-per-second per-beam indoor optical wireless networks,” *Opt. Express*, vol. 24, no. 17, p. 19211, Aug. 2016.
[50] T.-H. Chao, H. Zhou, G. F. Reyes, D. Dragoi, and J. Hanan, “High-speed high-density holographic memory using electro-optic beam steering devices,” 2002, vol. 4803, p. 70.
[51] J.-H. Park and I. C. Khoo, “Liquid-crystal beam steering device with a photopolymer prism,” *Appl. Phys. Lett.*, vol. 87, no. 9, p. 091110, Aug. 2005.
[52] Jie Sun, R. A. Ramsey, Yuan Chen, and Shin-Tson Wu, “Submillisecond-Response Sheared Polymer Network Liquid Crystals for Display Applications,” *J. Disp. Technol.*, vol. 8, no. 2, pp. 87–90, Feb. 2012.
[53] Xinghua Wang, Bin Wang, P. J. Bos, J. E. Anderson, and P. F. McManamon, “2-D liquid crystal optical phased array,” in *2004 IEEE Aerospace Conference Proceedings (IEEE Cat. No.04TH8720)*, vol. 2, pp. 905–913.
[54] J. Kim, C. Oh, M. J. Escuti, L. Hosting, and S. Serati, “Wide-angle nonmechanical beam steering using thin liquid crystal polarization gratings,” 2008, p. 709302.
[55] J. Ptasinski, S. W. Kim, L. Pang, I.-C. Khoo, and Y. Fainman, “Optical tuning of silicon photonic structures with nematic liquid crystal claddings,”

Opt. Lett., vol. 38, no. 12, p. 2008, Jun. 2013.
[56] J. Martz *et al.*, "Liquid crystal infiltration of InP-based planar photonic crystals," *J. Appl. Phys.*, vol. 99, no. 10, p. 103105, May 2006.
[57] "InP-based planar photonic crystals:process development, characterization and infiltration | Request PDF." [Online]. Available: https://www.researchgate.net/publication/254882361_InP-based_planar_photonic_crystalsprocess_development_characterization_and_infiltration. [Accessed: 18-Mar-2019].
[58] Xuesong Dong, P. LiKamWa, J. Loehr, and R. Kaspi, "Current-induced guiding and beam steering in active semiconductor planar waveguide," *IEEE Photonics Technol. Lett.*, vol. 11, no. 7, pp. 809–811, Jul. 1999.
[59] D. A. May-Arrioja, N. Bickel, and P. LiKamWa, "Optical beam steering using InGaAsP multiple quantum wells," *IEEE Photonics Technol. Lett.*, vol. 17, no. 2, pp. 333–335, Feb. 2005.
[60] G. A. Fish, L. A. Coldren, and S. P. DenBaars, "Compact InGaAsP/InP 1×2 optical switch based on carrier induced supression of modal interference," *Electron. Lett.*, vol. 33, no. 22, p. 1898, 1997.
[61] M. W. Pruessner, T. T. King, D. P. Kelly, R. Grover, L. C. Calhoun, and R. Ghodssi, "Mechanical property measurement of InP-based MEMS for optical communications," *Sensors Actuators A Phys.*, vol. 105, no. 2, pp. 190–200, Jul. 2003.
[62] W. H. Ng *et al.*, "Design and Fabrication of Suspended Indium Phosphide Waveguides for MEMS-Actuated Optical Buffering," *IEEE J. Sel. Top. Quantum Electron.*, vol. 21, no. 4, pp. 240–246, Jul. 2015.
[63] A. Yariv, P. Yeh, and A. Yariv, *Photonics : optical electronics in modern communications*. .
[64] C. Kittel, *Introduction to solid state physics*. Wiley, 2005.
[65] "InPACT - The Indium Phosphide substrates (InP) Specialist." [Online]. Available: http://www.inpactsemicon.com/p_process.php. [Accessed: 03-Mar-2019].
[66] H. G. Bach, J. Krauser, H. P. Nolting, R. A. Logan, and F. K. Reinhart, "Electro-optical light modulation in InGaAsP/InP double heterostructure diodes," *Appl. Phys. Lett.*, vol. 42, no. 8, pp. 692–694, Apr. 1983.
[67] S. Adachi and John Wiley & Sons., *Physical properties of III-V semiconductor compounds : InP, InAs, GaAs, GaP, InGaAs, and InGaAsP*. Wiley, 1992.
[68] J. Faist and F. -K. Reinhart, "Phase modulation in GaAs/AlGaAs double heterostructures. I. Theory," *J. Appl. Phys.*, vol. 67, no. 11, pp. 6998–7005, Jun. 1990.
[69] G. Hagn, "Electro-optic effects and their application in indium phosphide waveguide devices for fibre optic access networks." ETH. Zürich, 2002.
[70] B. R. Bennett, R. A. Soref, and J. A. Del Alamo, "Carrier-induced change in

refractive index of InP, GaAs and InGaAsP," *IEEE J. Quantum Electron.*, vol. 26, no. 1, pp. 113–122, 1990.

[71] J. Vinchant, J. Cavailles, … M. E.-J. of lightwave, and undefined 1992, "InP/GaInAsP guided-wave phase modulators based on carrier-induced effects: Theory and experiment," *ieeexplore.ieee.org*.

[72] F. Fiedler and A. Schlachetzki, "Optical parameters of InP-based waveguides," *Solid. State. Electron.*, vol. 30, no. 1, pp. 73–83, Jan. 1987.

[73] J.-P. Weber, "Optimization of the carrier-induced effective index change in InGaAsP waveguides-application to tunable Bragg filters," *IEEE J. Quantum Electron.*, vol. 30, no. 8, pp. 1801–1816, 1994.

[74] C. Henry, R. Logan, F. Merritt, and J. Luongo, "The effect of intervalence band absorption on the thermal behavior of InGaAsP lasers," *IEEE J. Quantum Electron.*, vol. 19, no. 6, pp. 947–952, Jun. 1983.

[75] W. Walukiewicz *et al.*, "Electron mobility and free-carrier absorption in InP; determination of the compensation ratio," *J. Appl. Phys.*, vol. 51, no. 5, p. 2659, Jul. 1980.

[76] S. L. Chuang, *Physics of optoelectronic devices*. Wiley, 1995.

[77] R. E. Nahory, M. A. Pollack, W. D. Johnston, and R. L. Barns, "Band gap versus composition and demonstration of Vegard's law for $In_{1-x}Ga_xAs_yP_{1-y}$ lattice matched to InP," *Appl. Phys. Lett.*, vol. 33, no. 7, pp. 659–661, Oct. 1978.

[78] F. M. (Francisco M. . Fernández, *Introduction to perturbation theory in quantum mechanics*. CRC Press, 2001.

[79] F. M. De Paola, V. d'Alessandro, A. Irace, J. H. den Besten, and M. K. Smit, "Novel optoelectronic simulation strategy of an ultra-fast InP/InGaAsP modulator," *Opt. Commun.*, vol. 256, no. 4–6, pp. 326–332, Dec. 2005.

[80] X. Zhao, B. Xiong, C. Sun, and Y. Luo, "Low drive voltage optical phase modulator with novel InGaAlAs/InAlAs multiple-quantum-barrier based n-i-n heterostructure," *Opt. Express*, vol. 21, no. 21, p. 24894, Oct. 2013.

[81] J. Decobert, D. Herrati, V. Colson, D. Leclerc, and L. Goldstein, "Growth and characterization of Si, S and Zn-doped InP in selective area growth conditions," *J. Cryst. Growth*, vol. 248, pp. 390–394, Feb. 2003.

[82] S. Mukai, M. Watanabe, H. Itoh, H. Yajima, Y. Hosoi, and S. Uekusa, "Beam scanning and switching characteristics of twin-striped lasers with a reduced stripe spacing," *Opt. Quantum Electron.*, vol. 17, no. 6, pp. 431–434, 1985.

[83] L. B. Soldano and E. C. M. Pennings, "Optical multi-mode interference devices based on self-imaging: principles and applications," *J. Light. Technol.*, vol. 13, no. 4, pp. 615–627, Apr. 1995.

[84] J. Leuthold, R. Hess, J. Eckner, P. A. Besse, and H. Melchior, "Spatial mode filters realized with multimode interference couplers," *Opt. Lett.*, vol. 21, no. 11, p. 836, Jun. 1996.

[85] “JePPIX.” [Online]. Available: http://www.jeppix.eu/multiprojectwafers-1. [Accessed: 10-Jul-2018].
[86] D. D’Agostino, D. Lenstra, H. P. M. M. Ambrosius, and M. K. Smit, “Coupled cavity laser based on anti-resonant imaging via multimode interference,” *Opt. Lett.*, vol. 40, no. 4, p. 653, Feb. 2015.
[87] C. Kachris, K. Kanonakis, and I. Tomkos, “Optical interconnection networks in data centers: recent trends and future challenges,” *IEEE Commun. Mag.*, vol. 51, no. 9, pp. 39–45, Sep. 2013.
[88] R. A. Steinberg, T. G. Giallorenzi, and R. G. Priest, “Polarization-insensitive integrated-optical switches: a new electrode design,” *Appl. Opt.*, vol. 16, no. 8, p. 2166, Aug. 1977.
[89] M. Renaud, M. Bachmann, and M. Erman, “Semiconductor optical space switches,” *IEEE J. Sel. Top. Quantum Electron.*, vol. 2, no. 2, pp. 277–288, Jun. 1996.
[90] F. Testa and L. Pavesi, *Optical switching in next generation data centers*. .
[91] Q. Cheng, S. Rumley, M. Bahadori, and K. Bergman, “Photonic switching in high performance datacenters [Invited],” *Opt. Express*, vol. 26, no. 12, p. 16022, Jun. 2018.
[92] B. C. Qiu *et al.*, “Monolithic fabrication of 2 /spl times/ 2 crosspoint switches in InGaAs-InAlGaAs multiple quantum wells using quantum-well intermixing,” *IEEE Photonics Technol. Lett.*, vol. 13, no. 12, pp. 1292–1294, Dec. 2001.
[93] K. A. Williams, “Integrated semiconductor-optical-amplifier-based switch fabrics for high-capacity interconnects [Invited],” *J. Opt. Netw.*, vol. 6, no. 2, p. 189, Feb. 2007.
[94] H. Wang, X. Li, Q. Zhou, L. Ge, X. Jiang, and J. Yang, “LiNbO3 Based 1×2 Y-Branch Digital Optical Switch Integrated with S-Bend Variable Optical Attenuator,” in *2010 Symposium on Photonics and Optoelectronics*, 2010, pp. 1–4.
[95] “IMPROVED FABRICATION OF 4X4 POLARISATION INSENSITIVE SWITCH MATRICES ON INP BY INTRODUCTION OF AN ETCH STOP LAYER - Bell Labs.” [Online]. Available: http://bell-labs.com/our-research/publications/285315/. [Accessed: 06-Jul-2018].
[96] K. Komatsu, K. Hamamoto, M. Sugimoto, A. Ajisawa, Y. Kohga, and A. Suzuki, “4*4 GaAs/AlGaAs optical matrix switches with uniform device characteristics using alternating Delta beta electrooptic guided-wave directional couplers,” *J. Light. Technol.*, vol. 9, no. 7, pp. 871–878, Jul. 1991.
[97] R. Krahenbuhl *et al.*, “Low-loss polarization-insensitive InP-InGaAsP optical space switches for fiber optical communication,” *IEEE Photonics Technol. Lett.*, vol. 8, no. 5, pp. 632–634, May 1996.
[98] D. H. P. Maat, “InP-based Integrated MZI Switches for Optical Communication.” 2001.

[99] J. S. Parker, E. J. Norberg, R. S. Guzzon, S. C. Nicholes, and L. A. Coldren, “High verticality InP/InGaAsP etching in Cl2/H2/Ar inductively coupled plasma for photonic integrated circuits,” *J. Vac. Sci. Technol. B, Nanotechnol. Microelectron. Mater. Process. Meas. Phenom.*, vol. 29, no. 1, p. 011016, Jan. 2011.

[100] W. Yao, “Towards a high-capacity multi-channel transmitter in generic photonic integration technology.” 12-Jan-2017.

[101] M. N. Sysak, L. A. Johansson, J. W. Raring, M. Rodwell, L. A. Coldren, and J. Bowers, “A High efficiency, Current Injection Based Quantum-Well Phase Modulator Monolithically Integrated with a Tunable Laser for Coherent Systems,” in *Optical Amplifiers and Their Applications/Coherent Optical Technologies and Applications*, 2006, p. CFC6.

[102] E. Suhir, “Thermal Stress Failures in Electronics and Photonics: Physics, Modeling, Prevention,” *J. Therm. Stress.*, vol. 36, no. 6, pp. 537–563, Jun. 2013.

[103] L. Zimmermann, G. B. Preve, T. Tekin, T. Rosin, and K. Landles, “Packaging and Assembly for Integrated Photonics—A Review of the ePIXpack Photonics Packaging Platform,” *IEEE J. Sel. Top. Quantum Electron.*, vol. 17, no. 3, pp. 645–651, May 2011.

[104] T. Hirata, M. Suehiro, M. Hihara, M. Dobashi, and H. Hosomatsu, “Demonstration of a waveguide lens monolithically integrated with a laser diode by compositional disordering of a quantum well,” *IEEE Photonics Technol. Lett.*, vol. 5, no. 6, pp. 698–700, Jun. 1993.

[105] A. M. Rashed, K. A. Williams, P. J. Heard, R. V. Penty, and I. H. White, “Tapered waveguide with parabolic lens: theory and experiment,” *Opt. Eng.*, vol. 42, no. 3, p. 792, Mar. 2003.

[106] S.-Y. Jung, S. Hann, and C.-S. Park, “TDOA-based optical wireless indoor localization using LED ceiling lamps,” *IEEE Trans. Consum. Electron.*, vol. 57, no. 4, pp. 1592–1597, Nov. 2011.

[107] A. Yariv and A. Yariv, *Optical electronics in modern communications*. Oxford University Press, 1997.

[108] Lord Rayleigh, “Investigations in optics, with special reference to the spectroscope,” *London, Edinburgh, Dublin Philos. Mag. J. Sci.*, vol. 8, no. 49, pp. 261–274, Oct. 1879.

[109] A. Paraskevopoulos *et al.*, “Fabrication of InGaAsP/InP ridge waveguide lasers with dry etched facets using chemically assisted ion beam etching and a simple photoresist mask,” in *LEOS 2001. 14th Annual Meeting of the IEEE Lasers and Electro-Optics Society (Cat. No.01CH37242)*, vol. 1, pp. 173–174.

[110] R. M. L. A. Dos Santos, D. D’Agostino, H. R. Haghighi, M. K. Smit, and X. J. M. Leijtens, “Fabrication and characterization of etched facets in InP for advanced packaging of Photonic Integrated circuits.” University of Twente,

pp. 107–110, 2014.
[111] J. S. Parker, E. J. Norberg, R. S. Guzzon, S. C. Nicholes, and L. A. Coldren, “High verticality InP/InGaAsP etching in Cl2/H2/Ar inductively coupled plasma for photonic integrated circuits,” *J. Vac. Sci. Technol. B, Nanotechnol. Microelectron. Mater. Process. Meas. Phenom.*, vol. 29, no. 1, p. 011016, Jan. 2011.
[112] G. J. van Gurp, J. M. Jacobs, J. J. M. Binsma, and L. F. Tiemeijer, “InGaAsP/InP Lasers with Two Reactive-Ion-Etched Mirror Facets,” *Jpn. J. Appl. Phys.*, vol. 28, no. Part 2, No. 7, pp. L1236–L1238, Jul. 1989.
[113] S. L. Rommel *et al.*, “Effect of H[sub 2] on the etch profile of InP/InGaAsP alloys in Cl[sub 2]/Ar/H[sub 2] inductively coupled plasma reactive ion etching chemistries for photonic device fabrication,” *J. Vac. Sci. Technol. B Microelectron. Nanom. Struct.*, vol. 20, no. 4, p. 1327, Aug. 2002.
[114] L. Gatilova, S. Bouchoule, S. Guilet, and P. Chabert, “Investigation of InP etching mechanisms in a Cl2/H2 inductively coupled plasma by optical emission spectroscopy,” *J. Vac. Sci. Technol. A Vacuum, Surfaces, Film.*, vol. 27, no. 2, pp. 262–275, Mar. 2009.
[115] S. Bouchoule, G. Patriarche, S. Guilet, L. Gatilova, L. Largeau, and P. Chabert, “Sidewall passivation assisted by a silicon coverplate during Cl[sub 2]–H[sub 2] and HBr inductively coupled plasma etching of InP for photonic devices,” *J. Vac. Sci. Technol. B Microelectron. Nanom. Struct.*, vol. 26, no. 2, p. 666, Apr. 2008.
[116] B. Docter, “Deeply-etched DBR mirrors for photonic integrated circuits and tunable lasers,” 2009.
[117] D. D’Agostino, “Capability extensions to the COBRA generic photonic integration platform.” 2015.
[118] M. Cooke, “Scribe and dice,” *III-Vs Rev.*, vol. 19, no. 4, pp. 20–24, May 2006.
[119] “High Accuracy Cleaving System-Electron Microscopy Sciences.” [Online]. Available: https://www.emsdiasum.com/microscopy/products/cleaving/systems.aspx. [Accessed: 06-Mar-2019].
[120] “Cleaving breakthrough: A new method removes old limitations | Request PDF.” [Online]. Available: https://www.researchgate.net/publication/288544767_Cleaving_breakthrough_A_new_method_removes_old_limitations. [Accessed: 06-Mar-2019].
[121] K. Wasmer *et al.*, “Cleavage Fracture of Brittle Semiconductors from the Nanometre to the Centimetre Scale,” *Adv. Eng. Mater.*, vol. 7, no. 5, pp. 309–317, May 2005.
[122] L. Balmer and J. Douce, “An application of hill climbing techniques in measurement,” *IEEE Trans. Automat. Contr.*, vol. 27, no. 1, pp. 89–93, Feb. 1982.

[123] M. Smit *et al.*, “An introduction to InP-based generic integration technology,” *Semicond. Sci. Technol.*, vol. 29, no. 8, p. 083001, Jun. 2014.

List of Publications

Journal publications

- **S. Cardarelli**, N. Calabretta, D. D'Agostino, R. Stabile and K. Williams, "Voltage Driven Near Field Beam Shifting in an InP Photonic Integrated Circuit", Feb 2019, In : IEEE Journal of Quantum Electronics. 55, 1, 10 p., 8584479.
- **S. Cardarelli**, N. Calabretta, R. Stabile and K. Williams, "Voltage Driven 1x2 Multimode Interference Optical Switch in InP/InGaAsP", In: IET Optoelectronics, special issue of ECIO 2018, Valencia, Spain (accepted with minor revisions).

International conferences

- **S. Cardarelli**, N. Calabretta, S. Koelling, R. Stabile and K. Williams. "Electro-Optic Device in InP for Wide Angle of Arrival Detection in Optical Wireless Communication", OFC 2019, San Diego, California.
- **S. Cardarelli**, N. Calabretta, R. Stabile, J. Mink, X. Luo and K. Williams, " Wide-range 2D InP chip-to-fiber alignment through bimorph piezoelectric actuators" , Proceedings - IEEE 68th Electronic Components and Technology Conference, ECTC 2018 (pp. 1124-1129).
- **S. Cardarelli**, N. Calabretta, R. Stabile and K. Williams, "Voltage Driven 1x2 Multimode Interference Optical Switch in InP/InGaAsP", ECIO 2018, Valencia, Spain.
- **S. Cardarelli,** N. Calabretta, D. D'Agostino, R. Stabile and K. Williams, "Beam steering device with sub micrometre precision" ,Proceedings of the European Conference on Integrated Optics 2016,Warsaw, Poland.
- D. Lenstra, W. Yao, **S. Cardarelli** and J. Mink, "Cost-effective, compact and high-speed integrable multi-mode interference modulator", Optics (Proceedings of SPIE, No. 10106), San Francisco, USA, (Feb) 2017.

Regional conferences

- **S. Cardarelli,** N. Calabretta, D. D'Agostino, R. Stabile and K. Williams, "Optical beam steering functionality of an InP/InGaAsP based optical waveguide". In G. Roelkens, N. Le Thomas & P. Bienstman (Eds.), Proceedings of the 21st Annual Symposium of the IEEE Photonics Society Benelux Chapter, November 17-18, 2016, Gent, Belgium (pp. 299-302).
- D. Lenstra, W. Yao, **S. Cardarelli** and J. Mink, "Cost-effective, compact and high-speed integrable multi-mode interference modulator", Proceedings of the 21st Annual Symposium of the IEEE Photonics Society Benelux Chapter (pp. 7-10).
- **S. Cardarelli**, N. Calabretta, S. Koelling, R. Stabile and K. Williams, "Electro-optic beam steering enhancement by etching a cylindrical facet within an InP photonic integrated circuit", 22nd Annual Symposium of the IEEE Photonics Society Benelux Chapter - Delft, Netherlands, (Nov) 2017.

Filed provisional patent

- **S. Cardarelli**, N. Calabretta, R. Stabile and K. Williams, "Etched Facets in an InP Photonic Circuit enabled through Wet Etch based Precision Cleave". Lumen Ref. No.: TUE-281/PROV, Client Ref. NO.: 2018-3300.

Acknowledgments

Just a few minutes before submitting the final version of my dissertation, I finally find the time to look back in the past, to these four years, and I feel like to spend some thoughts for the people that have been relevant to me during this fantastic staying in The Netherlands.

The first acknowledgment goes to Kevin, Nicola, and Patty … my teamwork, my family in the university. I really thank them for the effort they put to support me and guide me, from the first to the final contract day. Kevin taught me how to look at results through an objective eye, that details matter, to follow the nature hints to formulate research questions. I thank Kevin for being always so objective and focused during our discussions. I thank Nicola, that believed in me since the first day we met and helped me to apply for this project. Nicola knows when pushing and motivating at the right moments. He helped me to always keep the focus and to understand what the real research issues are and how to spot them. Thanks also for the soppressata, delicious!!!!! Thank you, Patty, for the important support. You always knew when I needed some motivation … the right energy has arrived from you really at the right moments. You deserve an extra jar of tuna.

I want to thank the whole ECO group and in particular… Ton for leading the group, for his support and for teaching me some Dutch. José, that also taught me quite a lot of Dutch ☺. She has been great during my PhD, always keeping an eye on me and on my bad bureaucracy skills. I want to thank Hugo and Chigo, my supervisors during my Master thesis project at the TU/e. I thank Oded, Franz, Johan, Henrie, Eduward. A great thanks goes to my friend Zizheng, who helped to have a nice mood in the group…thank you again for the beautiful gift you gave to me! Thanks to all the ECO PhD students in particular to my historical officemates: Jon, Netsanet, Joanne, Federico, Prometheus, Robbert … thank you for being so patient with me and our improvised Dutch lessons at lunch, thanks for teaching Ketema poker, Ketema … keep on being the positive guy you are, always smiling and willing to help … but cannot invite you playing poker anymore, dude you are too good at it. Thank you Chenhui, amazing moments in USA … good time spent in the cleanroom, looking forward to going to Universal with you again. Many thanks to Alvaro and Bin … much fun in the lab!

Still in the university but different group, I want to thank the Phi people or as I like to call them, the Pheople. I want to thank Erwin, Meint, Huub, Daan, Xavier, Yuqing, Jos … sometimes I let him win at chess, Stefanos for the shared climbing, Rastko … such as good guy, Vadim, Marc, Marija, Florian, Arezou, Dima, Perry, Victor, Xander, Manuel, Domenico, Katia (not really Phi). A special thanks goes to

Giovanni who helped me so much in the beginning … he has always been very kind to me. Un grande ringraziamento al mio piccolo gioiello di Phi, Valeria, un cuoricino pieno di panna montata!!! Grazie di tutto, delle risate, dei momenti down condivisi, del clearnroom time, dei gin, del sushi, di essere cosí forte e solare. Congratulazioni ancora per il tuo recentemente guadagnato PhD.

There is also a team of heroes to mention, the nanonab guys! A fundamental thanks to Barry … a sweet guy who knows a lot about chemistry, music and cultures, I have learnt a lot from him. Thank you Robbert for being so polite, it was nice to share some Metal music with you… in the cleanroom you were so confident to fix every issue, congrats. Thanks to Erik-Jan, Tjibbe, Jeroen … you will get back your three inch holder one day. Thank you Nando, for letting us always feel safe 😊.

A big thanks also goes to the SMART Photonics guys… Luc, Rui, Alfonso, Jeroen and of course to the amazing CR friends Ton, Jos, Jordi, Franz, Marcel, Josin and Roel, a group of hard working guy always available for discussions. We have spent good time together.

Stepping out the university, I would like to start with the football team. Thanks to Zarko, Misir, Renaud, Giuseppe, Mike, Ija, Valerio, il Biro, Daniele, Baldini, Paolo, Joel che ancora parla di randellate. Un ringraziamento speciale va al capitano Maurangelo, detto Croccangelo, per la sua decisivitá dentro e fuori dal campo. Grazie mille per la carica che hai e per avermi insegnato la famosa tecnica del “tomato method” ahahhaha, fondamentale per concludere la stesura di questa tesi ... lo consiglio vivamente.

Grazie al mio primo gruppo musicale in Olanda, Grazie a Waldo, Michele, Cesar e Davide ... é stato un sogno tornare a suonare in una band! Un grazie speciale a Michele, detto Ruoppolo, ci siamo diveriti di brutto!!! Concerti, festival, bonghi, cime di rapa, partite a calcio, discussioni scientifiche, panzerotti, gran cassa, registrazioni, i container maledetti, da Clemente, che io e Gabriele provavamo ad ascoltarlo ma dopo un pó... insomma tanti bei ricordi. Un abbraccio anche alla dolce metá di Michele, Irene, una ragazza greca che parla perfetto italiano, con un sorriso che ti riempie il cuore.

Facciamo anche un pó di pubblicitá al mio nuovo gruppo: gli strepitosi Ndujah, composti da Carmine alla chitarra solista, Luca al basso e Demetrio che ad essere sinceri é il miglior batterista della band! Grazie per ció che stiamo facendo insieme e che faremo in futuro. Ndujah for Valencia ... ip ip urrá!

Un abbraccio ai miei amici Erasmus, in particolare Marco, Valerio, Anna, Veronica e Stefano Pedroni.

Stefano Cappelli, grazie di tutto. Le arrampicate, le nottate a COD, Zurigo, le corse, sono fortunato ad aver avuto un generale come te.

Grazie a Renato e Lorenzo per le bellissime serate passate insieme e le risate.

Felix, questa la scrivo in italiano cosí studi che devi fare il cantate d'opera. Grazie per le divertenti serate, per averci regalato delle performace emozionanti, per le torte squisite che sai fare. Buona fortuna con la tua nuova challenge.

Dopo aver toccato tasti come universitá, musica e sport ... é giunto il momento di chiamare in campo i big guys ... come se fosse arrivato il momento della grande battaglia finale di *Endgame*. Un sentititissimo grazie ai miei amici di tutti i giorni, quelli che chiami anche se non hai niente da dire. Quelli che inviti a casa anche se non hai niente da fare.

Un abbraccio a Basilio e Viviana, non basterebbe un libro per descrivere l'amore che provo per loro. Indimenticabili momenti, cene, risate, divertimento ... ricordo il primo giorno che ho incontrato Basilio alla ricerca dell'avventura all'estero. Ricordo il suo primo appartamento ... che ogni tanto ritrovavo un numero sul cellulare e non sapevo fosse il suo ... ricordo le prime volte in cui piano piano la fiamma che ci lega é diventata sempre piú intensa, non provate a toccarla che brucia tantissimo ora. Basilio é una persona immensa, profonda, altruista, sognatrice!!! Continua cosí!!!! Stai andando alla grande!

Viviana, detta Scrocchiarella, l'ho incontrata per la prima volta alla Folie. Che tipa! Sempre solare, con il suo accento semi napoletano, rallegra sempre le giornate. Poi Viviana é la dea della cucina. Ma l'avete provate mai le cibarie che prepara Viviana? Roba da shuttle nello spazio, che ti guardi in dietro e pensi quanto sia bello guardare la terra da lontano! Abbiamo riscoperto il piacere di giocare a carte con Viviana ... sempre pronta a percorrere nuove strade, con in mano una valigia di tradizioni.

Un bacione a Giacomo e Claudia, il Re e la Calabrona. Anche loro hanno partecipato giorno dopo giorno a rendere unici questi quattro anni. Ora io e Giacomo proviamo a far scendere la panza, impresa non facile. Non penso sia utile andare in piscina a nuotare mezz'ora e poi tornare a case a mangiare pasta con tonno rosso e pollo al guanciale e nduja ... ma a noi piace cosí! E comunque forza Inter e abbasso Juve. Calabrona é proprio italiana, roba di lievito "paneangeli" nel cassetto, tonno alla nduja, kinder pinguí... ma dove la trova tutta questa roba? Da sligro? Non so. Avete mai visto qualcuno che porta dei calzini extra per andare a giocare a bowling in modo che non ci sia contatto tra i veri calzini e la scarpa da bowling? ... io si.

Un abbraccione a Gabrile e Mandy, Maestro e Mendozzi, respectively. Che dire, con Maestro é stato amore a prima vista. Ricordo ancora quando cantavamo le canzoni di Bertoli per le scale del Flux, che intesa! Con Gabriele si sta bene insieme, punto. Giochiamo a scacchi, alla play station, siamo stati alle isole Tremiti, Formentera, in Calabria insieme ... cioé questo soggetto mi ha invitato al matrimonio

del fratello dopo tre mesi che ci conoscevamo!! Peró non sa fare la carbonara, ci mette la cipolla, vergogna. Un bacione anche ai grandi Giuseppe, Caterina, Cataldo, Vittoria e la pupetta appena nata. Un ricordo all'immenso Gabriele, che ci ha regalato dei bellissimi momenti ... *se t'incontro per la via e ti vidu in compagnia*...

Mandyyyyy, how much you need to stand. You are great, diving into this group of Italian people without any fear…. Congrats! Thank you for the laughs we had together, talking about sushi, eyebrows, my bad English that you still find difficult to understand. Thank you for tolerating me … messy guy, changing plans with the speed of light, making a lot of nicknames!!! I hope I gave you a good reason to forgive me with those nice days we spent together in Abuzzo! Bedankt Mandy!

Giorgina, un abbraccio e un bacione anche a te. Ci siamo conosciuti la prima volta in erasmus ... poi dopo quattro anni eccoci ancora qui, a condividere avventure ed emozioni. Formentera, il sushi, teppanyaki, i trabocchi, il parco degli acquedotti, Ostia (il miglior mare di sempre), Brunori, Santo Stefano di Sessanio, la barca in Amsterdam e tanto, tanto di piú. Un mega in bocca al lupo per il tuo PhD, la tua casetta nuova e la carbonara che hai promesso a Basilio e Viviana e acora non hai fatto. Spero questa sia la buona occasione per organizzare ... ciao Gno Gno.

Tu statte carmoooooo... lo so che stai pensando che ora sia arrivato il tuo momento dei ringraziamenti... e se invece non lo fosse???? A mo non fa piú o sverdo. Ebbene si, tocca a te... Grazie Chicco! Ormai sono 10 anni che ci conosciamo, a L'Aquila insieme, erasmus insieme, PhD insieme. Qui tocca sposarsi Chicco. Troppo roba fatta insieme... qualche highlight: Call of duty a L'Aquila, zombieland, salsicciette al fioncchio, genziana, capodanno a Rieti, arrosticini in Abruzzo, Sint Jorislaan (grazie anche a Gigia e scusami ancora per la pallonata in testa), Voorterveg, Paaspop, Stratum, il biliardo, le lezioni di chitarra, Report, lo schaccino... la stampa s'incazzerá quando vedrá che il numero delle pagine lievita. Chicco un abbraccio a te e alla piccola Anke .... that still did not get the difference between cola zero and normal cola. Still need to kick her ass at badminton ahahhah!

E sdighete e sdaghete, lo spacchino Sergiño. Un abbraccio a Sergiño, il nuovo acquisto del team Eindhoven!!! Ma quanto ci mancava un soggetto come te nel nostro gruppo... sempre all'avanguardia: eventi, proof courses, danza, tutto. Il re di Atmos ... che musicista, che pizza ... quanti schiaffi sul collo t'ha dato Basix ... ma in fondo ti piacciono. Sei il tipo piú amorevole del mondo (cit)... e sei stato lí quando ne avevo bisogno, tu, un piccolo gipsy king di Bracciano. Un saluto anche a Sergiña e un in bocca al lupo con la sua band.

Jon, no words … thanks for being Jon … an open mind guy, always critic in the right way, ready for helping anyone, gull of love … Jon is an angel. He is the kind of guy that gives you something even if he does not have so much of it. He

gave me time when he did not have so much for himself either! Thank you for the great time we had together, the movies, the ice cream, the concert … Graspop 2017 was unforgettable. Thanks for sharing the comics adventure … we are the Oneiros (a thanks also to our marvelous inker Jonathan!!!) and made our first piece of art. More is coming!!! A hug goes also to your wife Rongling!

Grazie ai miei amici in Italia, in particolare i mitici Andrea, Filippo, Mariateresa, Manuel, Simone, Ettore, Alessandro e Fabio... questi ragazzi hanno reso la mia vita meravigliosa, L'Aquila, i Thunder 'n Fire, il bicio al bacio, le gite, il mare e tant'altro. Grazie a Gabriele e Lorenzo, i miei coinquilini a L'Aquila ... birrette a profusione e cose strane.

In fine, l'abbraccio piú stretto va alla mia famiglia, sempre presente, amorevole. Grazie Nicolino, Coccia Pelata, un padre affettuoso, un amico, tutto. Mi ha dato tanta libertá nelle scelte e i consigli giusti per raggiungere la mia felicitá ... hanno funzionato. Grazie Milva, Tonnoliscia, per avermi dato tanti tanti baci. Per essere state sempre comprensiva e vicina. Il mio trainer personale in termini di esercizi di matematica e memorizzazione di poesie ... e anche la miglior cucina italiana!!!

Fabietto, detto Testa Calda Mastrolindo. Grazie Fabietto per quello che hai fatto e farai ... sei un pochino macho ma in fondo sei un cucciolo di pollo. Continua a coltivare le tue passioni, musica, disegno e il resto ... un grande in bocca al lupo con la tua nuova avventura! Non vedo l'ora di mangiare rustell a casa tua.

Zia Mariangela, Zanzibar, un bacione anche te che sei stata sempre attenta ... a tutto. Ci siamo divertiti tanto insieme, mi hai insegnato tanto. Ci siamo divertiti tantissimo ad Eindhoven a il futuro é sempre piú roseo. Sei l'avvocato piú dolce del mondo.

Grazie a tutti per farmi sentire cosí amato e felice.

Simone

This work is part of the research programme NOW-TTW Perspectief MEMPHIS II (Merging Electronics and Micro and nano-Photonics) with project number 13539, which is financed by the Netherlands Organization for Scientific Research (NWO).

Curriculum Vitae

Simone Cardarelli was born on 16-05-1990 in Teramo, Italy. After finishing the high school Liceo Scientifico Saffo in 2009 in Teramo, Italy, he studied Electrical Engineering at University of L'Aquila in L'Aquila, Italy. In 2012 he obtained the Bachelor degree with 110/110 cum laude. A research project on analog electronic interfaces for capacitive sensors has been performed as final Bachelor project. In 2012 he started his Master study in the University of L'Aquila. In 2013 he was a visiting student at the Eindhoven University of technology to perform the Master final project within the ECO group. During the Master project he realized and characterized an optical re-circulating loop. He obtained his Master degree in 2014 with 110/110 cum laude. From February 2015 he started his PhD project at the Eindhoven University of Technology at Eindhoven. The main focus of his research was to explore efficient and accurate alignment techniques for optical systems, by means of novel photonic integrated devices. His expertise focuses on electro-optic effects in InP/InGaAsP materials, optical beam steering, imaging techniques, fabrication of photonic integrated circuits, piezoelectric actuators for alignment of optical fibers. He developed a novel Electro-Optic beam steering method for sub-micrometer optical alignment, which is reported in this thesis.